ABSTRACT

Title of Dissertation: Progress in Nitrogen Vacancy
Nuclear Magnetic Resonance Detection

Emma Kaye Huckestein
Master of Science, 2023

Dissertation Directed by: Dr. Ronald L. Walsworth
Department of Electrical and Computer Engineering

Nuclear Magnetic Resonance (NMR) spectroscopy is a powerful analytic tool of use in the physics, chemistry, and biology disciplines, yet the resource costs to buy, maintain, and use the spectrometer limit the tool's accessibility and the limited sensitivity and spectral resolution limit its application space. In recent years, Nitrogen Vacancy (NV) centers have emerged as an alternative NMR sensor due to their atomic-scale resolution and minimal resource costs. However, NV-NMR similarly suffers from limited sensitivity and spectral resolution due to the technical challenges associated with increasing the applied magnetic field. In this work, the sensitivity of an existing NV-NMR setup is characterized to determine the experimental modifications necessary for measurements at higher magnetic fields (> 0.5 T). As a consequence of this characterization, a coplanar waveguide integrated with a microfluidic channel is designed. Finally, metabolomics, particularly spheroids, are reviewed for a potential high-impact NV-NMR application given historically relevant sample concentration sensitivities.

Progress in Nitrogen Vacancy Nuclear Magnetic Resonance Detection

by

Emma Kaye Huckestein

Dissertation submitted to the Faculty of the Graduate School of the
University of Maryland, College Park in fulfillment
of the requirements for the degree of
Master of Science
2023

Advisory Committee:
Dr. Ronald L. Walsworth, Chair/Advisor
Dr. Wendell T. Hill
Dr. Christopher Jarzynski

Dedication

To my parents

Acknowledgments

During my time in graduate school, not only did I have the immense honor of learning and contributing to scientific advancement, but I had the privilege of learning who I am as a scientist and pushing myself beyond what I ever thought I was capable of. I am incredibly grateful for the opportunity for this journey of self- and scientific discovery, and I have so many wonderful people to thank for helping to shape and contribute to this journey.

First, I'd like to thank my advisor, Dr. Ronald Walsworth. Throughout the years, he has provided fantastic feedback on my research endeavors and allowed me to be a bridge between ongoing research at Harvard and the University of Maryland. He is an incredibly empathetic advisor who genuinely cares for the well-being and future happiness of his graduate students, post-docs, and staff scientists. Very recently, I decided to leave graduate school early with my Masters, and Dr. Walsworth was incredibly supportive of my decision and immediately began reaching out to his various contacts to help me find a job. It was in that moment that I realized how incredibly fortunate I was to find Dr. Walsworth and have him as my advisor.

Next, I would like to thank the current and former members of Dr. Walsworth's research group. I've had the pleasure of closely working with Nithya Arunkumar, John Blanchard, Johannes Cremer, Stephen DeVience, Daniel Ang, Declan Daly, Connor Hart, and Matthew Turner. To Matthew, I thank him for introducing me to biological NV applications and the QDM, and I thank him allowing me to badger him with questions at all hours. To Connor, I thank him for teaching me about diamond characterization and optimizing/designing a state-of-the-art NV experiment, and I thank him for his kindness, for no matter how busy he was, he always took the time to ask how I was doing. To Declan, I thank him for his skills of optics alignment and work ethic, and I thank him for being my friend. To Stephen, I thank him for sharing his NMR expertise on both the Harvard and UMD experiments. To Johannes, I thank him for his assistance for all NV-NMR related activities at Harvard and for his desire to help in any way that he can. To John, I thank him as well for his NMR expertise and I thank him, Johannes, and Declan for the fun times we shared desperately trying to resolve the seemingly never-ending list of problems with the Harvard experiment. To Nithya, I thank her for her passing her NV-NMR knowledge to me. Finally, to Daniel, although our time working together has been short, I thank him for setting up the high field magnet at UMD. I also thank Johannes, John, Stephen, and Daniel for their comments and feedback while I was writing this thesis.

I would also like to thank all of my friends who have provided their unwavering support and love regardless of the length of time we have been in each others lives. I thank Chloe Grove, Tori Daniels, Henry Gunner, Lindsey Wood, Greeshma Shivali Oruganti, Wells Taylor, Gary Trice, Brian Ryall, Brandon Hunt, Skylar Crews, Gracie Fitzgerald, Margaret Spacapan, and Katie Barnes.

Next, I want to thank my undergraduate professors. To Dr. Jeffrey Fieberg, I thank him for teaching a mock class at Centre's Acceptance Day weekend otherwise I never would have attended Centre and never would have the honor of having him as my undergraduate advisor. To Dr. Jason Neiser, I thank him for his passionate teaching and the many long hours with my numerous sticky note questions. To Dr. Fulfer, I thank her for being such wonderful supporter of all women in STEM. To all of my Centre professors, including the ones here, I thank them for nurturing my intellectual curiosity.

Finally, I want to thank my parents; for them, it is hard to find the words to express my gratitude. To my dad, thank you for showing me what hard work is, thank you for showing me how to get back up when I don’t succeed, and thank you for showing me what unconditional support is. To my mom, thank you for showing me how to find the joy in everything that I do in life, thank you for helping me figure out who I am and what I want in life, and thank you for showing me what true courage is.

Table of Contents

Dedication ii

Acknowledgements iii

Table of Contents vi

List of Tables viii

List of Figures ix

Chapter 1: Introduction 1
- 1.1 Nitrogen Vacancy (NV) Centers 1
- 1.2 Hamiltonian Physics 4
  - 1.2.1 Rotating Reference Frame 7
- 1.3 Sensing Mechanisms 7
  - 1.3.1 DC Sensitive Measurements 8
  - 1.3.2 AC Sensitive Measurements 15

Chapter 2: Nuclear Magnetic Resonance (NMR) 22
- 2.1 NMR History 22
- 2.2 The Basics of NMR Spectroscopy 23
- 2.3 Associated Challenges 27
- 2.4 NV Centers as an Alternative 28

Chapter 3: Progress of NV-NMR Experiments 31
- 3.1 CASR 32
- 3.2 AERIS/DRACAERIS 35

Chapter 4: Characterization of NV-NMR Experiment Sensitivity 39
- 4.1 Experimental Layout 39
  - 4.1.1 Optical Pathway 39
  - 4.1.2 Electronics 43
- 4.2 Measuring Sensitivity of NV-Based Measurements 46
  - 4.2.1 CW-ODMR 47
  - 4.2.2 Rabi 48
  - 4.2.3 AC Magnetometry 48
  - 4.2.4 CASR 50

    4.2.5 Sensitivity 50
    4.2.6 Example Calculation 50
    4.2.7 Sensitivity vs. Frequency 53
    4.2.8 Discussion 56
  4.3 Inductive NMR Measurements 63

Chapter 5: MW Delivery 69
  5.1 MW Resonators 70
  5.2 Coplanar Waveguide 72

Chapter 6: Metabolomics 76
  6.1 Metabolomics with NMR 76
  6.2 NV-NMR Concentration Sensitivity 77
    6.2.1 Spheroids 79

Appendix A: Diamond Characterization 82
  A.1 T_2^* 83
  A.2 T_2 83
  A.3 ^{14}N Contamination 84
  A.4 Strain and Linewidths 85
    A.4.1 Luke Skywalker 86
    A.4.2 Princess Leia 88
    A.4.3 Han Solo 90
    A.4.4 Arya Stark-D 92

Bibliography 93

Bibliography 93

List of Tables

3.1 Summary of Results from Previous NV-NMR Experiments 38

4.1 Summary Experimental Conditions and Calculated Sensitivity for Each Coil Frequency 68

5.1 Summary of MW Resonators Used for NV and EPR Experiments 75

6.1 Concentration Sensitivity for NV-NMR Experiments 79
6.2 Minimum Concentration Measurable for a Given Acquisition Time 80

A.1 T_2^* Data for Luke Skywalker, Princess Leia, Han Solo, Arya-D, and John McClane-B 84
A.2 T_2 Data for Luke Skywalker, Princess Leia, Han Solo, Arya-D, and John McClane-B 84

List of Figures

1.1 Nitrogen-Vacancy Center's Diamond Orientation and Energy Structure 4
1.2 Continuous-Wave Optically Detected Magnetic Resonance (CW-ODMR) Sequence and Bloch Sphere Diagram 10
1.3 Rabi Nutations Sequence and Bloch Sphere Diagram 13
1.4 Ramsey Sequence and Bloch Sphere Diagram 16
1.5 Spin Echo Sequence and Bloch Sphere Diagram 19
1.6 Spin Echo and CPMG Data 20

2.1 Conventional NMR Spectroscopy Overview 27

3.1 CASR Sequence 34
3.2 AERIS/DRACAERIS Sequence 36

4.1 NV-NMR Experiment's Optical Pathway 40
4.2 NV-NMR Electronic Components 44
4.3 CW-ODMR Data used to Characterize Experimental Sensitivity 47
4.4 Rabi Data used to Characterize Experimental Sensitivity 48
4.5 AC Magnetometry Sequence 49
4.6 AC Magnetometry Data for a $f_{\text{coil}} = 1$ MHz and an XY8-8 Magnetometry Sequence 51
4.7 CASR Data for a $f_{\text{coil}} = 1$ MHz, an XY8-8 Magnetometry Sequence, and 25 Averages 53
4.8 AC Magnetometry Plots for a Variety of Coil Frequencies 54
4.9 CASR Spectrum for a Variety of Coil Frequencies 55
4.10 Sensitivity, η_{AC}, for Each Coil Frequency 56
4.11 Overlaid Unconverted CASR Data for all Coil Frequencies 58
4.12 Overlaid Converted CASR Data Noise Floor for all Coil Frequencies 59
4.13 Measured Photodiode Noise 60
4.14 Exponential Decay Fit to Measured Rabi and XY8-M Data to Extract T_2 62
4.15 Close-up of Sample Holder 63
4.16 Inductive NMR Sequence 64
4.17 Inductive NMR Spectrum of a Copper Sulfate and DI Water Solution 65
4.18 Measure B_1 Rabi 66

5.1 CAD Model of Coplanar Waveguide 73

A.1 DEER ESR Spectrum Depicting ^{14}N Contamination in Luke Skywalker 85
A.2 NV Resonance Linewidths Across 4×4 mm Surface of Luke Skywalker 86
A.3 Strain Measured Across 4×4 mm Surface of Luke Skywalker 87

A.4 NV Resonance Linewidths Across 4×4 mm Surface of Princess Leia 88
A.5 Strain Measured Across 4×4 mm Surface of Princess Leia 89
A.6 NV Resonance Linewidths Across 4×4 mm Surface of Han Solo 90
A.7 Strain Measured Across 4×4 mm Surface of Han Solo 91
A.8 Strain and Linewidth Across 2×2 Surface of Arya Stark-D 92

Chapter 1: Introduction

This thesis is organized as follows: Chapter 1 introduces Nitrogen Vacancy (NV) centers and describes the typical sequences used to manipulate and readout the spin state. Chapter 2 briefly summarizes the historical impact and challenges of conventional Nuclear Magnetic Resonance (NMR) spectroscopy and proposes NV centers as an alternative NMR sensor. Chapter 3 reviews historical NV-NMR experiments and describes the CASR and AERIS/DRACAERIS sequences. Chapter 4 details the sensitivity characterization of an existing NV-NMR experiment and assesses the issues limiting sensitivity. Chapter 5 briefly summarizes MW resonators and describes the design of a coplanar waveguide integrated with a microfluidic channel. Finally, Chapter 6 introduces metabolomics, particularly the study of spheroids, as potentially high-impact NV-NMR applications given historically relevant sample concentration sensitivities.

1.1 Nitrogen Vacancy (NV) Centers

Nitrogen Vacancy (NV) centers are atomic-scale defects in diamond that have proven to be powerful quantum sensors of local phenomena in a large variety of systems such as integrated circuits [1–3], biological samples [4–7], chemical identification via NMR [8–19], chemical identification via Electron Paramagnetic Resonance (EPR) [20], geological samples [21–23], microfluidic diffusion mechanisms [24], imaging [25, 26], and dark matter detection [27, 28].

Comprised of a substitutional nitrogen atom adjacent to a vacancy (see Figure 1.1**(b)**), NV centers can have four crystallographic axes, which define the four NV quantization axes, and three charge states, either NV^-, NV^0, or NV^+. However, the NV^- charge state is most useful for sensing purposes, so from here on after, the generalization of NV corresponds specifically to the NV^- charge state, unless otherwise stated.

Most remarkably, NV centers exhibit spin-state dependent fluorescence at room temperature via visible light excitation, as illustrated in Figure 1.1**(a)**. NV centers are spin triplets (S = 1) in the electronic ground state $^3\mathrm{A}_2$, and when isolated from a magnetic field, the ground spin projection $\mathrm{m_s} = 0$ and $\mathrm{m_s} = \pm1$ are separated by a zero-field splitting of $\mathrm{D_{gs}} \approx 2.87$ GHz. When exposed to non-zero magnetic fields, the degeneracy of the $\mathrm{m_s} = \pm1$ states is lifted by the Zeeman interaction (Equation 1.1) equal to $\Delta = 2\gamma_e B_{0,\|}$, where γ_e is the electron gyromagnetic ratio, approximately equal to 2.8 MHz/G, and $B_{0,\|}$ is the magnetic field component parallel to the NV quantization axis. Depending on the substitutional nitrogen isotope, each electronic spin state is further split by the hyperfine interaction (Equation 1.2) yielding nuclear spin states $\mathrm{m_I} = -1, 0, +1$ for $^{14}\mathrm{N}$ isotope or $\mathrm{m_I} = \pm\frac{1}{2}$ for $^{15}\mathrm{N}$ isotope.

Both the $\mathrm{m_s} = 0$ and $\mathrm{m_s} = \pm1$ states can be optically excited with wavelengths $490-637$nm [29–31], however 532nm light is typically used due to commercial availability. Additionally, the transitions between the states can be driven by applied microwaves (MWs). Preferentially, the excited $\mathrm{m_s} = 0$ state decays to the ground $\mathrm{m_s} = 0$ and emits red, 637 nm fluorescence (e.g. zero-phonon line (ZPL)). However, the excited $\mathrm{m_s} = \pm1$ states decay roughly equally to the ground $\mathrm{m_s} = 0$ and $\mathrm{m_s} = \pm1$ states because of an ISC (Inter-System Crossing) which includes a metastable singlet state that does not fluoresce in the 600 - 800 nm range [30].

Although Section 1.3 provides a detailed explanation of common NV spin state manipulations, for explanatory purposes, a general NV-based experiment is provided. The NV system is exposed to either a DC or AC magnetic field, B, which is the sum of an applied magnetic field, B_0, and a local magnetic field, B_{local}. The NVs are then initialized into the $\text{m}_\text{s} = 0$ state via a 532 nm laser pulse; because of the ISC decay pathway into both $\text{m}_\text{s} = 0$ and $\text{m}_\text{s} = \pm 1$, the NV population accumulates in the $\text{m}_\text{s} = 0$ state with exposure to this 532 nm pulse. Under the influence of B, the NV resonances shift proportional to B (Equation 1.4). By manipulating the NV spin states with MWs and measuring the emitted fluorescence of the final state with another 532 nm pulse, the local magnetic field B_{local} can be extracted[1]. Thus, the NV exhibits spin-state dependent fluorescence, optical initialization, and optical readout, which are all qualities of paramount importance for the determination of local phenomena such as magnetic and electric fields, strain, temperature, or stress. Because the NV couples to these local phenomena, they alter the NV spin state, which in turn, alters the magnitude of the emitted red fluorescence. Therefore, by monitoring the magnitude of the red fluorescence, the local environment of the NV system can be determined.

---

[1] The same principles can be applied to extract information regarding other local phenomena.

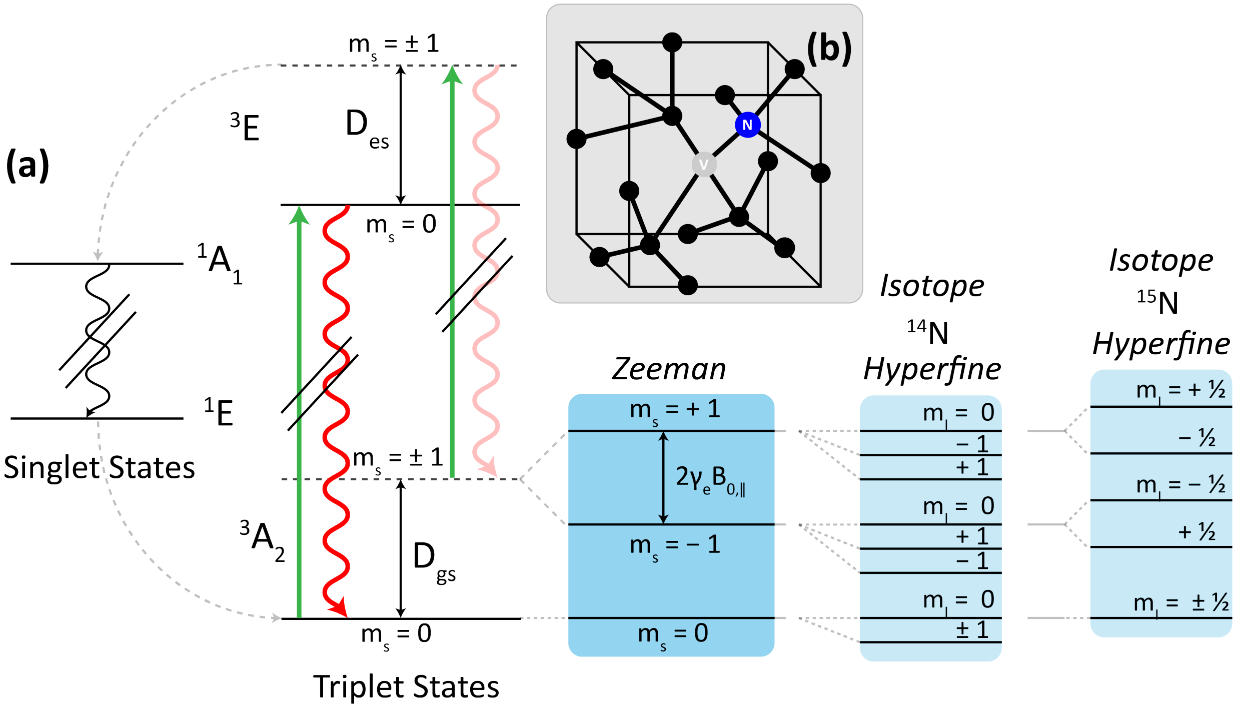

Figure 1.1: **(a) NV energy structure:** The NV center is a spin-triplet (S = 1) defect. At zero-field, the ground $\mathrm{m_s} = 0$ and degenerate $\mathrm{m_s} = \pm 1$ states are separated by a zero-field splitting of $\mathrm{D_{gs}} \approx 2.87$ GHz. Once exposed to a magnetic field, the degeneracy is lifted via the Zeeman interaction equal to $\Delta = 2\gamma_e B_{0,\parallel}$, where γ_e is the NV's electron gyromagnetic ratio and $B_{0,\parallel}$ is the magnetic field component parallel to the NV quantization axis. The hyperfine interaction further splits the electronic spin states yielding nuclear spin states that are isotope-dependent; the ^{14}N isotope yields nuclear states $\mathrm{m_I} = -1, 0, +1$ and the ^{15}N one yields $\mathrm{m_I} = \pm\frac{1}{2}$. The ground $\mathrm{m_s}$ states can be excited via green, 532 nm light and emit red, 637 nm fluorescence upon decay. Due to the ISC, the excited $\mathrm{m_s} = \pm 1$ states decay roughly equally to the ground to $\mathrm{m_s} = 0$ state and $\mathrm{m_s} = \pm 1$ states; decay through the ISC is through a metastable singlet state which does not fluoresce in the 600 - 800 nm range. **(b) NV orientation in the diamond lattice:** The NV center is comprised of a substitutional Nitrogen atom (blue sphere - either ^{14}N or ^{15}N) adjacent to a vacancy (gray sphere) in the diamond's Carbon (black spheres) lattice.

1.2 Hamiltonian Physics

The NV Hamiltonian can be simplistically written as

$$\hat{H} = \hat{H}_0 + \hat{H}_{\text{nuclear}} + \hat{H}_{\text{elec,str}}$$

where $\hat{H}_0$ encodes the electron spin interaction (Zeeman interaction), $\hat{H}_{\text{nuclear}}$ encodes the nuclear spin interactions (hyperfine splitting), and $\hat{H}_{\text{elec,str}}$ encodes electron interactions with electric fields and diamond strain (spin coupling to electric fields and strain) [30, 32].

Defining $\hat{z}$ to be along the NV quantization axis, $\hat{H}_0$ can be written as:

$$\frac{\hat{H}_0}{h} = DS_z^2 + \frac{g_e\mu_B}{h}(\vec{B}\cdot\vec{S}), \tag{1.1}$$

where $g_e \approx 2.003$ is the electronic g-factor, μ_B is the Bohr magneton, $\vec{B} = (B_x, B_y, B_z)$ is the sum of any applied (B_0) and local (B_{local}) magnetic field, and $\vec{S} = (S_x, S_y, S_z)$ is the dimensionless electronic spin-1 operator [32].

Similarly, $\hat{H}_{\text{nuclear}}$ can be written as:

$$\frac{\hat{H}_{\text{nuclear}}}{h} = \begin{cases} A_{\parallel}S_zI_z + A_{\perp}(S_xI_x + S_yI_y) - \frac{g_I\mu_N}{h}(\vec{B}\cdot\vec{I}), & \text{if } ^{15}\text{N} \\ A_{\parallel}S_zI_z + A_{\perp}(S_xI_x + S_yI_y) - \frac{g_I\mu_N}{h}(\vec{B}\cdot\vec{I}) + P(I_z^2 - I(I+1)/3), & \text{if } ^{14}\text{N} \end{cases} \tag{1.2}$$

where $A_{\parallel}$ is the axial magnetic hyperfine coupling coefficient, $A_{\perp}$ is the transverse coefficient, P is the nuclear electric quadrupole parameter, g_I is the isotope-dependent nuclear g-factor, μ_N is the nuclear magneton, and $\vec{I} = (I_x, I_y, I_z)$ is the dimensionless nuclear spin operator [32].

Finally, $\hat{H}_{\text{elec,str}}$ can be written as:

$$
\begin{aligned}
\frac{\hat{H}_{\text{elec,str}}}{h} &= (d_{\parallel}E_z + M_z)S_z^2 \\
&+ (d_{\perp}E_x + M_x)(S_y^2 - S_x^2) \\
&+ (d_{\perp}E_y + M_y)(S_xS_y + S_yS_x) \\
&+ (d_{\perp}^{'}E_x + N_x)(S_xS_z + S_zS_x) \\
&+ (d_{\perp}^{'}E_y + N_y)(S_yS_z + S_zS_y),
\end{aligned}
\tag{1.3}
$$

where $d_{\parallel}$ is the axial dipole moment, $d_{\perp}, d_{\perp}^{'}$ are the transverse dipole moments, and M_x, M_y, M_z, N_x, N_y are the spin-strain coupling parameters [32].

The full Hamiltonian for the NV system described in this thesis is (assuming an ^{14}N isotope – the full Hamiltonian for the ^{15}N isotope excludes the quadrupole parameter):

$$
\begin{aligned}
\frac{\hat{H}}{h} &= DS_z^2 + \frac{g_e\mu_B}{h}(\vec{B}\cdot\vec{S}) \\
&+ A_{\parallel}S_zI_z + A_{\perp}(S_xI_x + S_yI_y) \\
&+ P(I_z^2 - I(I+1)/3) - \frac{g_I\mu_N}{h}(\vec{B}\cdot\vec{I}) \\
&+ (d_{\parallel}E_z + M_z)S_z^2 \\
&+ (d_{\perp}E_x + M_x)(S_y^2 - S_x^2) \\
&+ (d_{\perp}E_y + M_y)(S_xS_y + S_yS_x)
\end{aligned}
\tag{1.4}
$$

Unfortunately, due to the large applied magnetic fields in this thesis, the Hamiltonian cannot be simplified further. Of note for the remainder of this thesis is the coupling to the local phenomena, such as magnetic field, electric field, and crystal strain. These couplings ultimately shift the NV resonance frequency, and monitoring the magnitude of these shifts via the spin-state dependent fluorescence allows the reconstruction of the local phenomena that caused it.

1.2.1 Rotating Reference Frame

Due to the complexity of time-dependent Schrodinger mathematics, it is often easier to transform to a time-independent Hamiltonian. This transformation can be done by operating in a rotating reference frame with rotational frequency ω_{rot} equal to the spin precession frequency [33]. Mathematically, the Hamiltonian transformation is:

$$\hat{H}' = \exp(i\omega_{\text{rot}} t \hat{I}_z) \hat{H} \exp(-i\omega_{\text{rot}} t \hat{I}_z) - \omega_{\text{rot}} \hat{I}_z,$$

where $\hat{I}_z$ represents any spin operator [33]. Unless otherwise stated, the remainder of this thesis operates in the rotating reference frame.

1.3 Sensing Mechanisms

Although the aforementioned Hamiltonian (Eq. 1.4) fully describes the quantum response for any spin state manipulation applied to the NV centers, the following sections attempt to summarize these spin state manipulations broadly and pictorially using Bloch Sphere diagrams. The spin state manipulations described here are by no means a comprehensive list[2]. Rather, they are those most applicable for the scope of this thesis.

---

[2] This list excludes spin state manipulations primarily used for single NV systems.

1.3.1 DC Sensitive Measurements

The following spin state manipulations are used to measure DC effects in or near the diamond. These DC effects include, but are not limited to, static local magnetic fields or gradients from thermal, dipolar coupling, or strain effects.

1.3.1.1 Continuous Wave Optically Detected Magnetic Resonance (CW-ODMR)

Continuous Wave Optically Detected Magnetic Resonance (CW-ODMR) can be used to extract vector and magnitude information about the local magnetic field, B_{local}, by measuring the NV resonance frequency associated with $\text{m}_\text{s} = 0 \longleftrightarrow \text{m}_\text{s} = -1$ and $\text{m}_\text{s} = 0 \longleftrightarrow \text{m}_\text{s} = +1$, and the corresponding hyperfine transitions [26, 34].

Figure 1.2 depicts the CW-ODMR pulse sequence and the associated Bloch Sphere diagram of the $\text{m}_\text{s} = 0 \longleftrightarrow \text{m}_\text{s} = +1$ spin states[3]. First, low-intensity 532 nm light and low-power MW radiation are simultaneously applied. The 532 nm light initializes the NVs into the $\text{m}_\text{s} = 0$ ground state due to the preferential decay mentioned in Section 1.1. Depending on the frequency of the applied MW, the NV spin state is either partially transferred to $\text{m}_\text{s} = +1$ (i.e. an on-resonant drive) or remains in $\text{m}_\text{s} = 0$ (i.e. an off-resonant drive). By measuring the emitted fluorescence, the resultant spin state is then readout; an on-resonant drive reduces fluorescence intensity due to decay of $\text{m}_\text{s} = \pm 1$ states through the non-radiative metastable singlet state (Section 1.1), while an off-resonant drive does not change fluorescence intensity [35]. Colloquially, this first readout is called *signal*. The second readout, for which no MWs are applied to the system, is called *reference*. Ultimately, the data plotted is:

---

[3] The same principles are applied to the $\text{m}_\text{s} = 0 \longleftrightarrow \text{m}_\text{s} = -1$ transition.

$$C = \frac{F_{\text{sig}}}{F_{\text{ref}}},$$

where C is the measurement contrast, F_{sig} is the *signal* fluorescence measured by a photodiode (or photon counter) in units of V (or in units of counts), and F_{ref} is the *reference* fluorescence. Processing the data and plotting in terms of C eliminates common-mode noise like laser noise [30]. Thus, sweeping the applied MW frequency yields the electronic and hyperfine transitions. Once the resonance information is obtained, the local magnetic field information can be extracted. In the absence of any local field effects, the resonance frequencies, defined as ν_0, are a consequence of only the B_0 field which is applied to lift the $\mathrm{m_s} = \pm 1$ degeneracy. However, in practical experimental conditions, the resonance frequencies, ν_B, are a consequence of B_0 and B_{local}. By calculating the resonance difference, $\delta\nu = \nu_B - \nu_0$, the vector and magnitude information of B_{local} can be extracted [34, 36][4].

---

[4] Typically, when interested in the vector information, B_0 is applied in an arbitrary direction such that all four NV orientations are spectrally distinguishable [7, 26, 34, 35].

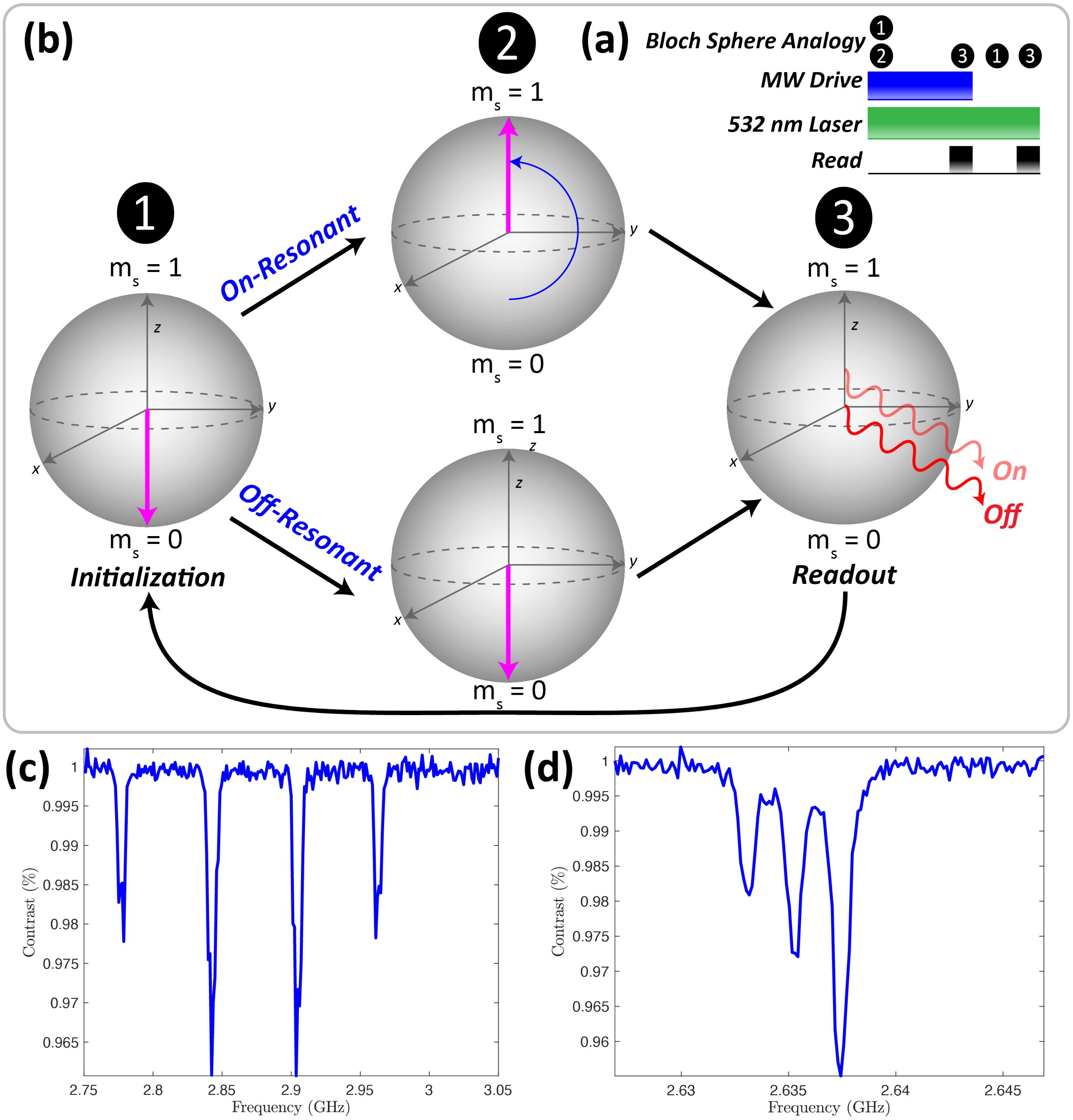

Figure 1.2: **(a) CW-ODMR pulse sequence. (b) Bloch Sphere Analogy:** Low-intensity 532 nm light and low-power MWs are simultaneously applied to the NV system. On-resonant MWs partially transfer spin population to $m_s = +1$ (yields decrease in measured fluorescence intensity). Off-resonant MWs have no effect, and the spins remain in $m_s = 0$ (yields no change in measured fluorescence intensity). **(c) CW-ODMR data:** For this data, B_0 is parallel to a single NV orientation (exterior resonances) which causes the other three orientation resonances' to overlap (interior resonances). **(d) CW-ODMR data:** Depicts the hyperfine resonances of the $m_s = -1$ electronic state for a ^{14}N diamond. Again, B_0 is parallel to a single NV orientation for this data.

1.3.1.2 Rabi Nutations

Broadly, the Rabi sequence establishes the MW pulse duration necessary for coherent spin population oscillations [35][5].

As depicted in Figure 1.3**(a)** and **(b)**, the NVs are first initialized into the $\mathrm{m_s} = 0$ state, then a high-power MW pulse is applied. The degree of which the spin population rotates around the Bloch sphere is a consequence of both the duration and amplitude of this applied MW pulse. Typical Rabi experiments hold the amplitude constant and sweep the pulse duration to determine the MW pulse duration which rotates the population to the $\mathrm{m_s} = +1$ state. Colloquially, this duration is referred to as a π pulse, and because of the aforementioned non-radiative decay path (Section 1.1), this rotation decreases the red fluorescence output. For any other pulse duration, the measured fluorescence corresponds to the projection of the final state onto the $\mathrm{m_s} = 0$ and $\mathrm{m_s} = +1$ manifold (Figure 1.3).

Following read-out of the *signal* measurement (i.e. MWs are on), the NVs are re-initialized and the *reference* measurement (i.e. MWs are off) is collected. The resultant data (Figure 1.3**(c)**) is an oscillation for which each contrast minimum represents a population transfer to the $\mathrm{m_s} = +1$ state[6]. The frequency of this oscillation, or the rate at which rotations are driven, is called the Rabi frequency (Ω); it scales with the square root of the applied MW power and can be calculated by[7]:

---

[5] There are examples using the Rabi sequence for other purposes, such as imaging the magnetic field produced by a MW device [37].

[6] Again, contrast is defined to be: $C = \frac{F_{\mathrm{sig}}}{F_{\mathrm{ref}}}$

[7] The calculation for Ω is simplified because we assume operation in the rotating reference frame; in this frame, $\mathrm{B_{MW}}$ also rotates with the NV spins.

$$\Omega = \gamma_e \mathrm{B}_{\mathrm{MW}},$$

where B_{MW} is the component of the applied MW field perpendicular to the NV quantization axis [33–35]. Ultimately, the Rabi oscillation will exponentially decay due to NV spin decoherence caused by gradients (thermal, dipolar coupling, strain) across the field of view or B_0/B_1 inhomogeneities, where B_1 is the Rabi frequency of an RF pulse (see Chapter 3 for more information) [35, 38, 39].

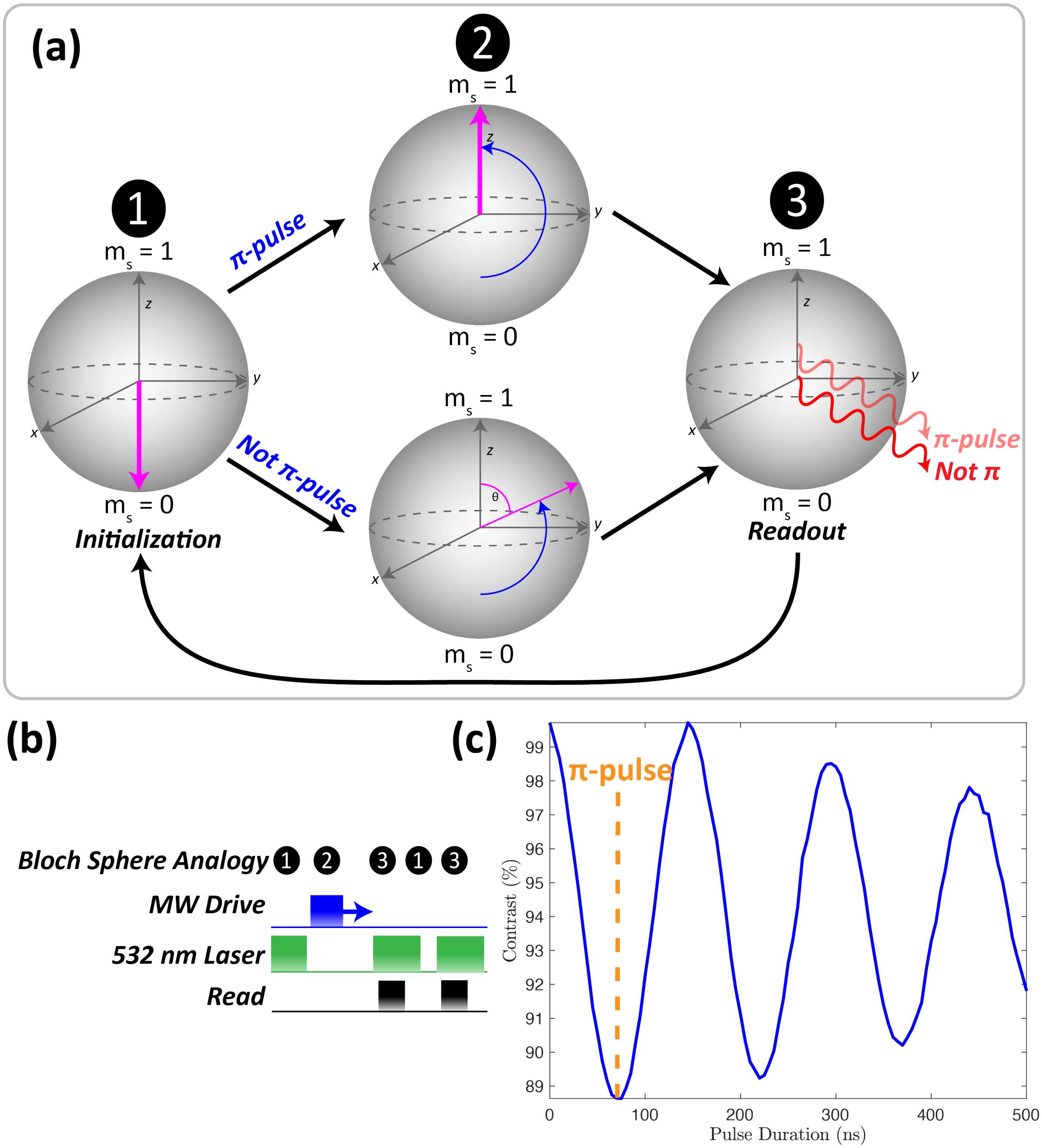

Figure 1.3: **(a) Rabi pulse sequence.** **(a) Bloch Sphere Analogy:** The NVs are initialized, and a high-power MW pulse is applied to drive spin population oscillations; if the population is rotated to $m_s = +1$, the corresponding MW pulse duration is colloquially referred to as a π pulse, and the fluorescence output is decreased. **(a) Rabi pulse sequence:** Depicts both the signal (MWs on) and reference (MWs off) measurements. Blue arrow illustrates that the pulse duration is swept while the amplitude is held constant. **(c) Rabi Data:** Each minimum represents an integer multiple of a π pulse. The exponential decay is a consequence of NV decoherence.

1.3.1.3 Ramsey

The Ramsey sequence [40] has two primary purposes: (1) extract the magnitude of B_{local} [26, 27, 41–44], and (2) measure the NV diamond's characteristic decay time, T_2^* [26, 30, 32, 35, 45–48]. However, for the scope of this thesis, the Ramsey sequence will be utilized for T_2^* characterization, where T_2^* decay is a consequence of spin dephasing from DC or slowly varying inhomogeneities in the diamond [32].

Like the previous sequences, the NVs are first initialized into $\text{m}_\text{s} = 0$ via a high-intensity 532 nm laser pulse. Next, a high-power MW $\pi/2$ pulse, the duration of which was calibrated by the Rabi sequence (Section 1.3.1.2), prepares the NVs in an equal superposition of the $\text{m}_\text{s} = 0$ and $\text{m}_\text{s} = +1$ states. The NVs then freely precess for a time, τ, during which they accumulate a phase, $\phi = 2\pi\gamma_e B_{\text{local}}\tau$ [34, 35]. After τ, another $\pi/2$ pulse projects the spin state back into the $\text{m}_\text{s} = 0$ and $\text{m}_\text{s} = +1$ manifold, and the phase accumulation is readout via another laser pulse. The sequence is then repeated such that the phase of the final $\pi/2$ pulse in the second sequence is π out of phase with the final $\pi/2$ in the first sequence. These phase adjustments cancel low-frequency noise. The measured contrast ultimately plotted is:

$$C = \frac{F_{x(y)} - F_{-x(-y)}}{F_{x(y)} + F_{-x(-y)}},$$

where $F_{x(y)}$ is the fluorescence measured by the photodiode (units of V) after a $\pi/2$ pulse with phase x (or y) and $F_{-x(-y)}$ is the fluorescence measured by the photodiode (units of V) after a $\pi/2$ pulse with phase $-x$ (or $-y$) [30]. By sweeping τ, Ramsey fringes can be measured, and the fringes can be Fourier transformed to extract their frequency. The B_{local} magnitude can then be extracted with $B_{\text{local}} = \delta\nu/\gamma_e$, where $\delta\nu$ is the frequency difference between the expected Ramsey fringes produced by applied B_0 and the measured Ramsey fringes produced by $B = B_{\text{local}} + B_0$ [35].

Ultimately, the contrast of the Ramsey fringes will exponentially decay with the aforementioned characteristic time T_2^* [35]; a simplistic mechanism expatiating this decay is depicted in Figure 1.4(**b**). During the free precession τ, the NV spins accumulate different phases due to the inhomogeneities in their individual environments. Once these phase accumulations are projected back into the $\mathrm{m_s} = 0$ and $\mathrm{m_s} = +1$ manifold, the resulting spin states are no longer coherent, so the fluorescence output is no longer correlated to B_{local} and the measured contrast decays. To extract T_2^*, the data can be fit with $e^{\frac{-\tau}{\mathrm{T}_2^*}p}$, where p is a stretched exponential parameter [47, 49].

T_2^* is usually of the order of μs [32, 47], and in an experimental setting, this dephasing limits the time for which coherent magnetic field sensing can occur. Thus, it is in the best interest of the experimentalist to extend this dephasing time. The following sections, 1.3.2.1, 1.3.2.2, and 1.3.2.3, describe pulse sequences that refocus these dephasing effects.

1.3.2 AC Sensitive Measurements

Akin to the DC counterpart, the AC sensitive measurements can be used to extract information on local oscillating phenomena, to characterize spin decoherence caused by interactions with ^{13}C or paramagnetic spins in the diamond lattice, and to refocus DC dephasing effects [35].

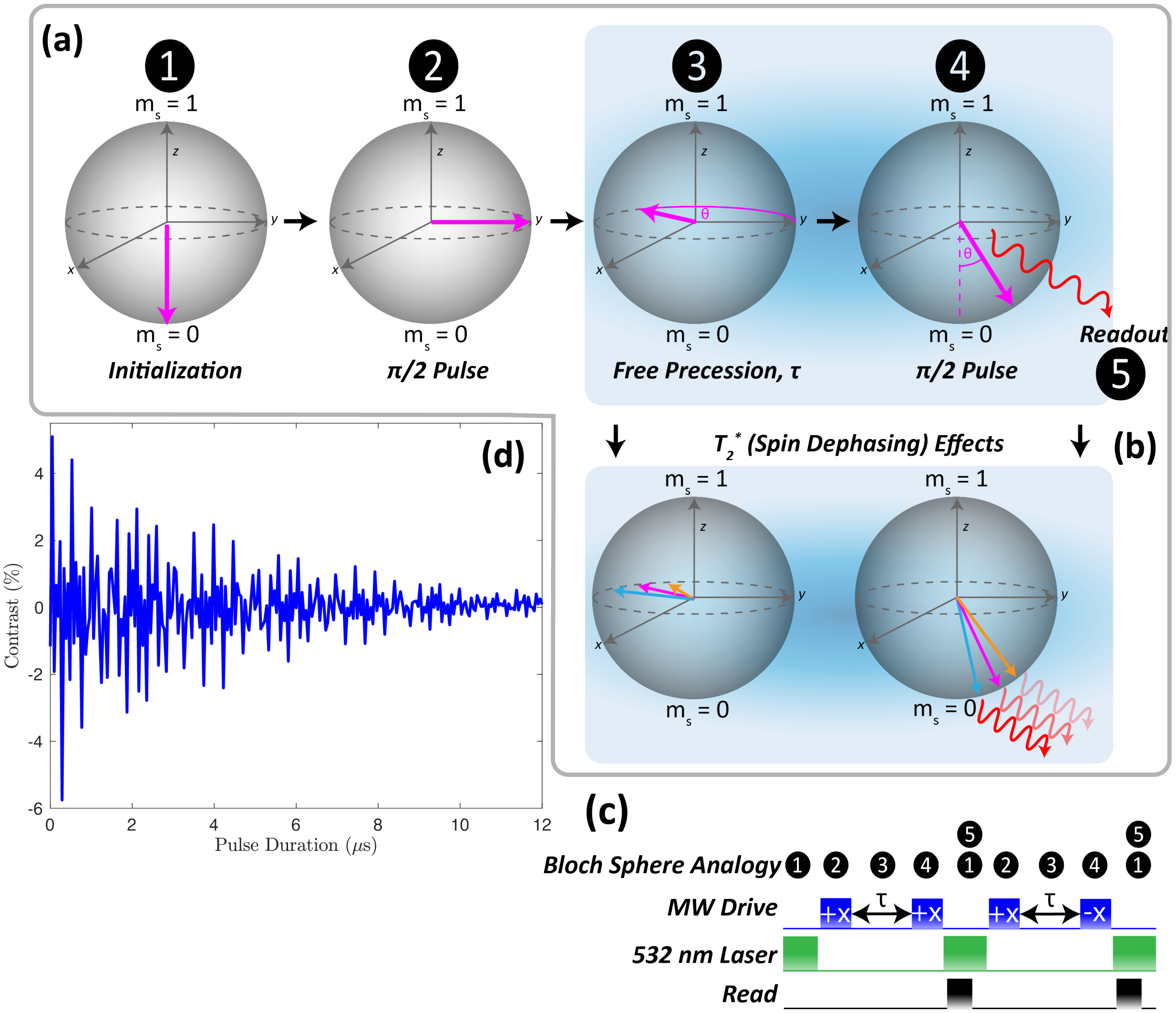

Figure 1.4: **(a) Bloch Sphere Analogy:** The NVs are initialized, and a $\pi/2$ pulse, calibrated via the Rabi sequence, prepares the spins into a superposition of the $m_s = 0$ and $m_s = +1$ states. The spins freely precess under the influence of $B = B_{\mathrm{local}} + B_0$ for time τ, after which they are projected back into the $m_s = 0$ and $m_s = +1$ manifold via another $\pi/2$ pulse. The phase accumulated spin state is then read out and the measurement repeats. **(b) T_2^* Mechanism:** Once prepared in the superposition, the spins precess at different rates due to variations in their environment. When mapped back into the $m_s = 0$ and $m_s = +1$ manifold, the measured fluorescence no longer correlates to B because the NV spin states are not coherent. **(c) Ramsey pulse sequence. (d) Ramsey data:** The plotted contrast is equal to $C = \frac{F_{x(y)} - F_{-x(-y)}}{F_{x(y)} + F_{-x(-y)}}$ and decays with characteristic time, T_2^*; T_2^* can be extracted by fitting the Ramsey fringe decay with $e^{{\frac{-\tau}{\mathrm{T}_2^*}}^{p}}$ [47,49].

1.3.2.1 Spin Echo

Similar to Ramsey, the spin echo sequence has two primary functions: (1) sense narrowband oscillatory signals [30,34,35], and (2) measure the NV diamond's characteristic spin coherence time, T_2 [30, 32, 34, 35, 47, 50]. Again, for the scope of this thesis, the spin echo sequence will be utilized for T_2 characterization, where T_2 decay is a consequence of spin decoherence due to time-dependent fields [35] and arises only after T_2^* effects have been eliminated by a refocusing pulse.

As like all other sequences, the NVs are initialized via 532 nm light and placed into a superposition of the $\mathrm{m_s} = 0$ and $\mathrm{m_s} = +1$ states with a $\pi/2$ pulse. The spins evolve for a free precession time, $\tau/2$, and accumulate phase at different rates due to DC effects (Section 1.3.1.3). To refocus the spins, a π pulse is applied to flip the spins. During the next evolution $\tau/2$, the spins precess back into a coherent spin state and ultimately accumulate some net phase ϕ. As a caveat, the refocusing efficacy depends on the rate of the DC dephasing sources; if the sources are slow compared to $\tau/2$, the π pulse effectively eliminates the phase differences [35,50]. The final $\pi/2$ pulse then projects the spins back into the $\mathrm{m_s} = 0$ and $\mathrm{m_s} = +1$ manifold, and the resultant spin state is readout. Akin to Ramsey, the sequence is repeated with different $\pi/2$ pulse phases such that the plotted contrast suppresses low-frequency $1/f$ noise [30,50]. With T_2^* effects eliminated, the spins are sensitive to oscillatory signals whose frequency match the filter response function produced by the π pulse [50]. This sensitivity ultimately causes the measured contrast to decay with approximate functional form $e^{\frac{-\tau}{\mathrm{T}_2}^{p}}$ [47, 49]. However, T_2 is typically several 10's of μs, which is at least an order of magnitude larger than T_2^* [30, 32, 34, 47]. As will be described in the following sections, the CPMG-M and XYN-M sequences, which are broadly called dynamical decoupling sequences, add additional π pulses to simultaneously extend T_2 and narrow the width of the filter response function [30, 34, 50].

1.3.2.2 Dynamical Decoupling: Carr-Purcell-Meiboom-Gill (CPMG)

The CPMG-M sequence is an extension of the spin echo; additional π pulses are centered between the $\pi/2$ pulses to repeatedly refocus the NV spins. This simultaneously extends T_2 and narrows the frequencies for which the NVs are sensitive to [30, 34, 35, 50]. The number of π pulses, M, can be increased arbitrarily until either (1) the theoretical T_2 limit of $2\mathrm{T}_1$ is reached (i.e. $\mathrm{T}_2 = 2\mathrm{T}_1$ where T_1 is the characteristic time for the NVs to return to thermal equilibrium [35]), or (2) the sequence duration itself approaches T_1[8].

---

[8] To the best of this author's knowledge, data corroborating statement (2) has not been published. However, it is behavior that has been observed in T_2 data collected in recent years.

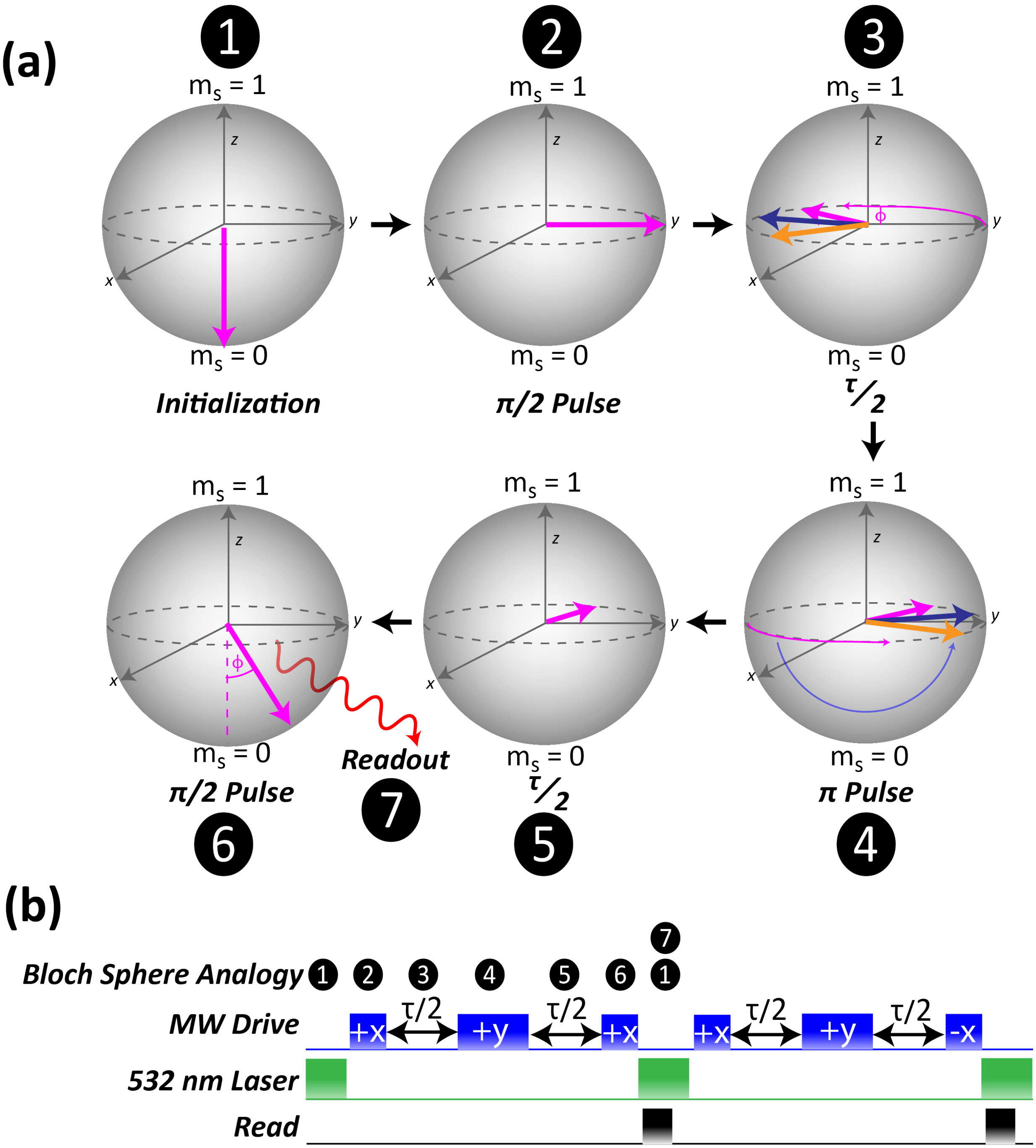

Figure 1.5: **(a) Bloch Sphere Analogy:** The NVs are initialized and prepared into a superposition of the $m_s = 0$ and $m_s = +1$ via a $\pi/2$ pulse, whose duration is calibrated with the Rabi sequence. Under the influence of DC and slowly varying fields, the spins precess at different rates for a time $\tau/2$. A refocusing π pulse is applied which flips the spins such that they precess back into a coherent state with net phase ϕ following another $\tau/2$ precession interval. Finally, another $\pi/2$ pulse projects the spins back into the $m_s = 0$ and $m_s = +1$ manifold, and the spin state is readout. Similarly to Ramsey, the sequence is repeated with different MW phases to suppress low-frequency $1/f$ noise [30, 34, 35, 50]. **Spin Echo pulse sequence.** The labels on the MW pulses refer to the pulse phase.

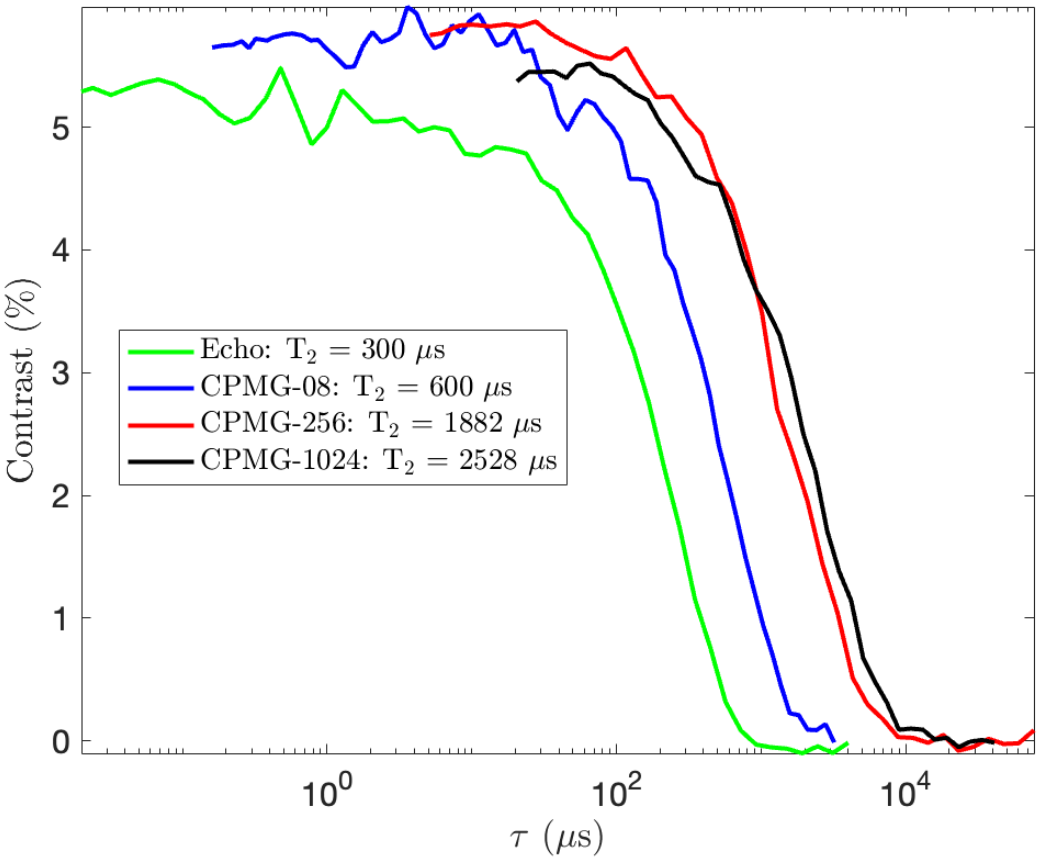

Figure 1.6: Depicts the T_2 for a spin echo, CPMG-08, CPMG-256, and CPMG-1024 sequence. As the number of π pulses increases, the T_2 increases.

1.3.2.3 Dynamical Decoupling: XYN-M

Similarly to CPMG, XYN-M extends T_2 and narrows the frequency filter with the addition of multiple π pulses. However, the XYN-M sequence applies π pulses with x and y rotations; rotations about both axes means XYN-M is robust to pulse errors along both axes when an even number of π pulses is applied. Conversely, the CPMG sequence is only robust to pulse errors along one axis [51].

The sequence itself can take on multiple forms depending on the value of N and M; N determines the π rotation pattern. For example, an XY4 sequence has the following pulse rotations [52]:

$$\pi_x \underset{\tau/2}{\Longrightarrow} \pi_y \underset{\tau/2}{\Longrightarrow} \pi_x \underset{\tau/2}{\Longrightarrow} \pi_y$$

Conversely, an XY8 sequence has eight π pulses with a phase pattern of [52] :

$$\pi_x \underset{\tau/2}{\Longrightarrow} \pi_y \underset{\tau/2}{\Longrightarrow} \pi_x \underset{\tau/2}{\Longrightarrow} \pi_y \underset{\tau/2}{\Longrightarrow} \pi_y \underset{\tau/2}{\Longrightarrow} \pi_x \underset{\tau/2}{\Longrightarrow} \pi_y \underset{\tau/2}{\Longrightarrow} \pi_x$$

The M variable details the number of times the phase pattern is repeated between the $\pi/2$ pulses. This means the total number of π pulses centered between the $\pi/2$ pulses is: $n = N \times M$. For instance, XY8-6 means there are 48 π pulses.

Chapter 2: Nuclear Magnetic Resonance (NMR)

2.1 NMR History

Today, Nuclear Magnetic Resonance (NMR) is a well-established analytic tool used throughout the biology, chemistry, and physics disciplines. Its storied history began in 1946 with physicists at Stanford [53] and Harvard [54] who independently, and within weeks of each other, demonstrated NMR of bulk materials. While they hoped to use this new tool to more accurately measure gyromagnetic ratios, they struggled to do so as the measured resonance features were askew from their predicted locations. This annoyance, later coined chemical shift, was the historical marker that catapulted NMR into chemical and biological applications [55].

The next several decades saw incredible technological developments for NMR spectroscopy. Examples of these innovations include the commercialization of highly homogeneous and temporally stable superconducting magnets, the use of Fourier transform for data processing, development of novel pulse sequences [56–60], enhanced RF coil fabrication and design [61, 62], and creation of NMR imaging, colloquially referred to as magnetic resonance imaging (MRI) [55]. These technological advancements established NMR spectroscopy as an essential analytic tool for solid, liquid, and gas systems; NMR has been enormously useful in a wide variety of applications such as identifying chemical structure, observing real-time chemical reactions and molecular dynamics (e.g. relaxation, cross-relaxation, chemical exchange) [55, 63], measuring in-vivo (e.g. living cells, tissues, and whole animals and humans) [55], and identifying human diseases (e.g. MRI) [63]. The breadth of knowledge made available because of NMR is far too extensive to encapsulate in this thesis, but hopefully, this brief synopsis highlights the debt modern day knowledge owes to NMR.

2.2 The Basics of NMR Spectroscopy

NMR spectroscopy relies on sensing the Larmor precession frequency, ω_L, which is the frequency a magnetic moment precesses around an applied magnetic field B_0:

$$\omega_L = -\gamma_I B_0$$

The application of B_0 causes the sample to become polarized, i.e. a net nuclear magnetic moment, or nuclear magnetization, is produced in the same direction as B_0. This is otherwise referred to as nuclear polarization, and there are two types: (1) thermal polarization (otherwise called Boltzmann) and (2) statistical polarization. Thermal polarization arises from vigorous motion of molecules in thermal equilibrium which generates a net magnetization in the same direction as B_0 [64]; typically, thermal polarization dominates over statistical in micro (or larger) samples [65]. Conversely, statistical polarization is a result of statistical variations in the net nuclear magnetization; it dominates in nano-sized (or smaller) samples[1] [65]. The work in this thesis involves only micro-sized (or larger) samples, so only thermally polarized NMR will be derived.

---

[1] The work in Chapters 4, 5, and 6 assume a thermally polarized system, so only thermal polarization is derived. However, for completeness, the following expression is the measure of the statistical variation of the net magnetization, M: $\sigma_M = \sqrt{\frac{N\hbar\gamma_I}{4}}$. The interested reader is referred to [65] for additional information.

Mathematically, thermal polarization is a consequence of Boltzmann distribution where the probability, $P(E_n)$, of a spin being in a certain energy eigenstate E_n is defined as:

$$P(E_n) = \frac{exp(-E_n/k_BT)}{\sum_n exp(-E_n/k_BT)}$$

where k_B is the Boltzmann constant and T is the temperature. For a spin-1/2 system under the influence of B_0, the net magnetization, M, is defined as the sum of the N nuclear magnetic moments per unit volume [64, 66, 67]:

$$M = N\gamma_I\hbar\frac{\sum_{-1/2}^{+1/2} n\exp(\gamma_I n\hbar B_0/k_BT)}{\sum_{-1/2}^{+1/2}\exp(\gamma_I n\hbar B_0/k_BT)}, \tag{2.1}$$

Operating with the assumption that $\frac{\gamma_I\hbar B_0}{k_BT} \ll 1$, the exponential terms can be approximated with a Taylor series expansion and the net magnetization simplifies to [64–67]:

$$M = \frac{N\gamma_I^2\hbar^2 B_0}{4k_BT} \tag{2.2}$$

Equation 2.2 demonstrates there is a linear proportionality between the nuclear magnetization and B_0. Not only is this proportionality why most NMR systems operate at large fields, but it is also why most NMR experiments actually measure the transverse magnetization; longitudinal magnetization is incredibly difficult to measure because the magnitude of M is orders of magnitude smaller than B_0 [64, 65]. To ease the measurement difficulty, the longitudinal polarization is transferred to the transverse plane (i.e. the plane perpendicular to B_0) via a $\pi/2$ pulse (Figure 2.1). After the pulse, the net moment also precesses at ω_L around B_0. Fortunately, a rotating magnetic moment can be measured with an RF coil because a rotating magnetic moment produces a rotating magnetic field. Due to Maxwell's equations, the rotating magnetic field produces an electric field which then generates an oscillating electric current in a nearby RF coil. The current is then digitized, and the resulting data is the NMR signal, or free induction decay (FID) of the nuclear magnetization (Figure 2.1), which has the form [64]:

$$M = M_x + M_y = M_{eq}e^{-t/\mathrm{T}_2^*}[\sin(\omega_0 t) - \cos(\omega_0 t)] \tag{2.3}$$

Once collected, an FFT (Fast Fourier transform) is done to extract the resonance frequencies from the FID. However, the convention in the NMR community is to plot chemical shift in units of ppm rather than the resonance frequency. Nuclear spins in a molecule have spatially different environments which yields slight variations in the magnetic field experienced by each spin. These variations shift that nuclear spin's Larmor frequency from the expected one, thus giving rise to the term *chemical shift*. Unfortunately, like M, the magnitude of the chemical shift is linearly proportional to B_0[2], thus it is difficult to compare NMR spectra at different fields and between experiments. To eliminate the dependence of chemical shift upon B_0, the data is normalized to some some reference compound, typically TMS (tetramethylsilane). Chemical shift, δ, can then be defined as:

$$\delta = \frac{\omega_L - \omega_L^{\mathrm{TMS}}}{\omega_L^{\mathrm{TMS}}}, \tag{2.4}$$

where ω_L^{TMS} is the nuclear spin's Larmor frequency in the reference compound when exposed to the same B_0 [64].

---

[2] This is another reason why NMR spectrometers often operate at large magnetic fields; a larger magnetic field produces larger chemical shifts which limits the overlap between signal peaks.

In addition to chemical shift, NMR spectra exhibit multiplet splitting from J-coupling, or indirect dipole-dipole coupling (Figure 2.1). While chemical shift is a net shift in the expected Larmor, J-coupling is a splitting of the resonance feature into multiple, closely spaced features. These multiplets occur when nuclear spins magnetize the electrons in the atomic bonds; in turn, this generates a magnetic field which neighboring spins experience, thus slightly altering their Larmor frequency [64].

Thankfully, the aforementioned chemical shifts and J-couplings have been well-researched over the last decades, and a sample's molecular structure can be elucidated based on the location of these features, assuming the features have not been broadened as a consequence of differences in magnetic susceptibility or a spatially and temporally inhomogenous B_0 [64].

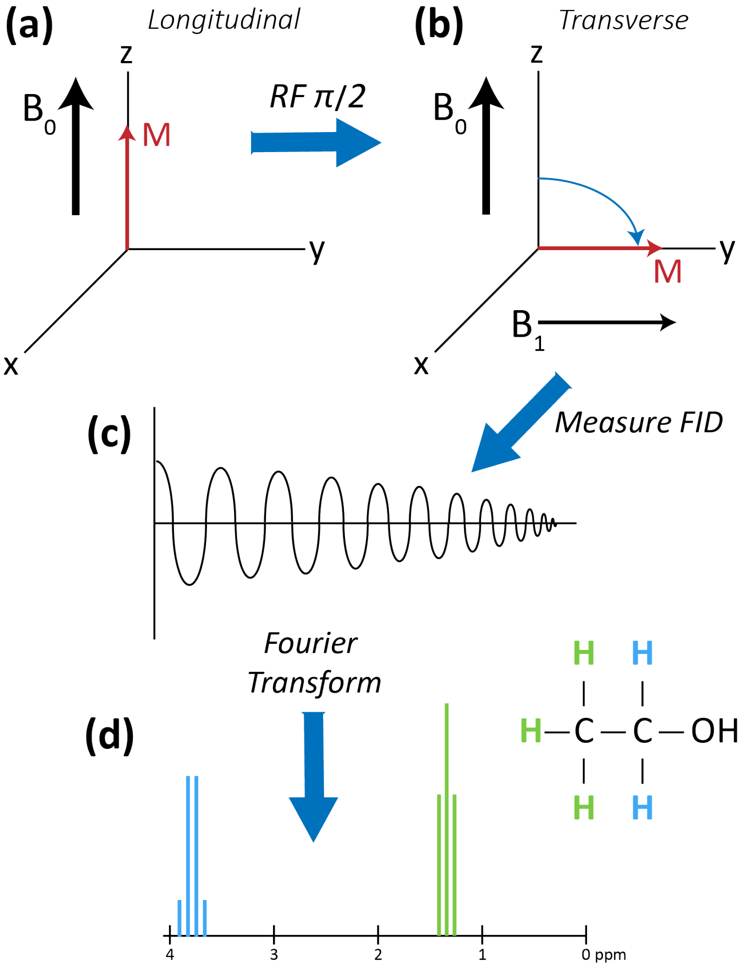

Figure 2.1: Summarizes the basic structure for thermally polarized NMR measurements. First, an applied B_0 generates a net nuclear magnetization, M, in the same direction. This longitudinal magnetization is then rotated to the transverse plane by a RF $\pi/2$ pulse. Following the RF pulse, the magnetization precession around B_0 at frequency ω_L is measured by a nearby RF coil. The measured data, the FID, is then Fourier transformed to extract the resonance features of the sample. Here, the chemical shift and J-couplings are depicted for ethanol.

2.3 Associated Challenges

Unfortunately, all measurement tools have advantages and disadvantages, and NMR spectroscopy is no exception. Arguably, the largest disadvantage is the limited sensitivity [68]. As described previously (Equation 2.2), the measured magnetization is linearly proportional to B_0 [65], but a magnetic field cannot be arbitrarily increased without bound and large magnets consume both space and money [63, 69]. Unfortunately, the magnet consumption costs dramatically limit NMR accessibility. While there are alternative analytic tools that consume less financial resources, like bench-top NMR systems [70] or mass spectrometry, they bring with them their own problems which limit their sensitivity or limit the application space [63,69]. Other than increasing the magnetic field, nuclear spins can be hyperpolarized (e.g. artifically increased polarization) to increase the measurement sensitivity via methods like Overhauser DNP (Dynamic Nuclear Polarization), PHIP (ParaHydrogen Induced Polarization), SEOP (Spin-Exchange Optical Pumping), or SABRE (Signal Amplification By Reversible Exchange) [71]. However, these polarization methods also have disadvantages such as the enhancement is generally on the order of a percent, time-consuming, and/or financially expensive [71]. Another method to enhance sensitivity is to increase the sample's concentration by simply increasing the amount of sample. Yet again, this is a resource consumption that many application spaces cannot afford to make (e.g. single cellular studies, human studies of blood or tissue, etc.) [63]. Finally, the complexity associated with maintaining/operating the spectrometer and analyzing the data requires operators to be highly skilled and trained, thus further limiting the tool's accessibility [63].

2.4 NV Centers as an Alternative

In recent years, NV centers have emerged as an alternative NMR sensor. Notably, NV experiments are significantly cheaper than conventional NMR systems because it is not necessary to have superconducting magnets. Additionally, the NV sensing volume is on the order of 10 pL due to the inherent size of the NV center itself, thus the required sample is orders of magnitude smaller than the conventional system's 5 - 10 mL [9, 10, 12]. This smaller sample volume also opens up application spaces unavailable to conventional NMR, such as nanoscale diffusion [24], surface chemistry [72], and characterizing boundary interactions and metabolic consumption/production rates for cancerous tumors or tumor-like objects [73]. With additional development of NV-based nanodiamonds, there is also potential for NMR inside living systems [74].

Again, like conventional NMR, NV-NMR is not without its challenges, particularly involving NV-NMR sensitivity because increasing B_0 yields a host of MW and RF engineering challenges. As mentioned in Section 1.1, the NV spin state requires manipulation via MWs, and homogeneously delivering high frequency, high power MWs is an engineering challenge that gets seemingly exponentially harder with larger magnetic fields. For example, let's assume a magnetic field of 2 T, which is on the low-end for conventional NMR spectrometers [55, 70]. At this field, the MW frequency for the NV's $\mathrm{m_s} = 0 \longleftrightarrow \mathrm{m_s} = +1$ transition is:

$$28\frac{\text{GHZ}}{\text{T}} \times 2\text{T} + 2.87\text{GHz} = 58.87\text{GHz}$$

Now, the nuclear Larmor frequency for ^{1}H at this field is:

$$\omega_L = 42.57\frac{\text{MHz}}{\text{T}} \times 2\text{T} = 85.14\text{MHz}$$

To sense this signal using the dynamical decoupling sequences (Section 1.3.2.2 or 1.3.2.3), the π pulses need to be applied at a rate of $2\omega_L = 170.28$MHz, which corresponds to a π pulse every 5.87 ns. Let's assume we want our π pulse duration to be 2 ns. To have a 2 ns π pulse, our Rabi frequency needs to be 500MHz. In summary, to operate at 2 T, we need to homogeneously deliver a roughly 59GHz MW with a Rabi strength of 500MHz across the NV sensing volume.

Unfortunately, these specifications are incredibly challenging to achieve. Therefore, NV-NMR sensitivity cannot be easily increased merely by increasing B_0. Besides increasing the applied B_0, there are have been a variety of mechanisms attempted to improve sensitivity such as the development of novel pulse sequences [8,16,75] and hyperpolarizing the sample with DNP [10], SABRE [9], or transferring the NV polarization to the nuclear spins [76–80]. Another method is to polarize the ^{13}C atoms in the diamond using the NV centers and then sense the NMR signal of either a sample or the ^{13}C spins themselves [81–84].

Chapter 3: Progress of NV-NMR Experiments

Even with the sensitivity limitations mentioned in the previous chapter, there have been a host of application-based NV-NMR demonstrations. Broad descriptions of some of these demonstrations are itemized below:

- quantitatively imaging molecule diffusion and flow in microstructures [24]
- measuring a diamond's hyperpolarized ^{14}N at high pressure (e.g. 16.6 GPa) [85]
- quantifying molecular coverage and binding in self-assembled monolayers on the surface of diamond [72]
- detecting individual protons in single proteins attached to the diamond surface [13]
- characterizing relative distances and depths of NV centers using a scanning-field-gradient MRI mechanism [86]
- NV-MRI of dark spins on the diamond surface [87]
- an all-optical method to measure a single paramagnetic molecule localized on the diamond surface [88]
- detecting protons by measuring the magnetic-dipole interaction between the NV center and electrons on the diamond surface [89]

- 2D NV-NMR spectroscopy to determine nuclear spin coupling and the spins relative positions [90]
- extracting the NV center depth with a NV-NMR spectrum from statistically polarized protons [91]
- using an MRI inspired frequency encoding method to selectively control spatially separated clusters of NVs [92]
- MRI of magnetotatic bacteria [7]

To better express the technical realities of NV-NMR and highlight the areas that need continued improvement, Table 3.1 summarizes the experimental results from several of the aforementioned papers. This table demonstrates that the sensitivity has remained relatively constant in recent years, but that the measured linewidths have improved several orders of magnitude from 2013. In fact, NMR linewidth was dramatically decreased with the advent of the CASR sequence in 2018 by Glenn et. al and is projected to be even smaller with the AERIS/DRACAERIS sequence [16]. Additionally, the AERIS/DRACAERIS sequence [16] is simulated to operate at the largest magnetic field reported thus far for ^1H NMR which would could largely improve the NV-NMR sensitivity. To better understand these past and future improvements, the following sections will discuss the CASR and AERIS/DRACAERIS sequences.

3.1 CASR

Arguably one of the most ground-breaking NV-NMR experiments in recent years was by Glenn et al. in 2018 in which they measured linewidths on the order of Hz using a sequence entitled Coherently Averaged Synchronized Readout, or CASR [12]. [1]

The CASR sequence is composed of concatenated NV magnetometry sequences, such as CPMG (1.3.2.2) or XYN-M (1.3.2.3), followed by a readout. The readout is synchronized such that the measured fluorescence is some downconverted frequency of the nuclear Larmor; this timing is calculated via $\tau_{\text{SR}} = k/f_0$, where f_0 is the frequency the magnetometry sequence is sensitive to and k is some integer number of periods of f_0.

To induce the measurable Larmor precession of the nuclear spins ($f_L = \omega_L/2\pi$), a $\pi/2$ pulse is applied to transfer the longitudinal magnetization to the transverse. The NVs are then used to read this oscillating nuclear spin state; the resulting data is a downconverted FID with frequency $\delta f = f_L - f_0$ [12] (Figure 3.1).

---

[1] Note, an equivalent sequence, historically used for single-NV experiments, is called Qdyne [19].

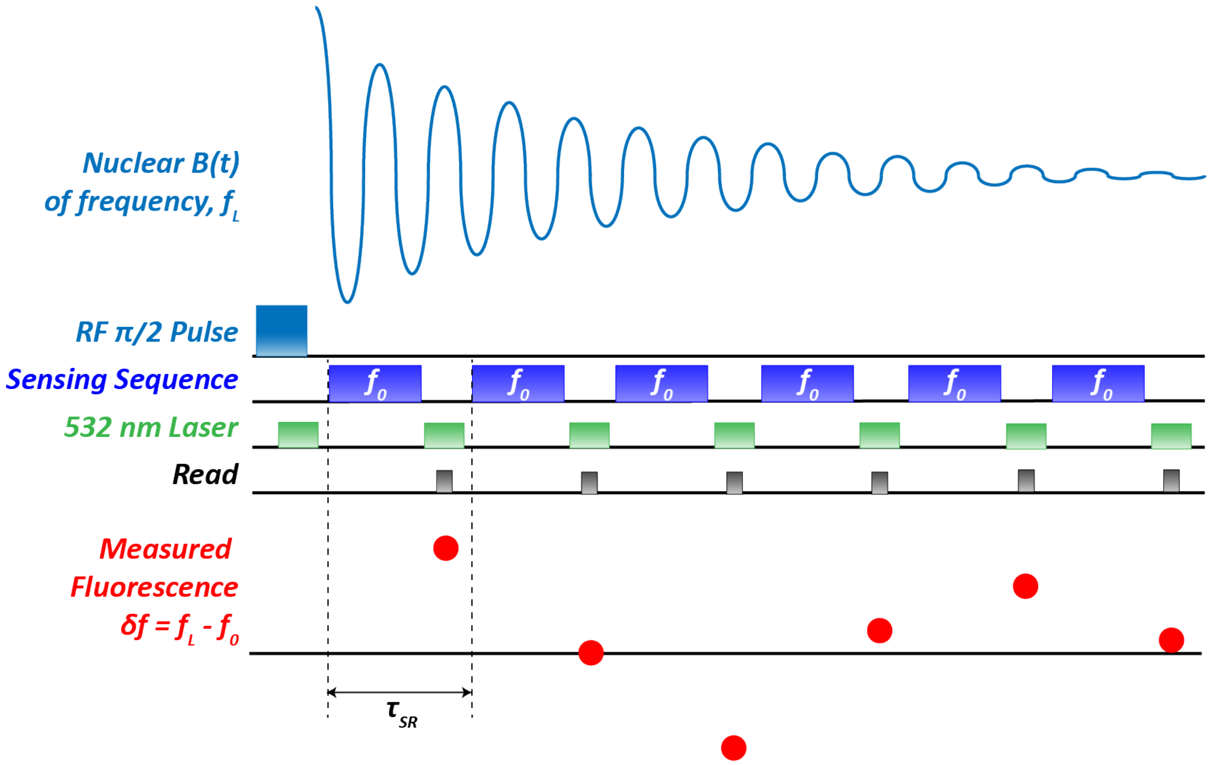

Figure 3.1: Depicts the CASR sequence. First, a RF $\pi/2$ pulse rotates the longitudinal nuclear magnetization to the transverse plane which produces an oscillating nuclear $B(t)$ of frequency f_L. The NVs are then initialized with a 532 nm pulse, and then subjected to a magnetometry sequence sensitive to frequency f_0. The NV spin state is then readout via another 532 nm pulse. The NV magnetometry sequence and readout is repeated every τ_{SR} until $B(t)$ decays. The resultant measured signal is a downconverted FID with frequency $\delta f = f_L - f_0$ [12].

Utilizing this sequence, at a $B_0 = 88$mT and with a 10 pL NV detection volume, Glenn et al. measured a pure water's proton peak with a FWHM (Full Width at Half Maximum) linewidth of 2.8 ± 0.3Hz [12]. The sublety as to why this sequence is able to achieve such small linewidths is that the NVs sense only during the magnetometry sequence, so the spectral resolution is limited by the nuclear spin decoherence (i.e. nuclear T_2^*) which is orders of magnitude larger than the NVs intrinsic T_2 [16].

3.2 AERIS/DRACAERIS

The AERIS (or DRACAERIS) sequence, which stands for Amplitude Encoded Radio Induced Signal (or Double Rewind ACquisition Amplitude Encoded Ratio Induced Signal), is a novel sequence theorized to increase NV-NMR sensitivity by increasing the applied magnetic field (i.e. increasing the thermal polarization) without equally increasing the MW engineering challenges [16, 93].

Figure 3.2 depicts the AERIS/DRACAERIS sequence. First, a $\pi/2$ pulse is applied to the thermally polarized nuclear spins to transfer the magnetization to the transverse plane. Immediately following, the spins precess at their Larmor frequency, ω_L, around the applied external field during the free precession interval, τ. Due to slight variations in the magnetic field experienced by the nuclear spins (i.e. from chemical shift and J-coupling), the spins accumulate different phases, ϕ_k, where k represents the nuclear spin. Following τ, an NV magnetometry sequence and a long RF pulse, coined induced rotation, are simultaneously applied. The induced rotation rotates the spins so they precess around B_1, which is the magnetic field generated by the RF pulse, and the spins precess with an oscillation amplitude corresponding to their accumulated ϕ_k. This precession about B_1 induces a nuclear magnetic field, $B(t)$, that oscillates at B_1's Rabi frequency, Ω. After N periods of $B(t)$, the RF radiation's phase is reversed ($+\Omega \rightarrow -\Omega$) and another magnetometry sequence is applied; this phase cycling eliminates phase errors that have accumulated from pulse errors [16] and the presence of chemical shift and J-coupling during the induced rotation [93] (*manuscript in preparation*). This reverse drive is applied for another N periods, and then the process is repeated until the nuclear spins thermally relax [16] (i.e. T_1 [35]).

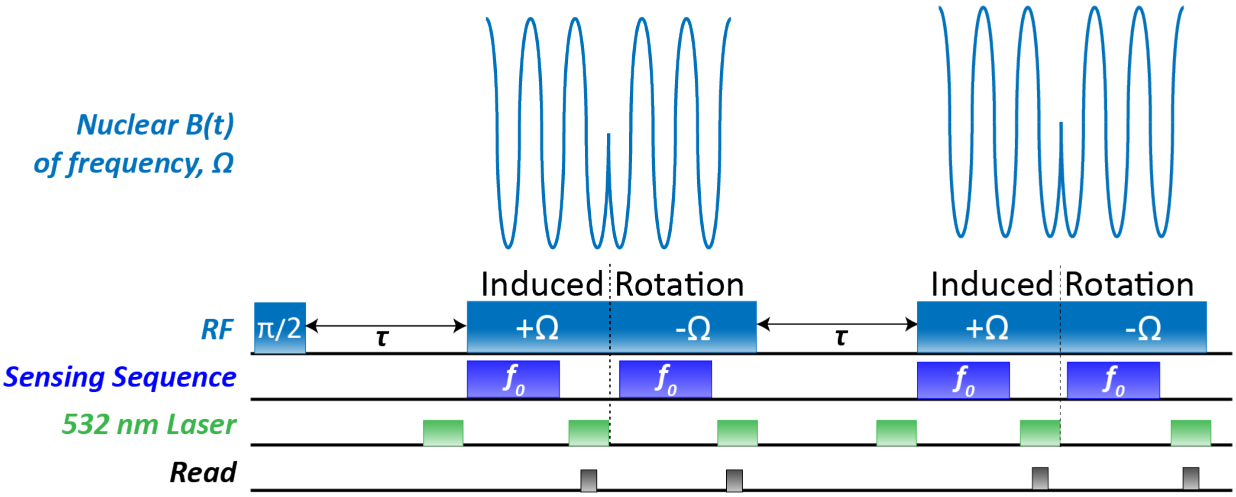

Figure 3.2: Depicts the AERIS/DRACAERIS sequence. First, a RF $\pi/2$ pulse rotates the magnetization to the transverse plane, and the nuclear spins are then allowed to freely precess for a time τ and accumulate phase, ϕ_k, where k refers to the kth nuclear spin. Then, an NV magnetometry sequence and induced rotation RF pulse of magnitude B_1 are simultaneously applied. The induced rotation induces a nuclear magnetic field $B(t)$ that oscillates at B_1's Rabi frequency. After N periods of $B(t)$, the B_1's phase is reversed and another magnetometry sequence is applied for N periods of $B(t)$.

There are two important subtleties associated with this sequence. First, the NVs sense only during the induced rotation, so the spectral resolution is again limited by the nuclear spin decoherence (i.e. T_2^*) rather than the NVs intrinsic T_2 [16]. Second, $B(t)$ oscillates at the induced rotation's Rabi frequency rather than the nuclear Larmor frequency.

To understand the benefit of $B(t) \propto \Omega$, consider an NV-NMR experiment at 2T. As derived in Section 2.4, the ^{1}H nuclear Larmor frequency is approximately 85 MHz. For an NV to sense this signal, a π pulse needs to be applied about every 6 ns. Assuming a π duration of 2ns, the MW Rabi strength must be 500MHz. Additionally, the $\mathrm{m_s} = 0 \longleftrightarrow \mathrm{m_s} = +1$ NV transition is 58.87 GHz. This means that the MW pulses must be delivered at about 60GHz with a 500MHz strength.

Now, let's consider the alternative: NVs sensing a 300kHz signal which is of typical magnitude order for a B_1 Rabi frequency [33]. The π pulses need to be spaced at a rate of:

$$2 \times 300\text{kHz} = 600\text{kHz}$$

Thus, there needs to be a π pulse about every 1.6μs. This means the π pulse can be significantly longer; let's assume a 300ns pulse which corresponds to a Rabi strength of 3.3MHz. Although the NV transition is still about 60GHz, now the Rabi strength only needs to be about 3MHz. Although this MW delivery is still a technical challenge, it is a far easier challenge than a 60GHz signal with a 500MHz strength!

Therefore, the AERIS/DRACAERIS sequence can increase the nuclear magnetization by several orders of magnitude (Equation 2.2), thus increasing the NV-NMR sensitivity and expanding the application spaces available to NV-NMR.

Table 3.1: Reports the sensing sequence, sample, acquisition time (T), applied magnetic field (B), linewidth ($\delta\nu$), NV measurement sensitivity, and relevant notes for several NV-NMR experiments. The lime colored rows are statisically polarized systems and the pink row is the result of simulated data only.

Paper (Year)	**Sequence**	**Sample**	**T (s)**	**B (mT)**	$\boldsymbol{\delta\nu}$	**NV sens. (pT/$\sqrt{\text{Hz}}$)**	**Notes**
[16, 93] (2023)	AERIS (DRA-CAERIS)	Ethanol	1.56	2.1 T	1.62	N/A	see Sec., NMR information in signal amplitude.
[8] (2022)	QLE	3-tone signal at 1 MHz	0.001361	370	N/A	≈ 20	Droid-60 [94] and 400 readouts, then 5.6 ± 0.3 enhanced sensitivity.
[9] (2021)	CASR	100 mM pyridine	2	6.576	2.3 ± 0.5 Hz	35 ± 2	Spins polarized via SABRE ($= 0.5\%$ polarization in 10 pL).
[10] (2020)	CASR	*tert*-butanol in D_2O	5000	84.7	13 Hz (3.55 ppm)	20	Sample spins polarized via DNP ($= 126 \pm 5$ signal enhancement)
[12] (2018)	CASR	Water	3.9×10^4	88	2.8 ± 0.3 Hz	32 ± 4	Original CASR demonstration.
[19] (2017)	Qdyne	Polybutene	–	8.8×10^{-4}	2 kHz	–	Single NV
[91, 95] (2015, 2016)	XY8-64 (XY8-32)	Immersion Oil	–	15 (15.6)	≈ 5 kHz (≈ 30 kHz)	–	Single NV. $\delta\nu \simeq 5$ kHz (30 kHz) is approx. 10 nm (4 nm) deep NV.
[96] (2013)	XY8-112	PMMA	–	20	46.3 ± 1.5 kHz	–	(5 nm)^3 sample volume.
[97] (2013)	Spin Echo	PMMA	–	79.5	20 kHz	–	(24 nm)^3 sample volume. Multiple RF $\pi/2$ pulses.

Chapter 4: Characterization of NV-NMR Experiment Sensitivity

The previous chapter expounded upon the great sensitivity enhancements made available by the AERIS/DRACERIS protocol. However, this conclusion assumes that this sequence works as effectively as simulated. Hence, this chapter first assesses the sensitivity of a previously used NV-NMR experiment ([8–10,12]) and then details the problems that need resolved and enhancements necessary to make a previously used NV-NMR experiment sensitive to the B_1 Rabi signals of the AERIS/DRACAERIS protocol so as to test the effectiveness of the protocol.

4.1 Experimental Layout

The experimental layout is comprised of (1) the optical pathway which directs the 532 nm beam into the sample area and collects the red fluorescence, and (2) the electronics which control the experiment.

4.1.1 Optical Pathway

A high power 532 nm laser beam (**Coherent Verdi-V5, 5 W**) first travels through a Half-Wave Plate (HWP)(**VitroCom**) and BeamSplitter (BS)(**Thorlabs: CCM1-PBS251**); this combination finely adjusts the laser power entering the Acousto-Optic Modulator (AOM)(**Gooch and Housego: 3250 – 220, S/N, 174163**).

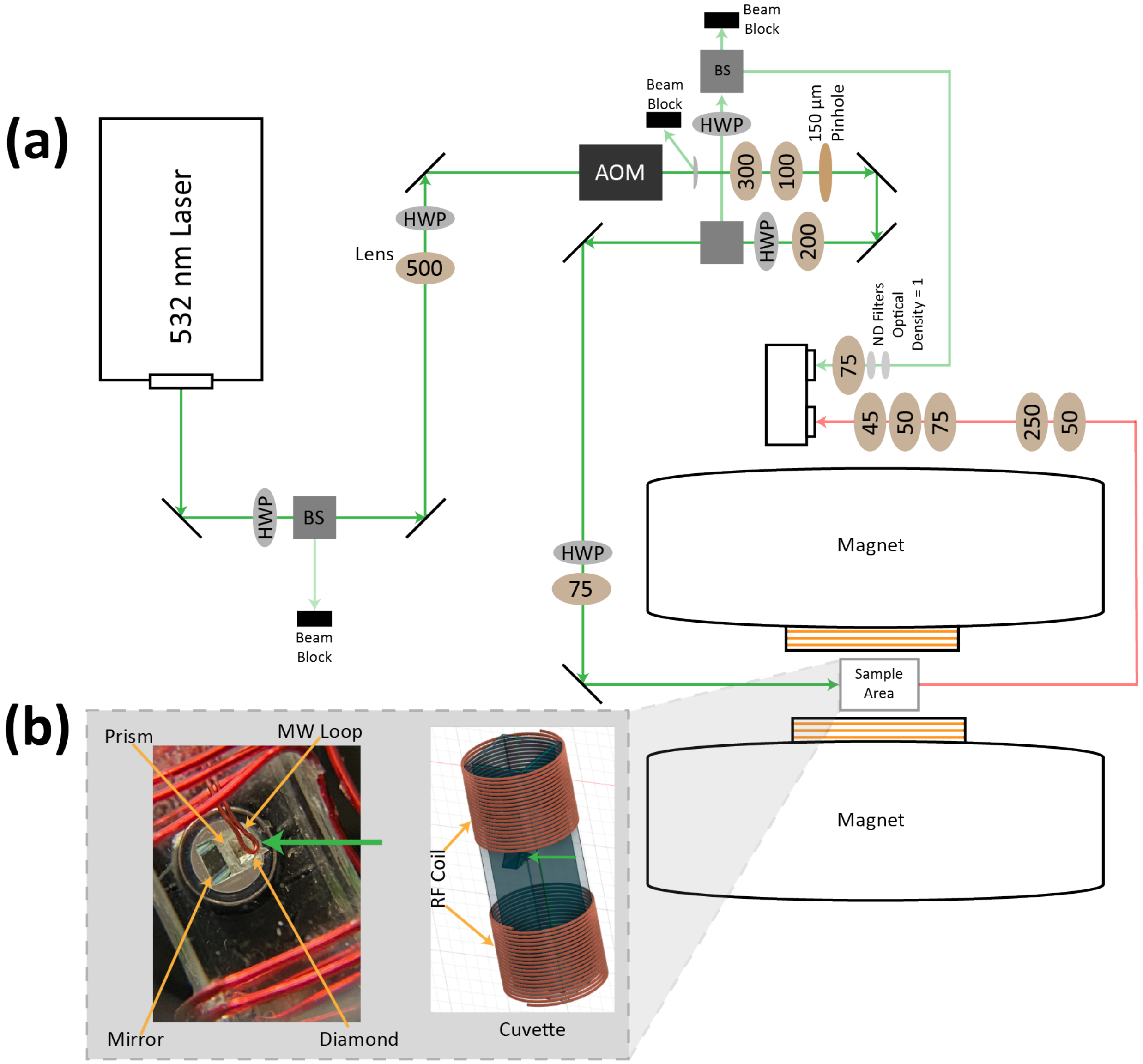

Figure 4.1: **(a) Optical Pathway:** Depiction of the 532 nm beam's pathway to the sample area and the collection pathway of the red fluorescence. The abbreviated optic components are Half-Wave Plate (HWP), BeamSplitter (BS), and AOM (acousto-optic modulator). The lenses are abbreviated by their focal length in mm. **(b) Sample Area:** CAD model of the cuvette and a close-up image of the diamond and MW loop inside the cuvette.

Broadly, the AOM allows the user to pulse the laser. When exposed to an electric current, a piezoelectric transducer generates an acoustic wave which in turn generates a refractive index grating in the nearby quartz (or quartz-like) material. Once exposed to this grating, the AOM material diffracts the beam; most of the output power is in the first-order diffraction. In this setup, the first-order beam is the beam that is allowed to propagate through the setup, while the zeroth-order is separated and dumped into a beam dump. Thus, when the AOM is off (i.e. no electric current driving the transducer), no significant beam power propagates through the setup. Once a beam is focused onto the quartz material, there are three quantities that define the AOM's efficacy: diffraction efficiency, rise time, and extinction ratio. The diffraction efficiency is defined as the percent ratio of the powers of the first-order diffraction and the beam into the AOM. The highest recorded diffraction efficiency for this AOM was $\approx 90\%$. The rise time, defined as the time for the AOM to respond to an applied pulse, can be measured as follows: A user defined pulse, with specified amplitude and frequency, is applied to the AOM. The first-order diffraction is measured with a photodiode and displayed on an oscilloscope. The rise time can then be observed on the oscilloscope. The measured rise time was ≈ 30 ns which is expected for this AOM. Finally, the extinction ratio is defined as the ratio of the first-order diffraction's power when the AOM is on and when the AOM is off; the measured extinction ratio was on the order of 10^5 which is also as expected for this AOM.

Returning to the optical pathway, a 500 mm focal length lens focuses the beam into the AOM and a second HWP adjusts the beam's polarization. With this AOM, the beam's polarization has a significant impact on the achievable diffraction efficiency; a 40% diffraction efficiency was measured without the HWP, while an 80% efficiency was measured with the HWP[1]. The zeroth-order diffraction is picked off via a D-mirror (**Thorlabs: BBD1-E02**) and the first-order is re-collimated with a 300 mm lens (**Thorlabs: LA1484-A**). Then, a 100 mm lens (**Thorlabs: LA1509-A**) focuses the beam into a 150 μm pinhole (**Thorlabs:P150CB**) which acts as a spectral filter (i.e. cleans the Gaussian profile of the beam by eliminating some of the Gaussian tail).

---

[1] Comparison was made under the same experimental conditions and AOM alignment.

The beam is then re-collimated with a 200 mm lens (**Thorlabs: LA1708-A**). Using another HWP and BS, part of the beam is picked off and directed towards a balanced photodiode. On this pick-off path, another HWP and BS is used to adjust the beam's power into the photodiode. The remainder of this 532 nm pick-off path will be discussed shortly.

The main beam goes through another HWP, which adjusts the beam's polarization, and the beam is then focused with a 75 mm lens (**Thorlabs: LA1608-A**) into the sample area inside an electromagnet (**air-cooled Newport Instruments Type A**).

An expanded view of the sample area is demonstrated in Figure 4.1**(b)**. Using assorted optic components, a cuvette is held such that it can be rotated in the directions depicted. Wrapped around the cuvette is $\approx$ 24 AWG (American Wire Gauge) wire; the wire is the RF coil used to drive the sample's nuclear spins. Glued to the wall of the cuvette is the diamond system comprised of a prism, mirror, diamond, and MW loop. The prism was specially designed to be $36.3°$ relative to the interior wall of the cuvette so as to facilitate alignment of the diamond to one of the NV orientations inside the electromagnet's fixed magnetic poles. The diamond sits on top of this prism, and a mirror is placed on the wall of the prism so as to direct red fluorescence from the diamond to the liquid light-guide outside the cuvette. The MW loop is 1671A Tin 15 MTR, conformable coax, 50 Ohms, 24 awg wire, and is made into a coil and soldered by hand. The diamond currently being used is a 2×2 mm angle-polished, 10 μm ^{15}N layer on EL (ELectronic-grade) substrate[2].

The red fluorescence is ultimately collected by a liquid lightguide **Thorlabs: LLG5-6H** which directs fluorescence to the balanced photodiode (**Thorlabs: PDB210A**)[3]. To collimate

---

[2] The diamond is referred to as Arya Stark, and the diamond's material characterization data can be found in Appendix A.

[3] The balanced photodiode is used as it minimizes (or eliminates) common mode noise, such as laser noise.

the red fluorescence after the liquid lightguide a 50 (**Thorlabs: LA1131-A**), 250 (**Thorlabs: LA1461-A**), 75 (**Thorlabs: LA1608-A**), another 50, and a 45 mm (**Thorlabs: AC254-045-A-ML**) lens, respectively, are used. The green pick-off, mentioned previously, is focused onto the photodiode with a 75 mm lens, and the power input is further reduced by two ND filters of optical density 1 (**Thorlabs: ND10A**). Finally, the balanced output of the photodiode, ΔV_{PD} (or the difference between the measured red fluorescence and green pick-off) is directed to the DAQ which converts the electrical signal into a digital one.

4.1.2 Electronics

The experiment synchronization is controlled by the Arbitrary Waveform Generator (AWG) (**Texktronic AWG 7122c**) in which the user uploads pulse sequences generated in Matlab to the AWG in discretized steps of its 12 GHz clock frequency. There are two experiments that can be performed using this setup: (1) NV-based (i.e. ESR, Rabi, NMR, etc.), and (2) Inductive NMR.

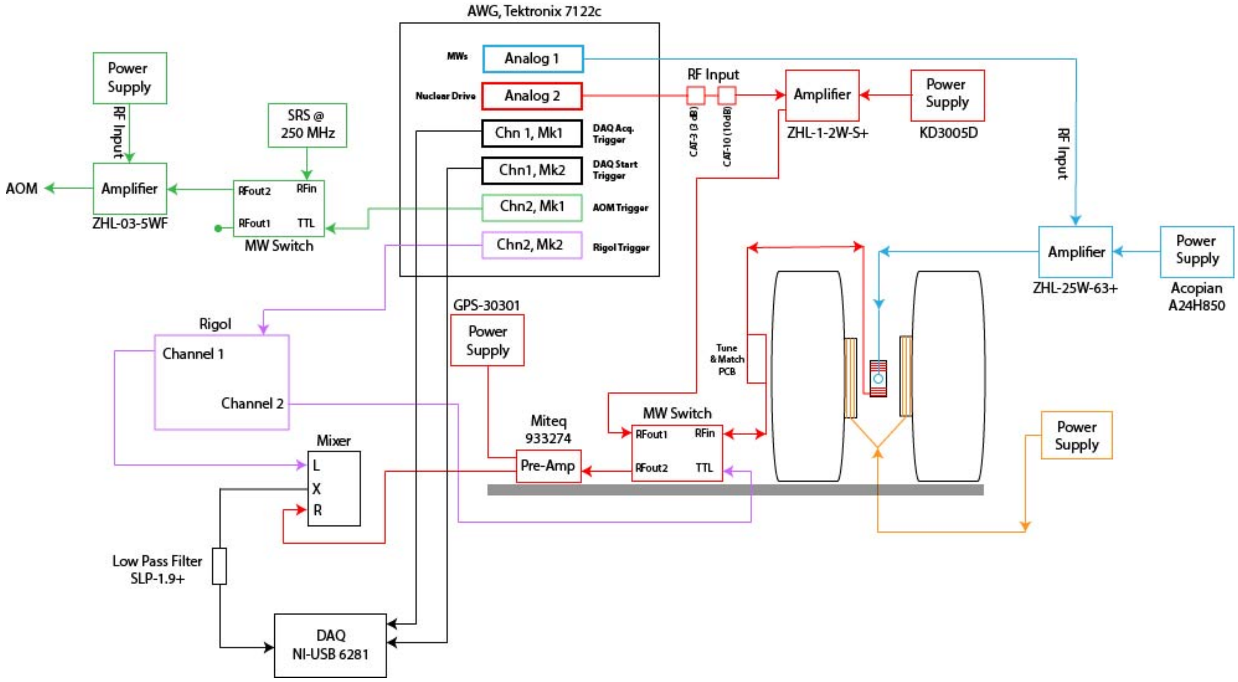

Figure 4.2: Depicts the electronic components necessary for both NV-based and inductive NMR experiments.

4.1.2.1 NV Experiments

The following section summarizes the AWG controls and electronic components for the NV-based experiments.

- Analog 1 ⇒ Outputs MWs: When the analog channel is nonzero, the AWG outputs the MWs which are then amplified by a 25 W amplifier (**Minicircuits: ZHL-25W-63+**) and delivered to the MW loop (Figure 4.1(**b**)).
- Channel 1, Marker 1 ⇒ Triggers the DAQ acquisition (**National Instruments: NI-USB 6281**): The DAQ (Data AcQuisition tool) records the electrical signals measured by the photodiode and converts into digital signals for later analysis. The acquisition pulse is a short (usually 300 ns) pulse that informs the DAQ to acquire data for the length of that

pulse. A value of 2^6 represents the ON state when programming Marker 1.

- Channel 1, Marker 2 ⇒ Triggers the DAQ start: The start trigger is a short (100's ns) pulse at the beginning of any pulse sequence that prepares the DAQ for acquisition pulses. A value of 2^7 represents the ON state when programming Marker 2.

- Channel 2, Marker 1 ⇒ Triggers the AOM: When ON, the AWG triggers a MW switch (**Minicircuits: ZASWA-2-50DRA+**) which outputs a 250 MHz signal generated by an SRS (**Stanford Research Systems: SG386**). The signal is then amplified (**Minicircuits: ZHL-03-5WF**) and delivered to the AOM. When exposed to this signal, the AOM diffracts the first-order diffraction into the experimental path (Figure 4.1(**a**)).

4.1.2.2 Inductive NMR

The following summarizes the AWG controls and electronic components for the inductive NMR experiments.

- Analog 2 ⇒ Outputs nuclear RF: When the analog channel is nonzero, the AWG outputs the RF signal which propagates through two attenuators (**Minicircuits: CAT-3 and CAT-10**) and is amplified by a 2W amplifier (**ZHL-1-2W-S+**). The signal then passes to a MW switch which acts as a T/R (Transmit/Receive) device. When the switch's TTL (Transistor-Transistor Logic) is zero, the switch transmits the signal to a tuned and matched RF coil (Figure 4.1(**b**)). Conversely, when the switch's TTL is nonzero, the switch receives the NMR signal measured inductively by the same RF coil. When the signal is received, it propagates through a pre-amplifier (**Miteq: 933274**) and is delivered to a mixer

(**Minicircuits: ZP-3+**) which downmixes the signal to a few kHz[4]. The mixer has two inputs (L = Local oscillator and R = Received signal) and one output (X = $|\mathrm{L} - \mathrm{R}|$). L is connected to Channel 1 of a signal generator (**Rigol: DG1032**), and it is set to a frequency several kHz from the received signal. R is the inductively measured signal. Once downmixed, the signal passes through a low pass filter (**Minicircuits: SLP-1.9+**) and is delivered to the DAQ.

- Channel 2, Marker 2 $\Rightarrow$ Triggers the Rigol (**Rigol: DG1032**). As described above, Channel 1 on the Rigol outputs a signal to the mixer's L input, and Channel 2 is used as the TTL pulse that controls the switch's T/R functionality. When the AWG marker is nonzero, the Rigol outputs its Channel 1 and Channel 2 data.

If necessary, the shim coils, represented as the yellow wrapped coils between the magnet poles in Figure 4.2, can be driven to minimize magnetic field inhomogeneities, thus minimizing line broadening from these inhomogeneities[5].

4.2 Measuring Sensitivity of NV-Based Measurements

Given the experimental layout, the sensitivity of the NV centers to NMR, or NMR-like, signals was calculated. First, CW-ODMR and Rabi measurements were performed to determine the NV resonance frequency and the π pulse duration. Next, a conversion factor between magnetic field and applied voltage was obtained by measuring the amplitude of a known oscillating magnetic field using a sequence called AC magnetometry. Using the conversion factor, the signal

---

[4] This downmixing is crucial because the DAQ has an internal filter which significantly reduces measured signal amplitude as a function of increasing frequency.

[5] In the inductive NMR experiment, the shim coils were driven with $\approx 100 - 300$ mV to correct for inhomogeneities. However, these field corrections minimally decreased line broadening.

SNR was determined using a CASR sequence, and finally, the sensitivity was calculated.

4.2.1 CW-ODMR

The following is the CW-ODMR data that was used to determine the NV resonance frequency for the $\mathrm{m_s} = 0 \leftrightarrow \mathrm{m_s} = +1$ transition at an applied magnetic field of approximately 2030 G. The resonance frequency for the $\mathrm{m_I} = +1/2$ state was 2.8104 GHz, while the $\mathrm{m_I} = -1/2$ resonance frequency was 2.8075 GHz. However, the frequency that was used in all following sequenes was 2.8091 GHz as it is the frequency between the two hyperfines[6].

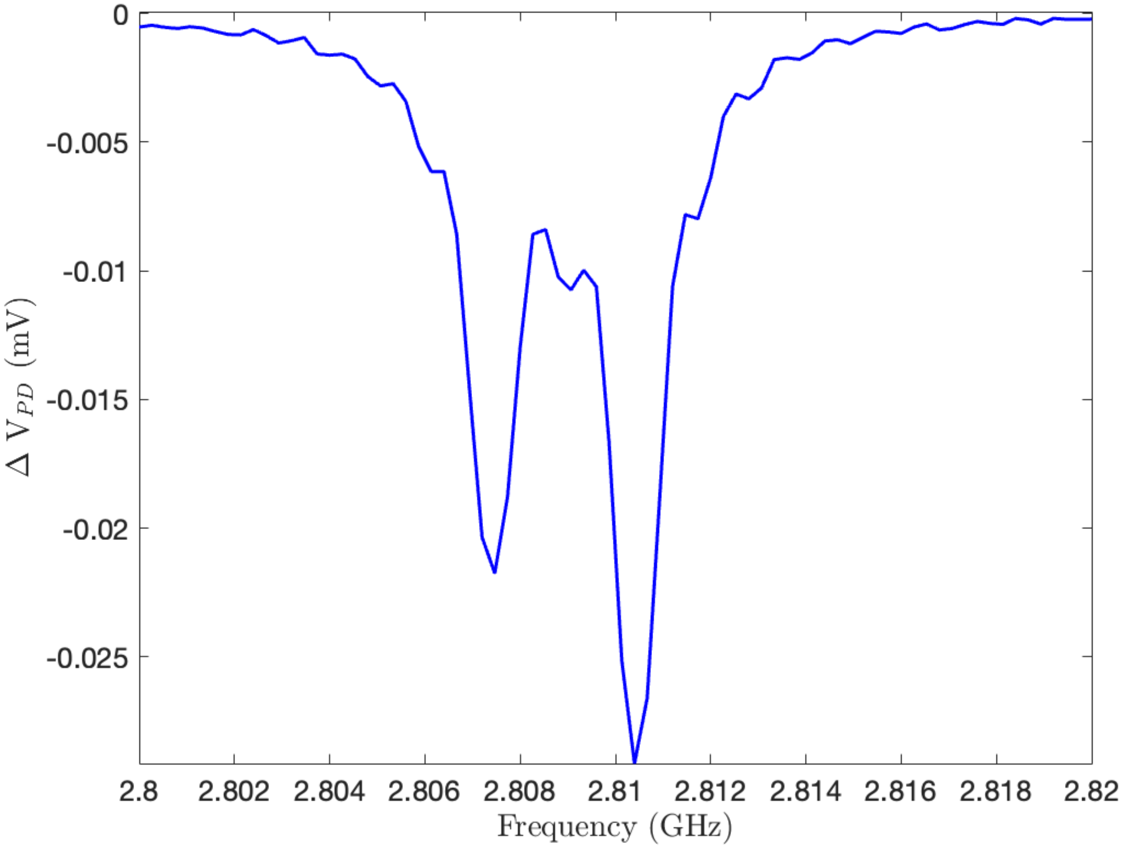

Figure 4.3: Depicts the measured CW-ODMR data for an applied magnetic field of approximately 2030 G. The resonance frequency used for all following sequences was 2.8091 GHz.

---

[6] For ^{15}N diamonds, typically the frequency between the two hyperfines is used because both hyperfines are then equally detuned from the driving frequency.

4.2.2 Rabi

The following is the Rabi data that was used to calibrate the π pulse duration which was 56 ns.

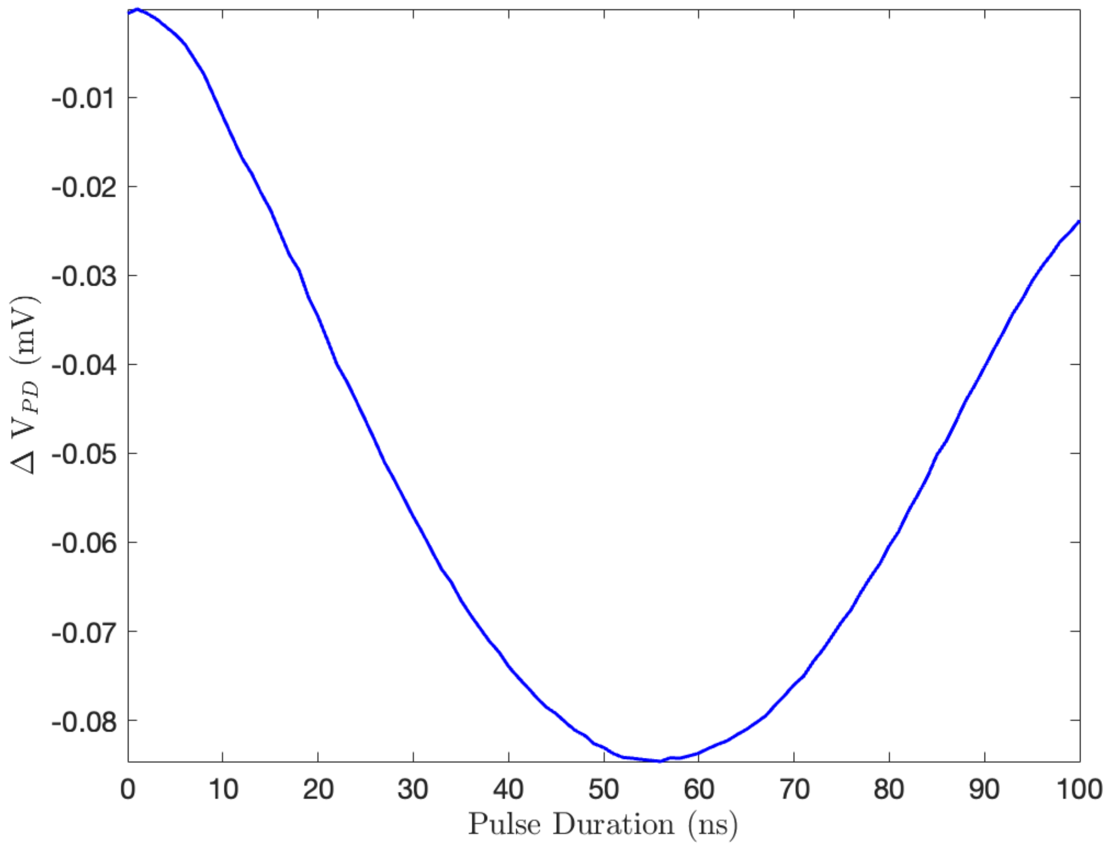

Figure 4.4: Depicts the measured Rabi data. The π pulse duration used for all following sequences was 56 ns.

4.2.3 AC Magnetometry

To obtain the conversion ratio, a signal with known frequency and variable amplitude is applied to the RF coil (Figure 4.1(**b**)). This action produces an oscillating magnetic field $B(t)$:

$$B(t) = B_{\text{AC}} \sin(2\pi f_{\text{coil}} + \phi), \tag{4.1}$$

where $B(t)$ is the oscillating field, B_{AC} is the unknown field amplitude, f_{coil} is the frequency which the coil is driven, and ϕ is a random, but fixed phase with respect to the applied magnetometry sequence.

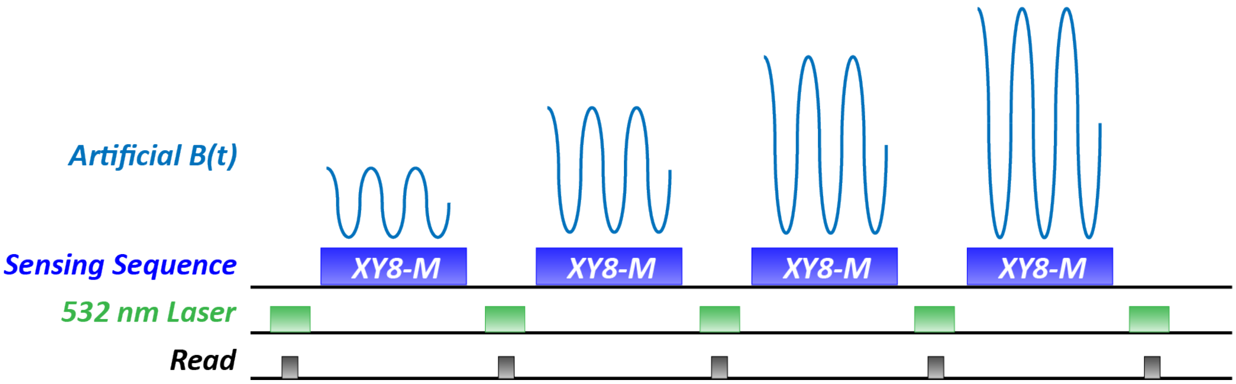

Figure 4.5: Depicts the AC Magnetometry sequence which is a repeated series of XY8-M sequences during which a $B(t)$ of varying amplitude is present.

While $B(t)$ is present, the NVs undergo an XY8-M magnetometry sequence (see Figure 4.5). During the sequence, the NVs accumulate phase with a rate dependent on the amplitude of $B(t)$, thus the measured photodiode voltage oscillates with $B(t)$. Fortunately, when the NVs accumulate $\pi/2$ phase, the measured photodiode voltage reaches a minimum (or maximum) and the field amplitude B_{AC} can be calculated with the following equation:

$$\frac{B_{\text{AC},\,\pi/2}}{V_c} = \frac{\hbar\pi^2 f_{\text{coil}}}{2g\mu_B M} \times \frac{1}{V_c}, \tag{4.2}$$

where $B_{\text{AC},\,\pi/2}$ is the field amplitude calibrated by the NV $\pi/2$ phase accumulation and V_c

is the voltage that sets the output of the current supply to the RF coil. Hence, by sweeping the voltage of the RF coil, the conversion ratio can be obtained and the $B(t)$ amplitude can be found given a certain RF coil voltage (or vice versa) [12].

4.2.4 CASR

To measure the SNR of a CASR spectrum, a $B(t)$ of known amplitude, where the amplitude is calibrated with the conversion ratio, is applied to the NV system (Equation 4.1). This signal is then sensed by the CASR sequence, and the noise is calculated by taking the average of the most quiet region near the signal peak[7].

4.2.5 Sensitivity

Finally, the sensitivity, η_{AC}, can be calculated with the following equation:

$$\eta_{\text{AC}} = \frac{B_{\text{AC}}}{\sqrt{T}} \times \frac{1}{\text{SNR}}, \tag{4.3}$$

where B_{AC} is the applied field of known amplitude and T is the CASR measurement duration.

4.2.6 Example Calculation

The following serves as an example sensitivity calculation. For this example, $f_{\text{coil}} = 1$ MHz and the magnetometry sequence is XY8-8.

---

[7] Although not necessary for calculating SNR as its units cancel, it is typically convention to convert the data from units of voltage to units of Tesla using the conversion ratio. In doing so, the peaks and noise, which are magnetic in origin, can be easily read in magnetic units.

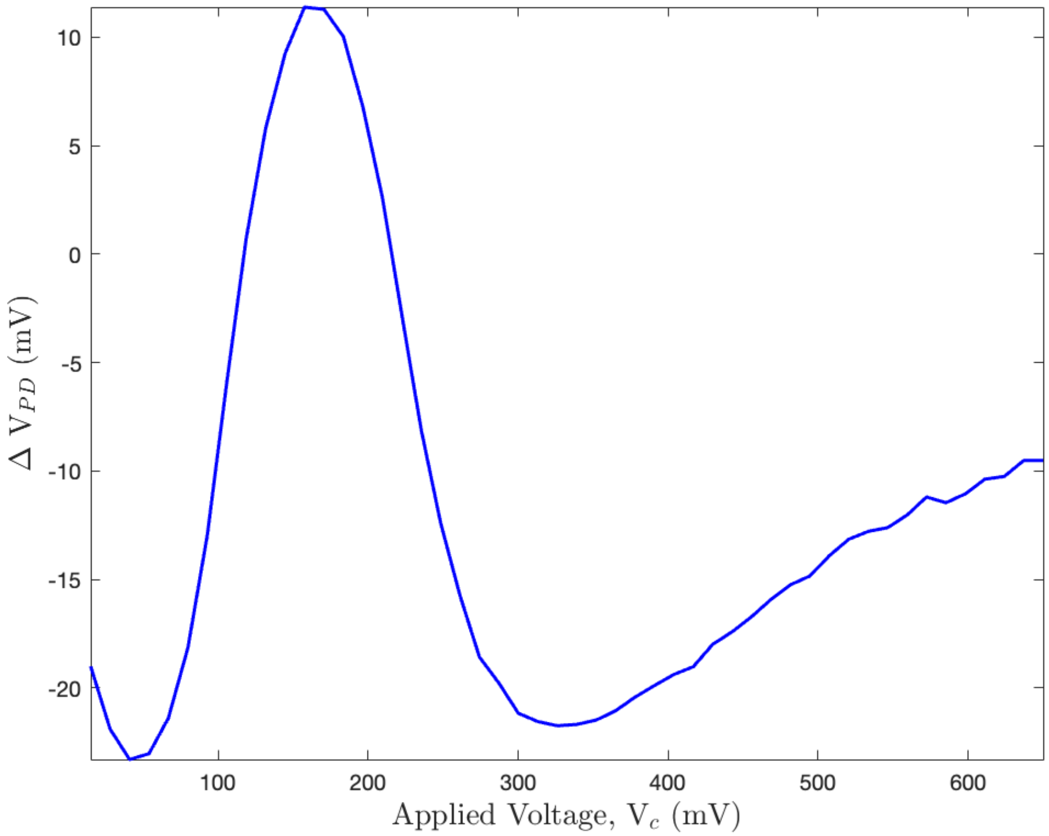

Figure 4.6: Depicts the measured AC Magnetometry data for a $f_{\text{coil}} = 1$ MHz and an XY8-8 sequence. Since there are multiple extrema, the V_c corresponding to an NV accumulation of $\pi/2$ is the average difference of the extrema. For this data, V_c equals 58.47 mV.

As depicted in Figure 4.6, the measured photodiode voltage oscillates with $B(t)$[8]. Because there are multiple extrema, the V_c that should be used in the conversion ratio is the average difference:

$$V_c = \frac{157.52\text{mV} - 40.58\text{mV}}{2} = 58.47\text{mV}$$

Substituting this value into Equation 4.2 yields:

---

[8] The mechanism behind the signal decay is unknown.

$$\frac{B_{\text{AC, }\pi/2}}{V_c} = \frac{\hbar\pi^2}{\mu_B} \times \frac{1\text{MHz}}{2 \times 2} \times \frac{1}{58.47\text{mV}} = 7.6\text{nT/mV}.$$

With this conversion, it can be determined that a $B(t)$ with amplitude 20 nT requires a voltage of 2.66 mV. A CASR sequence is then performed for a duration of $T = 1$s, and this entire sequence is repeated multiple times to increase SNR. To calculate the SNR given that the sequence was repeated, first the data in units of photodiode voltage was converted to Tesla using the conversion ratio, and then the absolute value of the FFT'ed data of each CASR sequence was obtained. For each CASR sequence, the noise was calculated by taking the average of the data in a small, quiet region near the signal. Finally, the noise values for each CASR sequence were averaged to give the final noise value.

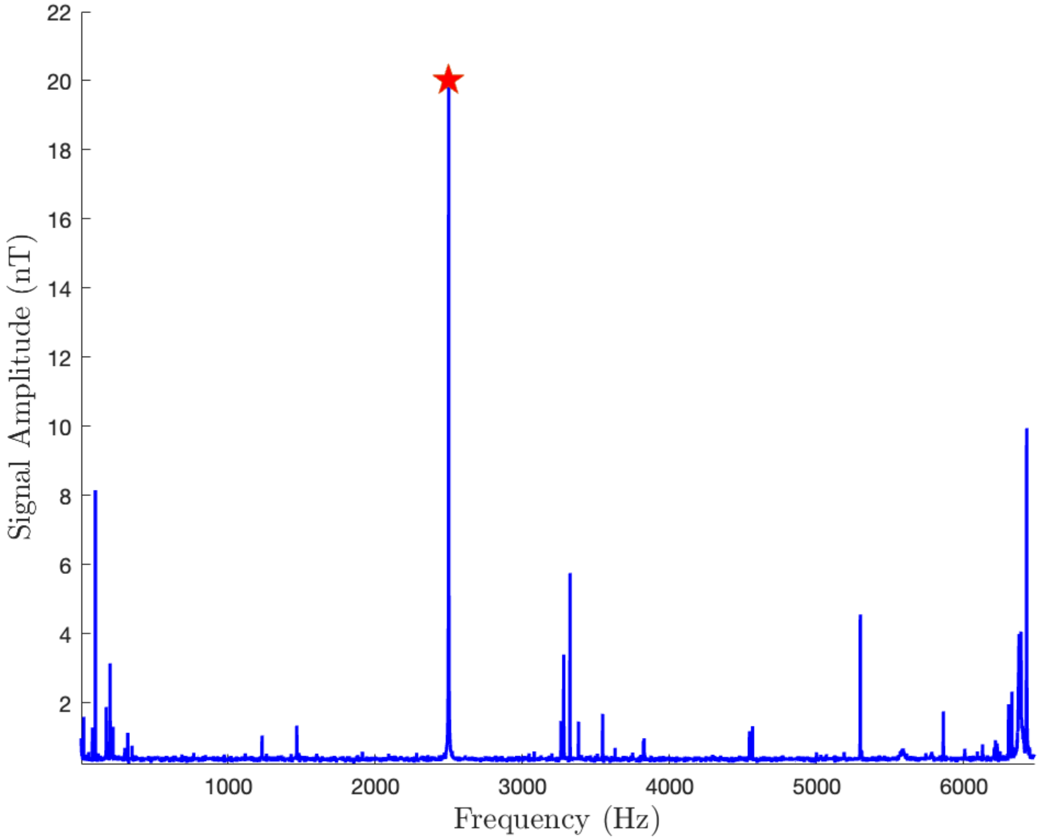

Figure 4.7: Depicts the CASR data for a $f_{\text{coil}} = 1$ MHz, an XY8-8 sequence, and 25 averages. To obtain the data plotted here, first the data is converted to units of Tesla using the conversion ratio, and then the absolute value of the FFT'ed data for each of the 25 CASR repetitions is obtained. The resulting 25 repetitions are then averaged and the data is plotted here. The red star marks the frequency and amplitude of the measured signal, $\delta f = f_{\text{coil}} - f_0$.

For the system described here, the sensitivity to a 1 MHz, 20 nT signal is approximately $392\text{pT}/\sqrt{\text{Hz}}$. This means for a 1 second measurement, the smallest signal amplitude that can be measured is 392 pT.

4.2.7 Sensitivity vs. Frequency

To best characterize the NV-NMR experiment, the sensitivity was measured for a host of coil frequencies. Figure 4.8 summarizes the AC magnetometry curves and Figure 4.9 summarizes the CASR spectrum for each coil frequency.

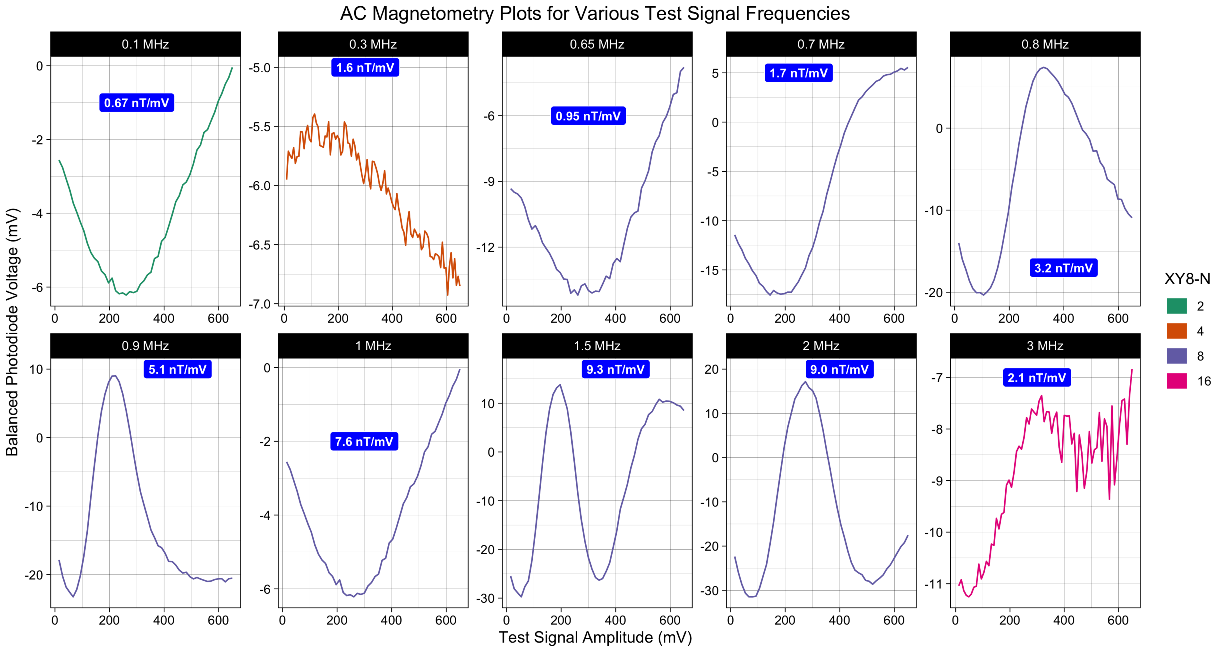

Figure 4.8: Depicts the AC magnetomery curve for each coil frequency. The data color corresponds to the XY8-M sequence and the blue label inside each plot details the conversion ratio.

In Figure 4.8, the f_{coil} of 0.3 MHz and 3 MHz are particularly noisy. Additionally, there is little consistency to the magnetometry curve, including the decay rate and shape.

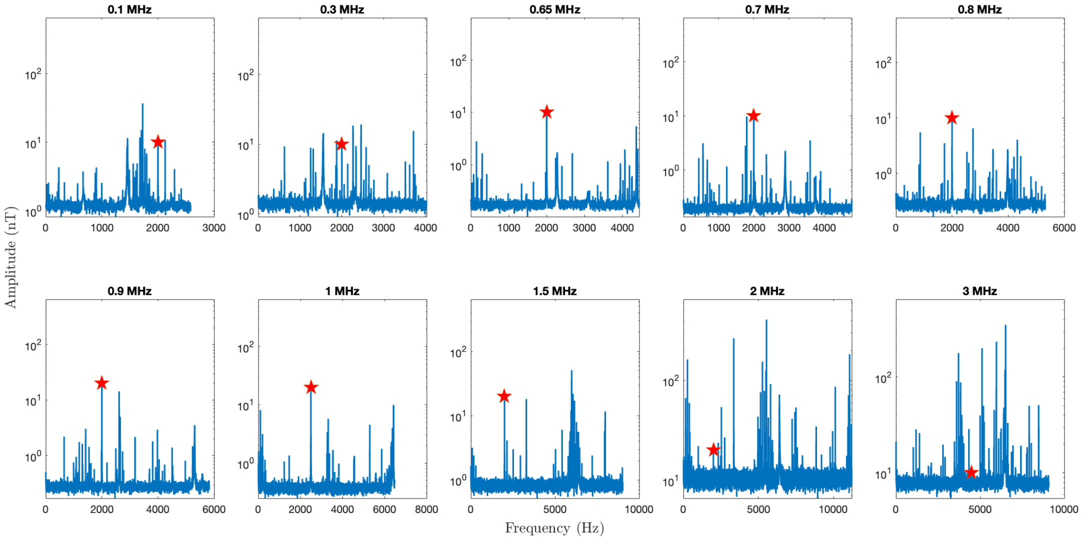

Figure 4.9: Depicts the average of the absolute value of the FFT'ed CASR data. For each coil frequency, except for 3 MHz, the CASR sequence was repeated 25 times; the 3 MHz data was repeated 50 times. The red star marks the measured signal frequency and amplitude.

The spectra in Figure 4.9 demonstrate that the measured CASR data is rather consumed by spurious noise peaks that are not correlated to the measured signal (i.e. not signal harmonics).

Based on the data in Figures 4.8 and 4.9, the sensitivity for each coil frequency was calculated. The results are plotted in Figure 4.10 and the experimental conditions are summarized in Table 4.1.

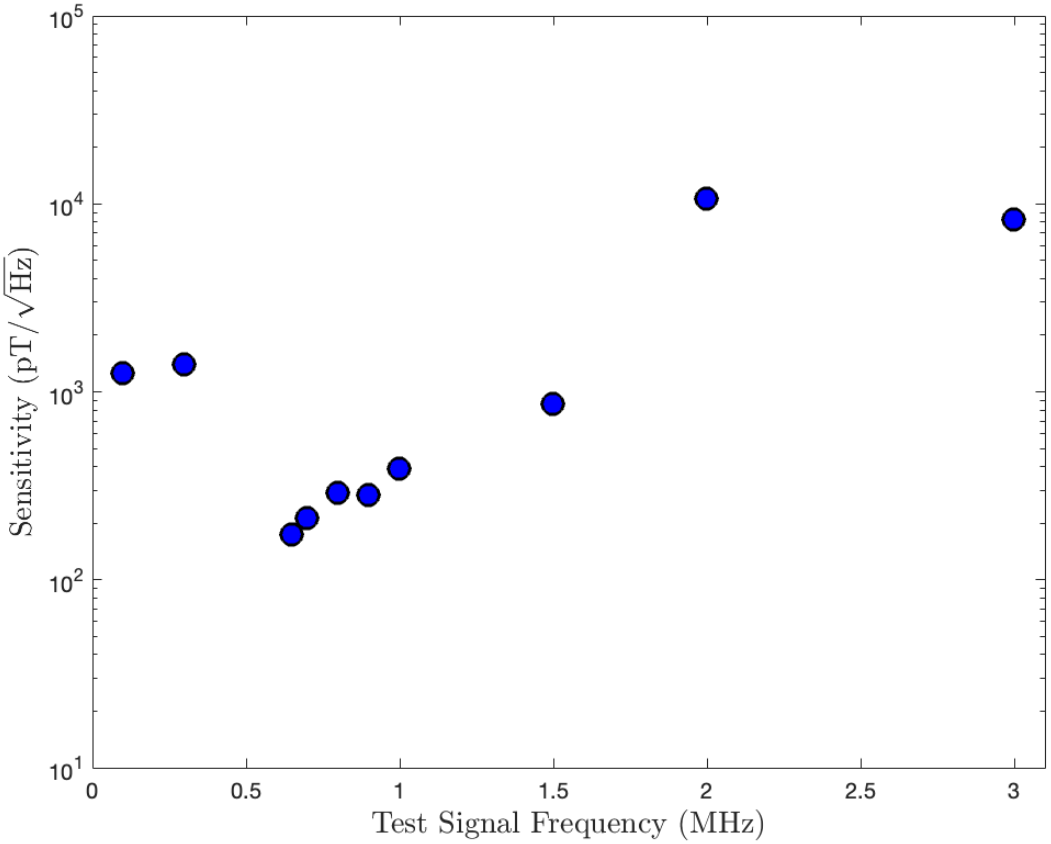

Figure 4.10: Semi-log plot of the calculated sensitivity, η_{AC}, for each coil frequency. The best sensitivity was $\eta_{\text{AC}} = 173\text{pT}/\sqrt{\text{Hz}}$ for a f_{coil} of 0.65 MHz.

As can be observed, the system is most sensitive to a coil frequency of 0.65 MHz, but it is largely insensitive to coil frequencies 0.1 - 0.3 MHz and 2 - 3 MHz.

4.2.8 Discussion

Unfortunately, the best measured sensitivity at 0.65 MHz is an order of magnitude larger than the reported sensitivity in [10] [9] and [8] (see Table **??**). The exact mechanism behind these insensitivities is currently unknown, however the potential contributions to this insensitivity are discussed below.

1. As described previously, the CASR data (Figure 4.9) contains quite large, uncorrelated noise peaks (i.e. not signal harmonics). The presence of this additional and large noise may be increasing the noise floor, thus decreasing the SNR and subsequently, decreasing the sensitivity.

2. The noise floor before and after conversion differs by more than an order of magnitude which becomes apparent when comparing Figure 4.11, which overlays the unconverted (i.e. units of mV) CASR data for all frequencies, to Figure 4.12, which overlays the converted noise (i.e. units of nT) for a small quiet, region near the measured signal. Figure 4.11 demonstrates that the noise floors for the various coil frequencies differ by less than an order of magnitude. However, once converted (Figure 4.12) the noise floors vary by more than an order of magnitude. As of now, there are two explanations for this behavior.

    (a) The 2 W RF amplifier used in this experiment, ZHL-1-2W-S+, is designed for 5 - 500 MHz input frequencies[9]. It is possible that operating outside the amplifier's frequency specifications produced arbitrary noise floors depending on the input frequency (Figure 4.11) and that these arbitrary noise floors were amplified following conversion (Figure 4.12).

    (b) The AC magnetometry sequence may also not be operating correctly since the noise floors only differ by a value greater than an order of magnitude after the data is converted. If the AC magnetometry step has properly calibrated the conversion ratio, it would be predicted that converting the data would not significantly skew the noise floor. Thus, the sensitivity may actually be larger than that reported in Table 4.1

---

[9] Even though these specifications do not match the RF coil frequencies, this amplifier was the only one available at the time.

assuming the AC magnetometry sequence artificially skews the noise floor.

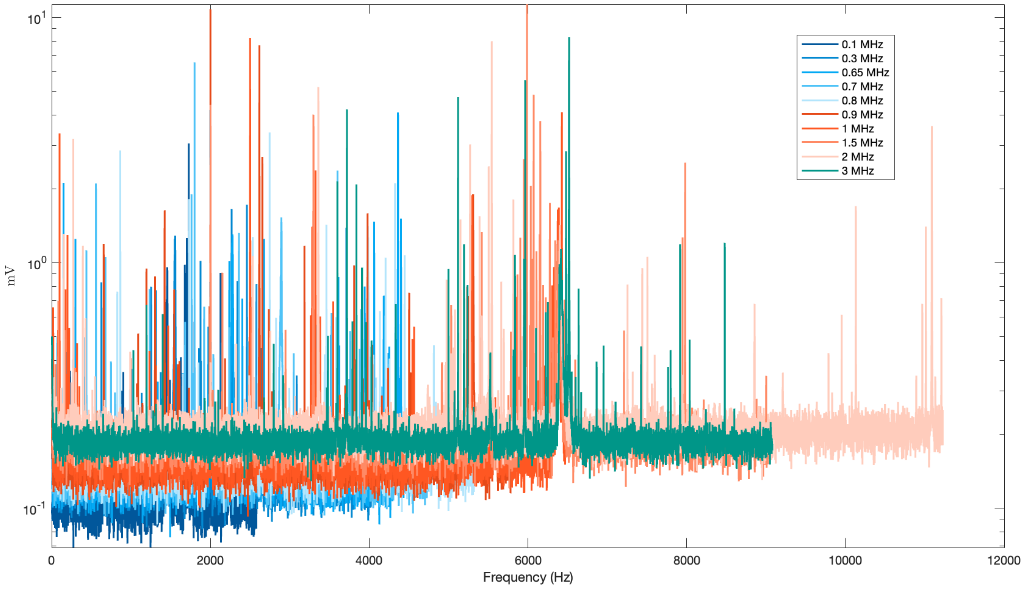

Figure 4.11: Depicts the unconverted CASR data for all coil frequencies. It can be observed that the noise floor changes with the coil frequency, but that they differ by less than an order of magnitude.

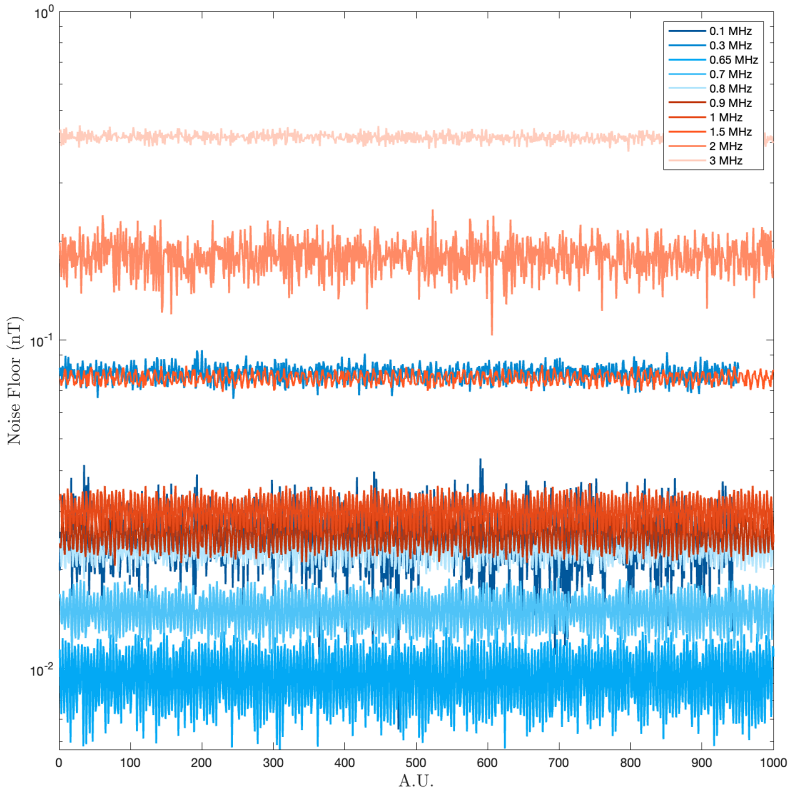

Figure 4.12: Depicts the converted CASR data noise floor for all coil frequencies, where the noise floor is the average of the absolute value of the FFT'ed CASR data for a small, quiet region near the measured signal. Again, it can be observed that the noise floor changes with the coil frequency, but now, they differ by more than an order of magnitude.

3. Even without the conversion issues, the unconverted data in Figure 4.11 is roughly an order of magnitude larger than the measured noise floor of the photodiode (see Figure 4.13); the photodiode noise was measured with a CASR sequence while all electronics (i.e. amplifiers, power supplies, AWG, DAQ etc.), electromagnet, and laser were on. It is currently unclear what source is producing this additional order of magnitude noise during the measurement.

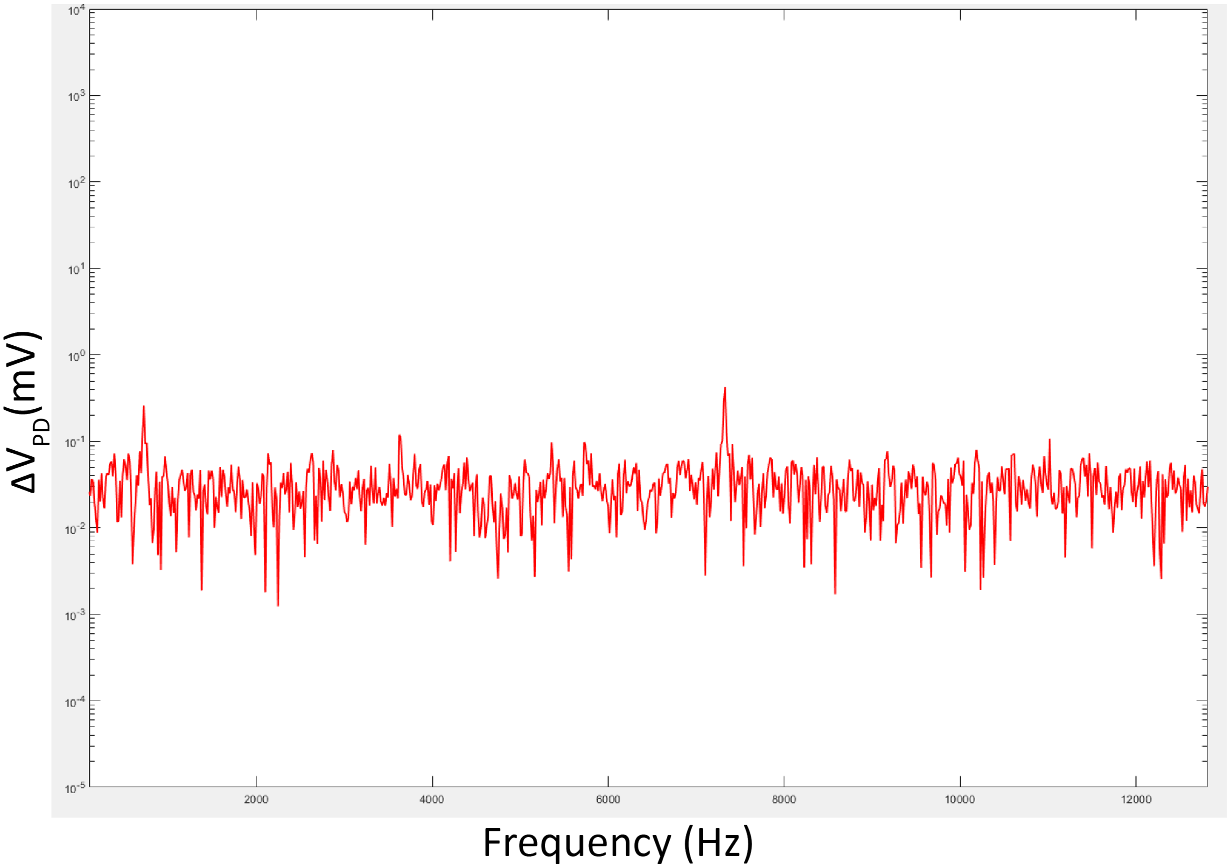

Figure 4.13: Depicts the photodiode noise (in mV) which was measured with a CASR sequence while the electronics, electromagnet, and laser were on. On average, the photodiode noise is an order of magnitude smaller than the unconverted CASR data for the coil frequencies.

4. Additionally, the MW delivery system is limiting the achievable SNR/sensitivity and the range of measurable frequencies. As mentioned many times prior, the dynamical decoupling sequence simultaneously minimizes T_2^* effects and acts as a narrowband filter that limits the signals the NVs can sense. The MW loop that was used for these experiments has a weak Rabi such that the π pulses themselves are long (Figure 4.4). In terms of the long π pulse's effect on T_2^*, fewer π pulses can be applied before the dynamical decoupling sequence approaches the time scale of T_2. This means there are less refocusing pulses in the sequence, and the sequence was less effective at squashing T_2^* effects. The NVs then

had less time for coherent measurements, which means either (1) more measurements must be made to achieve a good SNR or (2) the magnetometry sequence has a duration that actually exceeds T_2. For this diamond, a $T_2 \simeq 92\mu$s was extracted from an exponential fit of the measured photodiode voltage of Rabi, XY8-12, XY8-20, XY8-30, and XY8-40 data (Figure 4.14). However, this is an estimate T_2 that is only applicable for XY8-12 - XY8-40 sequences, and it is expected to be smaller for XY8 sequences with $M < 12$: for instance, as described in Appendix A.2, this diamond has a spin echo derived T_2 of 14.5μs. Detailed in Figure 4.1, an XY8-2 sequence, of duration 81.6μs, was used to measure $f_{\text{coil}} = 0.1$ MHz. Unfortunately, for this XY8-M, T_2 is most likely roughly equal to the sequence duration. Therefore, it is possible that some of the insensitivity to the 0.1 MHz signal arises because the magnetometry sequence is longer than the coherence time. Additionally, the long π pulse duration guarantees that only a certain range of frequencies can be measured because as the coil frequency increases, the spacing between the π pulses decreases. Eventually, the π pulses will overlap because the τ necessary to measure that signal becomes shorter than the π duration. This problem can be resolved by designing a MW system that delivers high frequency and high power MWs (see Chapter 5).

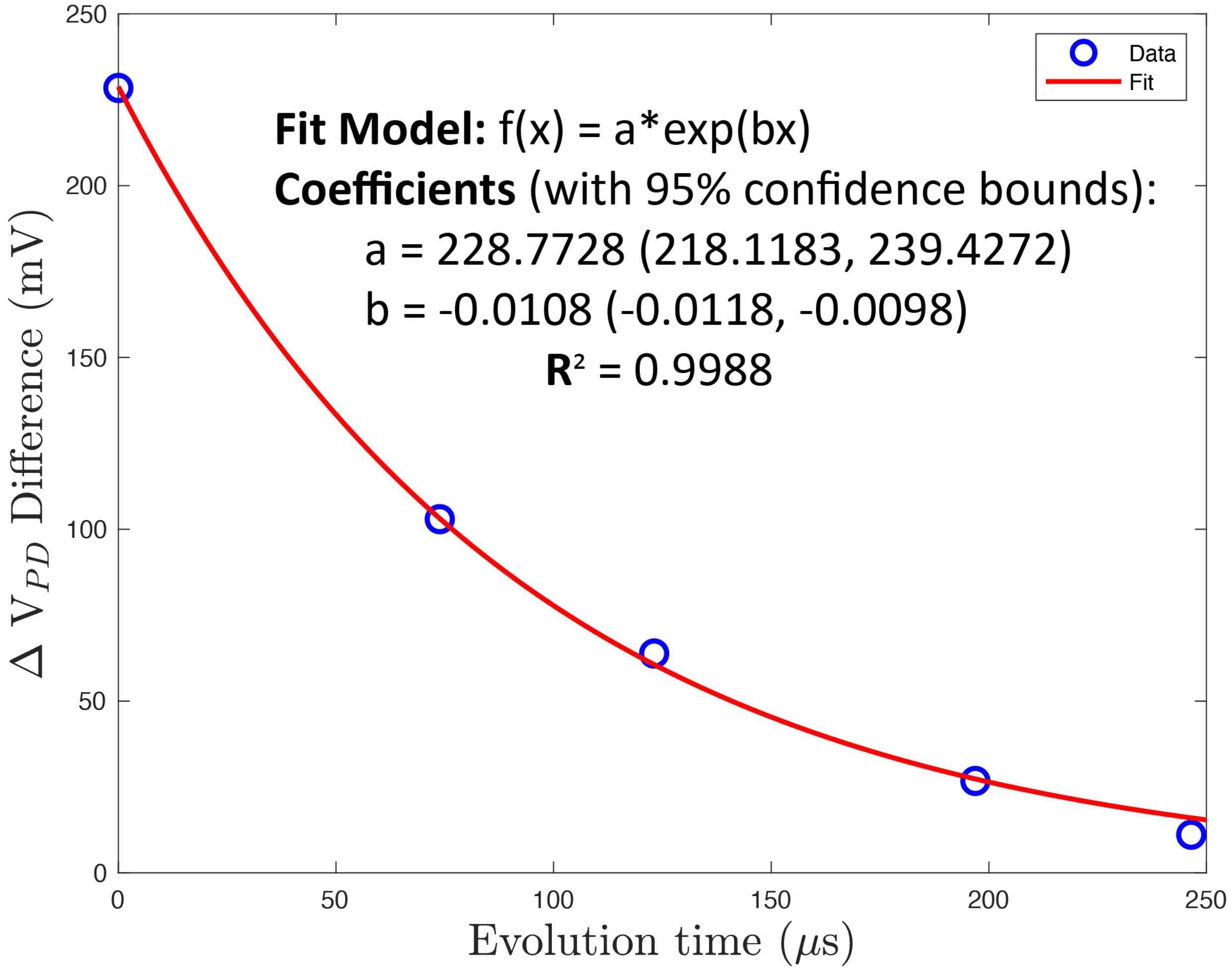

Figure 4.14: Depicts the measured Rabi and XY8-M data, as well as the exponential fit used to extract T_2. The coil frequency was 1.3 MHz. The evolution time was calculated as: $1/f_{\text{coil}} \times 8 \times M$, where 8 arises from XY8. For the Rabi data, the evolution time was assumed to be 0. The ΔV_{PD} difference for each Rabi/XY8-M data is calculated as the difference between the maximum and minimum measured photodiode voltage. The data was fit to a decaying exponential and the coefficients with 95% confidence bounds are reported. T_2 was assumed to be equal to $1/|b|$.

5. The sample holder, which includes the cuvette, diamond system, and MW loop, is a rather unstable contraption (Figure 4.15); it is annoyingly easy to accidentally nudge the system such that the diamond becomes misaligned with the magnetic field or such that the MW loop slips off the diamond surface. Additionally, the MW loop slowly drifts away from the diamond surface which decreases the achievable Rabi strength. To ensure the diamond and MW loop are properly oriented, it is often necessary to remove the sample holder and

re-install. Unfortunately, this process of removing and re-installing can consume a day or two. Similar to the item above, a possible solution is to design a sample holder that eliminates the bulkiness of the cuvette and a MW system that can be glued to the diamond (see Chapter 5).

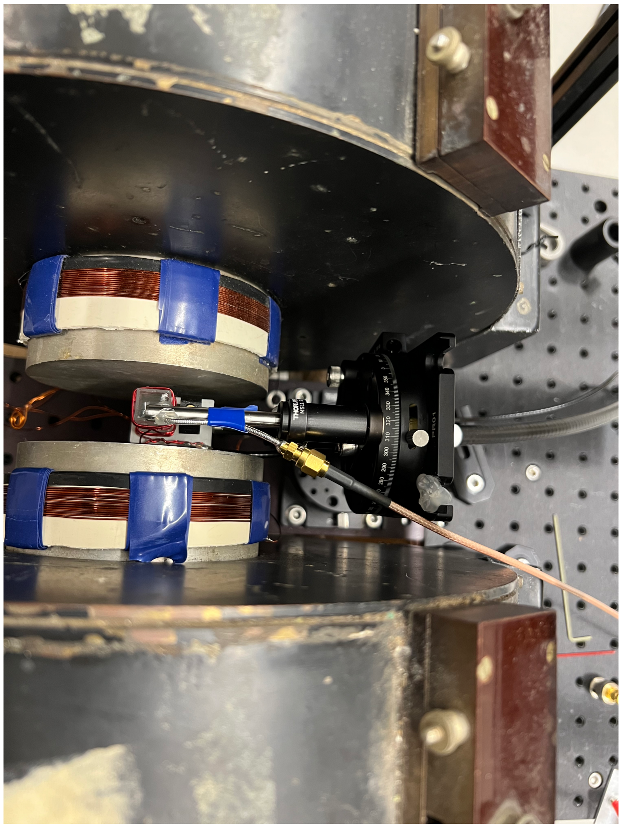

Figure 4.15: Depicts the sample holder, which includes the cuvette, diamond system, and MW loop.

4.3 Inductive NMR Measurements

In addition to NV sensitivity to NMR/NMR-like signals, it was necessary to determine the Rabi frequency of the nuclear spins. Described previously (Section 3.2), the AERIS protocol is one of the most promising sequences as it would increase the operable magnetic field without equally increasing the MW engineering challenges [16]; the pulse sequence is able to accomplish this feat because the nuclear $B(t)$ oscillates at frequency, Ω, which is the Rabi frequency of the nuclear spins under the influence of an applied B_1. To obtain this Rabi frequency for the given experimental conditions, an inductive NMR sequence (Figure 4.16) was performed.

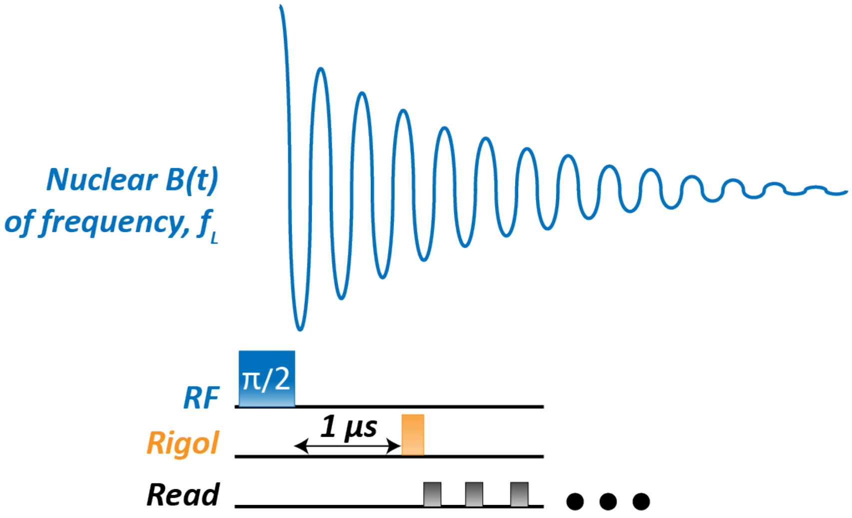

Figure 4.16: Depicts the inductive NMR sequence applied to the sample nuclear spins. A $\pi/2$ RF pulse rotates the magnetization into the transverse plane and the nuclear drive coil is allowed to ring down for a duration of 1μs to minimize measurement of unwanted noise. Channel 2 on the Rigol is then turned on which triggers the MW switch to switch from transmit to receive mode, and the nuclear drive coil then acts as a receiver coil to measure the nuclear $B(t)$. The nuclear $B(t)$ continues to be read out until the signal decays.

The magnetic field was set to 239.6 mT which corresponds to a measured 10.2 MHz Larmor frequency. To properly downmix this signal, the Rigol's Channel 1 is set to 10.5 MHz with a 500 mA amplitude. The downmixed signal is then 300 kHz. To trigger the T/R functionality of the MW switch, the Rigol's Channel 2 is set to a square wave with a period of 50 ms, a high voltage of 5 V (triggers receive functionality), a low voltage of 0 V (triggers transmit functionality), a pulse width of 49.999964 ms, and a phase of 359.999°[10]. The liquid sample was a copper sulfate and DI (De-Ionized) water solution. At a ratio of 1.25 mg copper sulfate per 1 mL DI water, the

---

[10] Ideally, an actual T/R switch would be used to eliminate such bizarre settings on the Rigol.

solution had a T_1 of approximately 100 ms[11]. This T_1 is convenient because the nuclear spins cannot be re-initialized with another $\pi/2$ pulse until they relax back into thermal equilibrium, and the shortened T_1 minimizes the time delay between re-initialization. Finally, to reduce line broadening from magnetic field inhomogeneities, the shim coils were driven with a current of approximately 300 mA.

With these experimental conditions and an RF $\pi/2$ pulse duration of 100μs, a proton signal for the copper sulfate and DI water solution was measured with a FWHM linewidth of approximately 1.7 kHz.

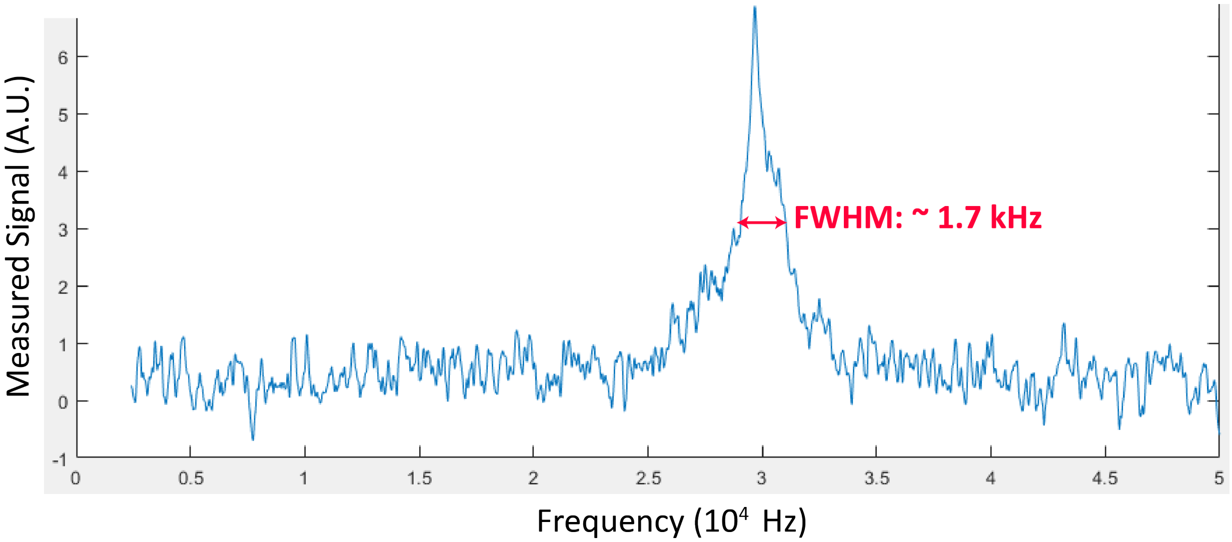

Figure 4.17: Depicts the proton signal for a copper sulfate and DI water solution with a FWHM linewidth of approximately 1.7 kHz. The RF $\pi/2$ pulse duration was 100μs.

Having confirmed the experimental apparatus can inductively measure NMR signals, the nuclear spins' Rabi frequency was measured by varying the duration of the RF pulse (Figure 4.18)[12].

---

[11] On its own, DI water has a T_1 of several seconds.

[12] There are two methods to measure B_1's Rabi frequency: (1) Hold the nuclear RF pulse duration constant and vary its amplitude, or (2) Hold the nuclear RF pulse amplitude constant and vary its duration. Ideally, Method (1)

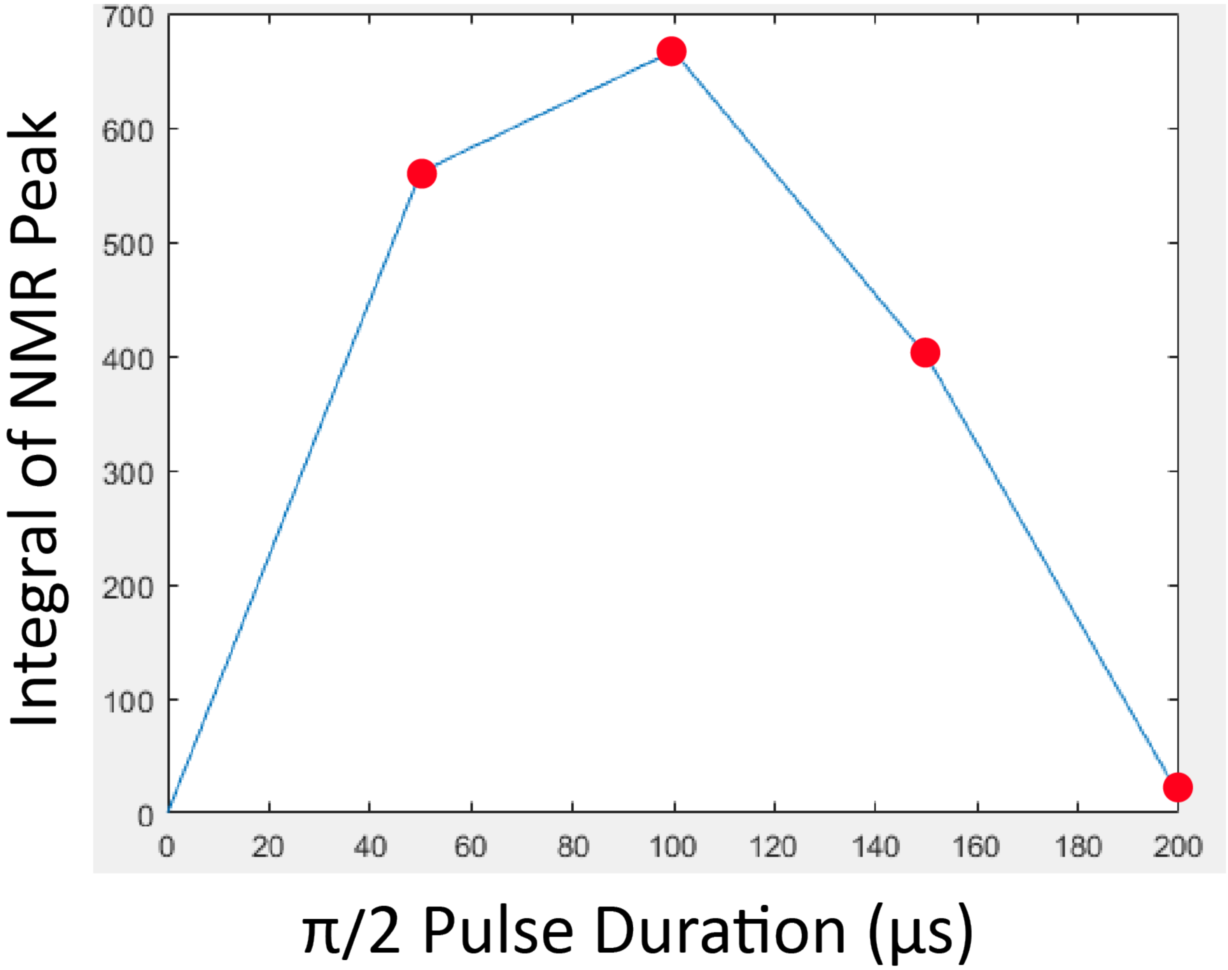

Figure 4.18: Depicts the measured B_1 Rabi. It is assumed that a pulse duration of approximately 100μs corresponds to a $\pi/2$ flip of the nuclear spins (i.e. longitudinal to transverse magnetization rotation).

Figure 4.18 plots the B_1's Rabi curve with the maximum amplitude at approximately 100 μs corresponding to a $\pi/2$ flip (i.e. fip from longitudinal to transverse magnetization). From this data, the magnitude of B_1 can be calculated with the following equation:

---

is more useful because Method (2) is eventually limited by linewidth. The RF pulse duration sets the frequencies the measurement is sensitive to (i.e. the measurement linewidth), and as the pulse duration decreases, so does the measurement linewidth. Eventually, the signal's linewidth is broader than the measurement linewidth, thus the proton signal is no longer observable. Unfortunately, the 2W amplifier that was available was not powerful enough for Method (1).

$$B_1 = \frac{\alpha}{2\pi\gamma_I t_p}, \tag{4.4}$$

where α is the flip-angle (radians) and t_p is the pulse duration (μs). With $t_p = 100\mu$s corresponding to $\alpha = \pi/2$, then $B_1 = 58.7\mu$T and the Rabi frequency is 2.5 kHz for an applied RF voltage of 9.6 Vpp, or 0.23 W.

Relating these measured values to the AERIS protocol, the NV system would need to sense a 2.5 kHz signal. Based on the sensitivities in Table 4.1, the NVs would be largely insensitive to this signal. Now, the Rabi could be increased by increasing the applied power such that a 100 kHz Rabi could be produced with 400 W. However, this is a lot of power that would require new high-power electronics. Additionally, the NVs are also largely insensitive to 100 kHz signals. Therefore, along with resolving the insensitivity issues associated with the NVs, it will also be necessary to increase B_1 so as to reduce the power necessary to yield a strong nuclear Rabi.

Table 4.1: Summarizes the experimental conditions, including coil frequency, $B_{\text{AC},\,\pi/2}$, V_c, conversion ratio, applied $B(t)$ amplitude, sequence duration of a single XY8-M sequence, the number of times XY8 is repeated (or M), and the calculated sensitivity. The lime colored row highlights the best calculated sensitivity.

[redacted]	$B_{\text{AC},\,\pi/2}$ **(nT)**	V_c **(mV)**	**Ratio (nT/mV)**	**Sig. Amp. (nT)**	**Seq. DT (μs)**	**XY8-M**	**Sens. (pT/$\sqrt{\text{Hz}}$)**
0.1	175	261	0.67	10	81.6	2	1,255
0.3	263	164	1.6	10	53.7	4	1,408
0.65	285	300	0.95	10	49.4	8	173
0.7	307	183	1.7	10	45.8	8	212
0.8	351	110	3.2	10	40.1	8	290
0.9	395	78	5.1	20	35.6	8	283
1	438	58	7.6	20	32.1	8	392
1.5	658	71	9.3	20	21.4	8	863
2	877	97	9.0	20	16	8	10,600
3	658	308	2.1	10	21.4	16	8,200

Chapter 5: MW Delivery

As described in the previous chapter, one of the issues with the current experimental setup is the MW delivery system which is unstable and limits the achievable SNR/sensitivity and measurable frequencies. The ideal re-designed MW delivery system would have the following qualities:

- a MW carrier frequency ranging from 14 GHz to 90 GHz, which would enable operation at 0.5 T to 3 T, respectively
- a MW Rabi frequency ranging from 25 MHz to 200 MHz which would yield a π pulse duration of 40 ns to 5 ns, respectively
- a B_1 Rabi frequency ranging from 100 to 300 kHz with a maximum applied power of 16 W or 25 W
- homogeneous MW and B_1 across the field of view[1].
- the system can be easily integrated with the liquid sample and diamond
- allows for laser illumination of the diamond and fluorescence can be effectively collected with minimal loss
- operates at room temperature

---

[1] Usually, the field of view is a 30 to 100 μm laser spot diameter for non-imaging applications and a several mm spot for imaging applications.

5.1 MW Resonators

In pursuit of a replacement MW delivery system, a small literature review was conducted on MW resonators and their use in NV and Electron Paramagnetic Resonance (EPR) research. A MW resonator is any electromagnetic device, typically coupled to a waveguide, which concentrates a magnetic field B_{MW} into some small volume when exposed to a resonant frequency [98]. Typically, MW resonators are designed to operate at specific frequency bands with small frequency bandwidths so as to achieve a high loaded quality factor, Q_L [98, 99]. Broadly, Q_L describes the ratio of the MW energy stored in the resonator to the loss per frequency cycle and can be calculated by [99]:

$$Q_L = \frac{f_0}{\Delta f}, \tag{5.1}$$

where f_0 is the center resonance frequency of the resonator and Δf is the frequency bandwidth[2]. Assuming a homogeneous B_{MW} across the sample volume, V_s, the magnitude of B_{MW} is equal to [99]:

$$B_{\text{MW}} = \sqrt{\frac{\mu_0 P Q_L}{\pi f_0 V_r}}, \tag{5.2}$$

where P is the incident MW's power and V_r is the volume of the resonator. Equations 5.1 and 5.2 detail that the smaller the resonator's bandwidth, the larger the B_{MW} magnitude, which is why most MW resonators are designed for specific, small frequency bands. The bands most

---

[2] The loaded quality factor, Q_L encapsulates both the quality factor Q_C which describes the coupling of the resonator to the external environment and the unloaded quality factor, Q_U, which describes the intrinsic response of the resonator [98, 99]

frequently used are the S-band (2 - 4 GHz) and the X-band (8 - 10 GHz). However, there has been some work done for higher frequency bands such as Q-band (35 GHz) and W-band (90 GHz). For NV-NMR systems, the Q- and W-bands are the most useful as they allow operation at 1.5 T and 3 T, respectively. However, minimizing the bandwidth is largely impractical for NV-NMR experiments because these experiments rely on sequences with pulses which have an inherent bandwidth. Thus, NV-NMR systems necessitate a delicate balance between bandwidth, Q_L, and B_{MW} magnitude.

Table 5.1 summarizes the NV experiments that have utilized MW resonators and the EPR experiments with resonator frequencies in the Q- or W-bands. While the NV experiments have demonstrated some great initial success, several resonators are currently only applicable for single NVs and none of the experiments have performed NV-NMR measurements, thus its unclear how simplistic or damaging it might be to integrate a liquid sample[3]. Additionally, the resonators with large Rabi frequencies operate near zero-field which is not the field regime for the aforementioned NV-NMR experimentation (Table 5.1).

The resonators used for EPR experimentation operate at larger carrier frequencies and stronger Rabi frequencies. Although these specifications more closely align with the desired operating NV-NMR conditions, many of these resonators have large Q_L which implies a small bandwidth. As mentioned previously, a small bandwidth is impractical for pulsed NV-NMR experimentation. Additionally, excluding the rectangular TE$_{U02}$ cavity in [100], none of the EPR resonators have optical access for either the excitation laser or fluorescence collection (Table 5.1).

Ultimately, it was determined that MW resonators are a good technology to monitor, but

---

[3] MW resonators can heat the sample if the electric field component of the MW is not contained properly by the resonator [98].

there is still quite a bit of development required before the resonators can be easily integrated into a high-field NV-NMR experiment.

5.2 Coplanar Waveguide

Having eliminated MW resonators as an immediate solution, a coplanar waveguide was suggested as an alternative solution. Compared to EPR resonators, the coplanar waveguide will not operate at such large frequencies, but the bandwidth will be much larger which is necessary for the pulsed experiments and allows some initial flexibility for operable magnetic fields. The CAD model of the waveguide with a 2×2 mm square diamond on top is depicted in Figure 5.1a and **??**.

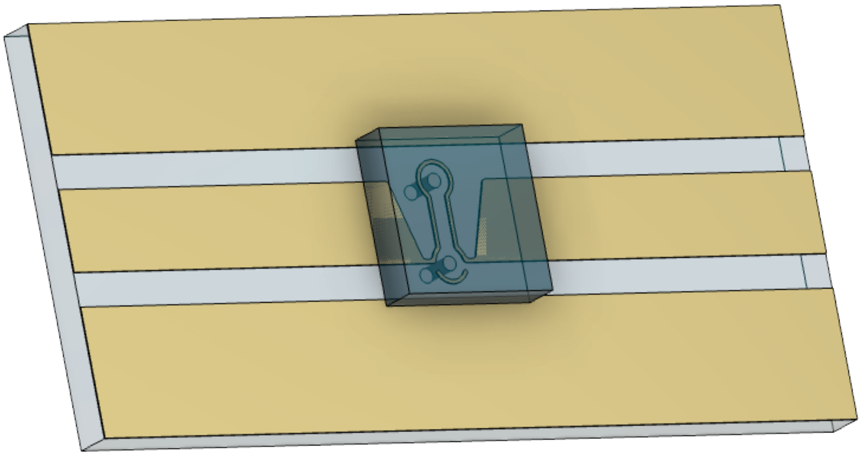

(a) The device is $21.5 \times 7.5 \times 1$ mm with a $2 \times 2 \times 1$ mm sized diamond on the surface. The omega loop is 0.8 mm in diameter and made from a 70 μm copper layer finished with gold ENIG. The substrate material is sapphire. The straight channel between the 360μm drilled holes acts as a microfluidic channel of length 2 mm. The holes act as the inlet and outlet ports for the microfluidic tubing.

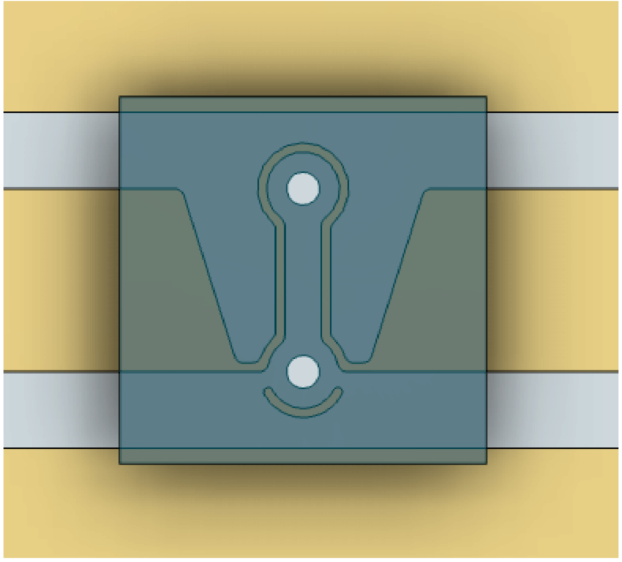

(b) Depicts a close-up view of the omega loop and diamond. The green circles and lines mark the location for glue that will be used to contain the liquid sample in the microfluidic channel.

Figure 5.1: CAD Model of Coplanar Waveguide

At the time of writing this thesis, the devices had arrived from the manufacturer Cercuits, but no measurements are available yet. However, the waveguide is based off of previous designs in the group. Assuming this new device operates similar to previous ones, it is expected to have a broadband MW response, from DC to 6 GHz, with a Rabi frequency of 15 to 30 MHz. Because its planar with a transparent substrate, the diamond can be easily glued to the waveguide's surface and optical excitation and collection can be done from both the top and bottom of the device. This design also eliminates the aforementioned cuvette as it includes a microfluidic channel (Figure **??**). The channel is 2 mm long, 0.4 mm wide, and 70 μm in height with inlet and outlet ports of diameter 360μm. Once the diamond is placed onto the waveguide, a small amount of glue can be placed around the diamond and in the green highlighted areas (Figure **??**) which will simultaneously hold the diamond in place and prevent the sample from seeping out of the channel. Eliminating the bulky cuvette will hopefully make the diamond alignment process easier. Finally, this design is projected to increase B_1 because the nuclear drive coil can be placed closer to the diamond and sample, thus increasing B_1 and its homogeneity across the detection volume. This design may even be able to simultaneously act as the RF driver without the need for an additional coil.

Ultimately, this design will expand the MW carrier frequency, increase the MW Rabi, increase B_1, eliminate the bulky cuvette, and simplify diamond alignment.

Table 5.1: Summarizes key characteristics of MW resonators used in NV and EPR experiments. The characteristics described are, in order from left to right, the type of resonator, the MW frequency (GHz), the Rabi frequency (MHz), the MW power used to produce the given Rabi, the sample size, and the loaded quality factor, Q_L. In the labeled NV experiment section, the yellow rows represent single NV experiments, while the uncolored represent ensemble NV experiments.

Paper (Year)	**Type**	**MW Freq. (GHz)**	**Rabi Freq. (MHz)**	**Power**	**Sample Size**	Q_L
NV Experiments						
[101] (2023)	Planar	2.9	20	200 mW	0.007 mm^3	2.9
[102] (2021)	quasi-optical waveguide	230	0.526	115 mW	few um^3	–
[103] (2018)	pent-loop gap	near 2.87	7.7	15.8 W	max 250 mm^3	36
[104] (2016)	Planar ring antenna	near 2.87	4.6	1 W	mm^3	6.4
[105] (2015)	TM_{110} cavity	78	0.3	–	$\approx 500\mu$m	56
EPR Experiments						
[106] (2018)	1D photonic crystal	94	Unknown	Unknown	$\approx$ uL	370
[99] (2017)	4-6 loop gap	33 - 36	35 - 150	200 W	mL	48 - 260
[100] (2017)	7 loop gap	94.17	–	10 - 100 μW	0.25 I.D. $\times$ 3 mm	150
	Rectangular TE_{U02} cavity	93.21	–	10 - 100 μW	0.1 $\times$ 2 $\times$ 6 mm	510
[107] (2017)	Surface loop gap	93.5	10	100 mW	few μm	50
[108] (2008)	Fabry-Pérot	110 - 334	0.8 - 5	10 W	few mm	–

Chapter 6: Metabolomics

The following chapter very broadly summarizes metabolomics and the advantages of NMR spectroscopy for metabolic studies. Additionally, some preliminary thoughts on utilizing a NV-NMR system to study spheroids are discussed.

6.1 Metabolomics with NMR

Metabolomics research studies cellular energy consumption and production by analyzing the metabolic concentrations and pathways associated with energy production, energy deprivation, and cellular stress [109].

Historically, the most utilized analysis tool for metabolomics is mass spectrometry (MS) because of its high proton concentration sensitivity (nanomolar or smaller), high selectivity, and minimal resource costs associated with trained personnel, initial purchase, and maintenance [63, 69]. However, in recent years, there has been an upswing in the number of studies published using NMR spectroscopy because MS has several disadvantages [69]:

1. Unlike NMR [73], MS is not an inherently quantitative analysis tool. The measured data can often not be assumed to be a direct consequence of the absolute metabolic concentration [69, 110]. If absolute concentration is desired, the data must be normalized with an additional parameter like reaction free energy [111]. Additionally, MS can only measure

net concentrations, i.e. it cannot separate the measured concentration into a sum of the metabolically available and bonded metabolites [110].

2. Although MS requires less sample than NMR, it is an entirely destructive analysis tool, so it is not typically used to for living organisms, tissue samples, or in-vivo studies [69]. Additionally, the tool's inherent destruction means it cannot be used to study dynamics, flux, and flow [63, 69]. Conversely, NMR is non-invasive and non-destructive, so it can monitor in real-time metabolic dynamics in a living system [69, 73, 112].

3. MS spectra are not as reproducible as NMR spectra which makes comparing subsequent data for the same sample unreliable [69].

4. The sample must be specially prepared for each MS method and the sample must be subjected to various ionization methods prior to a measurement so as to increase detectable metabolites [69]. Assuming no hyperpolarization, the sample can be analyzed as is in NMR.

Even though NMR is often 10 to 100 times less sensitive than MS, its other advantages, summarized above, make NMR a powerful tool for metabolic studies [69].

6.2 NV-NMR Concentration Sensitivity

Although NV-NMR is less sensitive than conventional NMR, arguably the largest advantage of NV-NMR is the small detection volumes which allows for studies of such systems like single cells [10, 13, 113], cellular response to external stimuli [10, 113], imaging of individual cells or a cluster of cells, surface or boundary effects on the millimeter or micrometer length scale [73], observation of metabolite consumption or production in real-time at the cellular surface [73], intracellular diffusion [24], or metabolic reaction rates [9, 113]. At these given lengths, it is important to assess what concentrations NV-NMR experiments can detect, and this can be analyzed in terms of concentration sensitivity:

$$\eta_{[\mathrm{M}]} = [\mathrm{M}] \times \sqrt{T}, \tag{6.1}$$

where $[\mathrm{M}]$ is the sample's molar concentration (M = mol/L) and T is the acquisition time in seconds. It is important to normalize Equation 6.1 by the measurement's SNR. For a typical conventional NMR experiment, the data reported has an SNR of three. To abide by convention, if the NV-NMR data's SNR is larger than three, the data is normalized to a value of 3.

An example concentration sensitivity for [9] is as follows: The sample was 1 mM pyridine, and for a 300 second acquisition, an SNR of 50 was reported. Equation 6.1 gives the concentration sensitivity as:

$$\eta_{[\mathrm{M}]} = \frac{1\mathrm{mM} \times \sqrt{300}}{50} \times 3 \simeq 1\mathrm{mM}/\sqrt{\mathrm{Hz}} \tag{6.2}$$

Hence, for an acquisition time of one second, the smallest measurable concentration is 1 mM.

The following table (Table 6.1) summarizes the concentration sensitivity for recent NV-NMR papers that reported experimental data.

To determine what sample concentrations are viable for NV-NMR, the minimum detectable concentration for [12], [10], and [9][1] were calculated for various acquisition times. This sample

---

[1] Only these NV-NMR papers are studied because they are the most recent experimental results for an NV en-

Table 6.1: Summarizes the sample molecule, molar concentration, acquisition time, SNR, and concentration sensitivity for several NV-NMR experiments. The colored rows are the average concentration sensitivity for a given experiment when multiple samples were reported.

Paper (Year)	**Molecule**	$[M]$	T **(s)**	**SNR**	$\eta_{[M]}$ $(\mathrm{M}/\sqrt{\mathrm{Hz}})$
[9] (2021) SABRE	Pyridine	0.001	300	50	0.0010
	Nicotinamide	0.1	2	200	0.0021
	Average	$0.0015\ \mathrm{M}/\sqrt{\mathrm{Hz}}$			
[10] (2020) DNP	*tert*-butanol	0.0053	5000	3.5	0.32
	Xylene	0.8	50	25	0.68
	Dimethylformamide	0.8	50	25	0.68
	Trimethyl phosphate	0.8	50	25	0.68
	Thymine	0.8	500	20	2.7
	Average	$1.0\ \mathrm{M}/\sqrt{\mathrm{Hz}}$			
[12] (2018) CASR	Trimethyl phosphate	8.5	3.3×10^4	3	1544
	Xylene	8.1	3.3×10^4	3	1471
	Ethyl Formate	12.4	3.5×10^4	3	2319
	Glycerol	13.7	7.2×10^4	3	3676
	Water	56	3.1×10^4	3	9859
	Average	$3773\ \mathrm{M}/\sqrt{\mathrm{Hz}}$			
[19] (2017) Qdyne	Polybutene	76	2.52×10^4	1	36193
[13] (2016) Single NV	Ubiquitin protein	–	–	–	1.1×10^6

analysis method assumes that the average concentration sensitivity reported in Table 6.1 accurately represents the average sensitivity of the experimental technique and that an SNR of three can be obtained in the given acquisition time. The results are summarized in Table 6.2.

6.2.1 Spheroids

Given this data and the length scales associated with NV-NMR detection, a potentially viable metabolic study is spheroids. Spheroids are cell clusters often used as tumor models and

---

semble with thermally polarized sample spins.

Table 6.2: Summarizes the minimum concentration measurable for a given acquisition time.

Paper (Year)	**Avg. $\eta_{[M]}$ (M/$\sqrt{\text{Hz}}$)**	**10 s**	**100 s**	**1000 s**	**10,000 s**
		Minimum Concentration (M)			
[9] (2021)	1.5×10^{-3}	4.7×10^{-4}	1.5×10^{-4}	4.7×10^{-5}	1.5×10^{-5}
[10] (2020)	1.0	0.32	0.1	0.032	0.01
[12] (2018)	3773	1193	377.3	119.3	37.7

used to explore cell-cell interactions, cellular organization, transportation of nutrients, oxygen, and intercellular signals, cell death, proliferation, cellular microenvironments, drug resistivity and metabolic production/consumption [73, 114–121].

Although there are historical studies of spheroids of size 10^6 - 10^8 cells, recent work has focused on minimizing both the number of spheroids in the detection volume and the number of cells within the spheroid. Such minimization would allow for drug efficacy studies because variations between individual spheroids could be observed [73]. Recently, [73, 118, 122] measured metabolic concentrations in spheroids containing 500 - 4000 cells. The smallest concentrations measured ranged from approximately 1 mM to 20 mM. Given these minimum concentrations, only a SABRE-based NV-NMR experiment could measure these concentrations (Table 6.2). Additionally, by implementing the QLE protocols in [8], which on average increase concentration sensitivity by a factor of five, a SABRE experiment could measure a concentration of 0.3 mM with an acquisition of one second. A CASR only NV-NMR experiment would only be viable for spheroids if the metabolic concentrations were increased by increasing the cell quantity, assuming that increasing the cell quantity increases the metabolic concentration proportionally. If the concentration were increased to 75 M (150 M), a CASR experiment could measure that concentration in 10,000 s (1000 s).

As mentioned previously, the largest advantage of the NV-NMR technique is the small detection volume which is typically on the order of 10 pL [9, 10, 12]; conversely, the smallest reported detection volume for a microfluidic conventional NMR system was 2.5 μL [73]. The maximum spheroid diameter found in the literature is 1.8 mm [114]. Even this spheroid, would sit entirely in the NV detection volume. Not only can the NV uniquely monitor the surface effects, but the small length scales make it possible for the NVs to image these surface effects in a manner similar to a Quantum Diamond Microscope [26, 34] which is unheard of in conventional NMR.

In summary, NV-NMR can measure mM concentrations using a SABRE-based experiment and have the unique advantage of monitoring and imaging metabolics at length scales unachievable with conventional NMR.

Appendix A: Diamond Characterization

The diamonds that have been historically used in the group for NV-NMR experiments are **Arya Stark (diamond ID: 1970639-03)** and **John McClane (diamond ID: 1460415-01)**.

Arya is an isotopically purified, ^{15}N, 10 μm layer on EL substrate with a nitrogen concentration of 14 ppm and an NV concentration of 2.7 ppm. Originally, Arya was a 4×4 mm diamond, but it was cut into four 2×2 mm pieces. Each piece was side angle polished so total internal reflection (TIR) of the 532 nm beam could be achieved[1]. Although Arya pieces A and B are most often used in the NV-NMR experiments, the diamond characterization data reported in this thesis is for Arya-D. However, the data should be relatively consistent across the Arya pieces. John McClane is an isotopically purified, ^{14}N, 13 μm layer on EL substrate with a nitrogen concentration[2] of 4.71×10^{18}cm^{-3}. It was also cut into four 2×2 sized pieces; the piece that is used in the NV-NMR experiments and whose characterization data is summarized in this appendix is John McClane-B. Both Arya and John McClane were grown by first growing the substrate material and then growing the nitrogen-doped layer on the substrate. Unfortunately, this method often produces diamonds with increased strain from surface imperfections and growth errors.

To minimize the material strain, a new low-strain growth method was developed by the diamond production company, Element6 (E6). In this method, the nitrogen-doped material is

---

[1] TIR is often used when one wants to avoid heating the sample [5].

[2] Measured via SIMS.

grown first and polished into the desired layer thickness. Then, the substrate is grown on the polished layer. Grown with this low-strain method, three new diamonds for NV-NMR experimentation were obtained: **Luke Skywalker (diamond ID: 2170608-01)**, **Princess Leia (diamond ID: 2170608-06)**, and **Han Solo (diamond ID: 2170608-07)**. These diamonds are all isotopically purified, ^{15}N, 10 μm layers grown on EL substrate with a nitrogen concentration of approximately 16 ppm and an NV concentration of approximately 4 ppm. Each diamond is approximately 4.6 x 4.6 x 0.5 mm in size. To confirm that the new diamonds have similar properties to the historically used NV-NMR diamonds, T_2^*, T_2, strain, and the residual ^{14}N contamination were measured.

A.1 T_2^*

Utilizing the Ramsey sequence in Section 1.3.1.3, T_2^* was measured and compared to historical data for Arya and John McClane. It was found that Luke, Leia, and Han have approximately $2\times$ longer T_2* than Arya and John McClane; essentially, the new diamonds have intrinsically longer dephasing times (Table A.1) and the measured signals have decreased linewidths (see Figures A.2, A.4, A.6, A.8**(b)** because there are less inhomogeneities inherent to the diamond material.

A.2 T_2

Utilizing the spin echo sequence in Section 1.3.2.1, it was found that the new diamonds have a T_2 that is smaller than Arya, but larger than John McClane.

Table A.1: Summarizes the T_2^* data for Luke Skywalker, Princess Leia, Han Solo, Arya Stark-D, and John McClane-B. For Luke, Leia, and Han T_2^* data was measured in five different locations on the diamond surface. The error values are the error associated with the T_2^* fit.

Location #	**Luke**	**Leia**	**Han**	**Arya**	**John**
T_2* (μs)					
1	1.331 ± 0.039	1.592 ± 0.040	1.742 ± 0.048	–	–
2	1.233 ± 0.078	1.656 ± 0.043	1.841 ± 0.046	–	–
3	1.407 ± 0.088	1.800 ± 0.049	0.270 ± 0.013	–	–
4	1.494 ± 0.087	1.525 ± 0.036	1.666 ± 0.031	–	–
5	1.378 ± 0.077	1.777 ± 0.045	1.494 ± 0.026	–	–
Average	1.3686 ± 0.0738	1.670 ± 0.0426	1.4026 ± 0.0328	0.6	0.6

Table A.2: Summarizes the spin echo T_2 data for Luke Skywalker, Princess Leia, Han Solo, Arya Stark-D, and John McClane-B. For Luke, Leia, and Han T_2 data was measured in five different locations on the diamond surface. The error values are the error associated with the T_2 fit.

Location #	**Luke**	**Leia**	**Han**	**Arya**	**John**
T_2 (μs)					
1	10.410 ± 0.69	11.493 ± 0.79	12.863 ± 0.46	–	–
2	9.598 ± 0.63	11.122 ± 0.80	12.311 ± 0.84	–	–
3	9.708 ± 0.71	10.901 ± 0.83	10.687 ± 0.80	–	–
4	9.782 ± 0.71	11.031 ± 0.81	10.697 ± 0.86	–	–
5	9.957 ± 0.72	11.133 ± 0.81	10.158 ± 0.86	–	–
Average	9.891 ± 0.692	11.136 ± 0.808	11.3432 ± 0.764	14.5	7.1

A.3 ^{14}N Contamination

Although not discussed in this thesis, the residual ^{14}N contamination can be measured with Double Electron-Electron Resonance (DEER) Electron Spin Resonance (ESR) [30]. Using this method, roughly 2% ^{14}N was measured in Luke Skywalker.

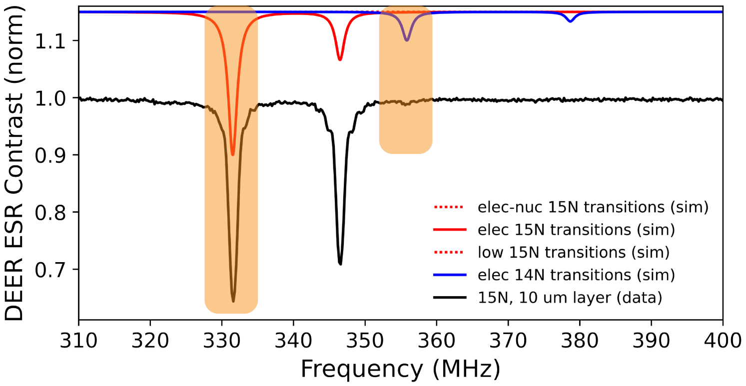

Figure A.1: Depicts the DEER ESR spectrum used to determine the residual ^{14}N contamination in Luke Skywalker. The contamination was found to be 2% by comparing the magnitude of the ^{15}N and ^{14}N peaks (orange highlighted peaks).

A.4 Strain and Linewidths

Again, although not described in this thesis, another diamond characterization method is to image the diamond material's strain and ODMR linewidths using a Quantum Diamond Microscope [26, 34]. The following sections depict the strain and linewidths for Luke, Leia, Han, and Arya[3]. Luke, Leia, and Han have eight strain and linewidth plots because the strain and linewidth of the $\mathrm{m_s} = 0 \leftrightarrow \mathrm{m_s} = +1$ and $\mathrm{m_s} = 0 \leftrightarrow \mathrm{m_s} = -1$ transition for all four diamond orientations were measured.

Out of the new diamonds, Princess Leia has the least strain and the strain that does exist is concentrated at the edges of the diamond; Luke and Han have larger strain features throughout the diamond and concentrated strain at the edges. Leia's strain looks the most similar to Arya simply because it lacks these concentrated strain features throughout the diamond. However, Arya does have a large strain gradient across much of the diamond and the new diamonds have a smaller gradient. Merely because the new diamonds do not have the strain gradient present in

---

[3] There is no strain or linewidth data on John McClane.

Arya, it seems that the low-strain growth method does minimize diamond strain.

A.4.1 Luke Skywalker

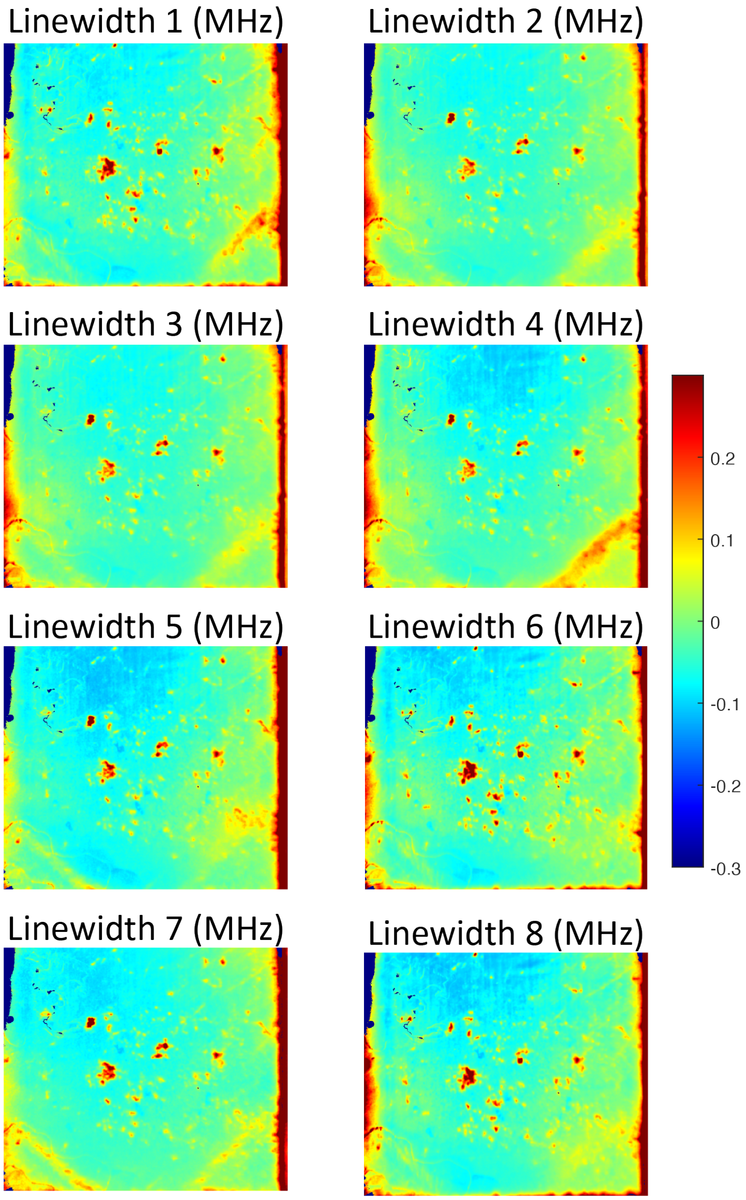

Figure A.2: Depicts the inhomogenous line broadening of the NV resonance linewidths across the entire 4×4 mm surface of Luke Skywalker. The colorbar represents this broadening in units of MHz.

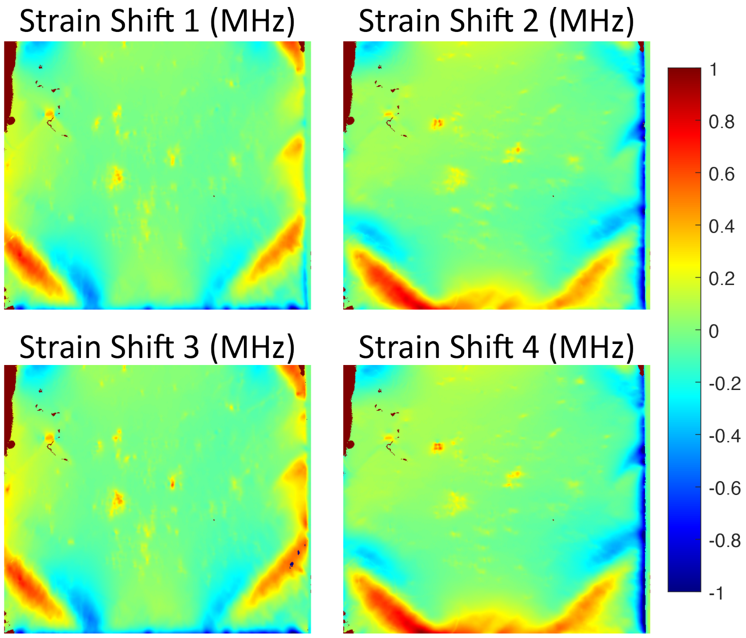

Figure A.3: Depicts the shift (in MHz) of the NV resonance frequency due to diamond strain across the entire 4×4 mm surface of Luke Skywalker. The colorbar represents MHz shifts in the resonance frequency.

A.4.2 Princess Leia

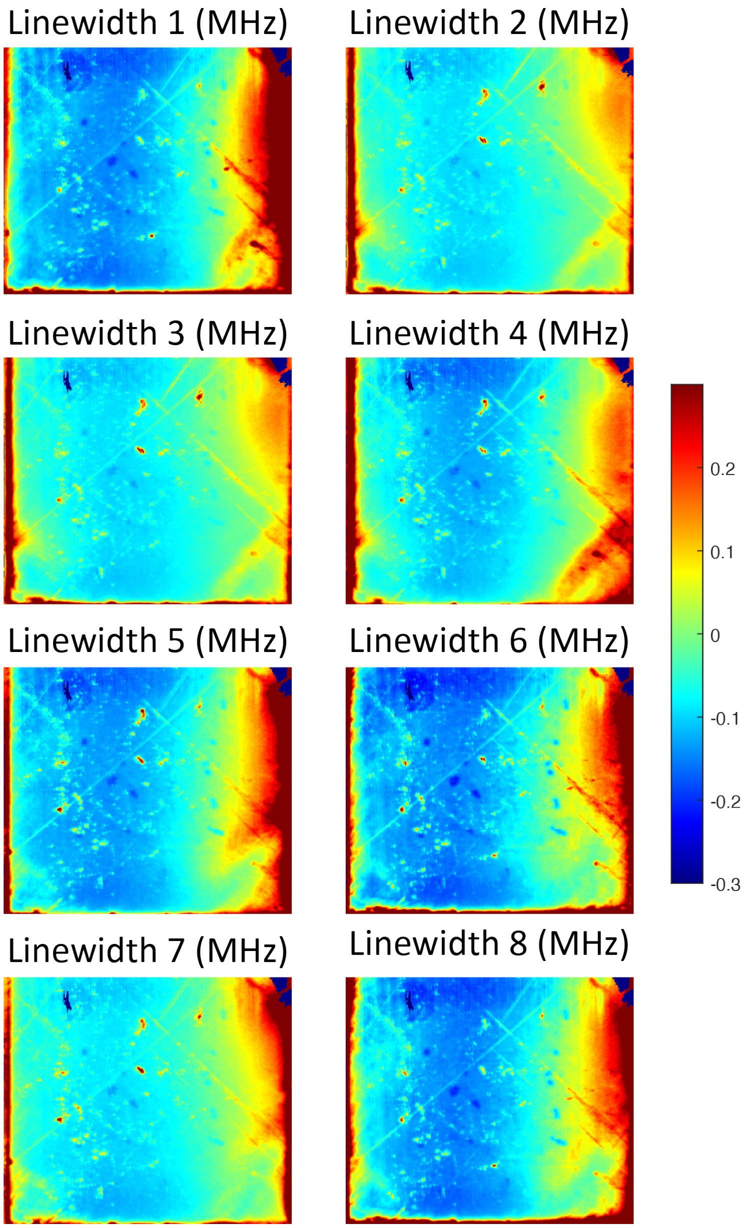

Figure A.4: Depicts the inhomogenous line broadening of the NV resonance linewidths across the entire 4×4 mm surface of Princess Leia. The colorbar represents this broadening in units of MHz.

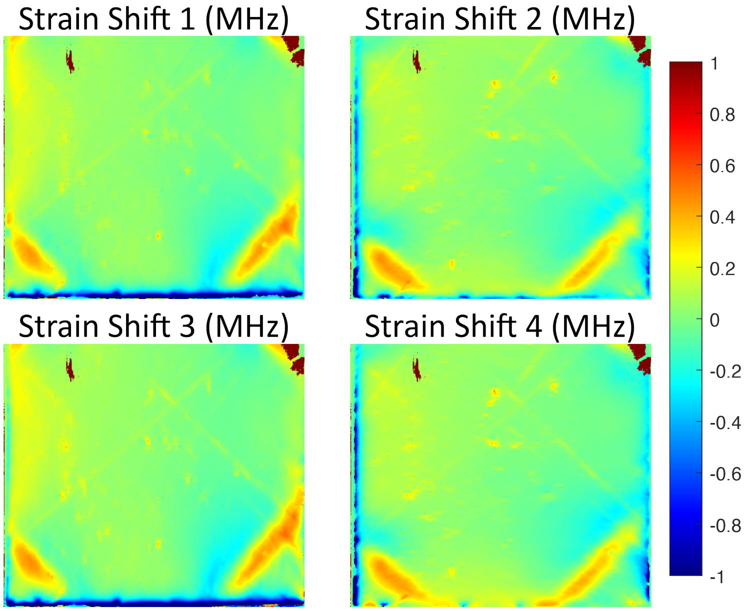

Figure A.5: Depicts the shift (in MHz) of the NV resonance frequency due to diamond strain across the entire 4×4 mm surface of Princess Leia. The colorbar represents MHz shifts in the resonance frequency.

A.4.3 Han Solo

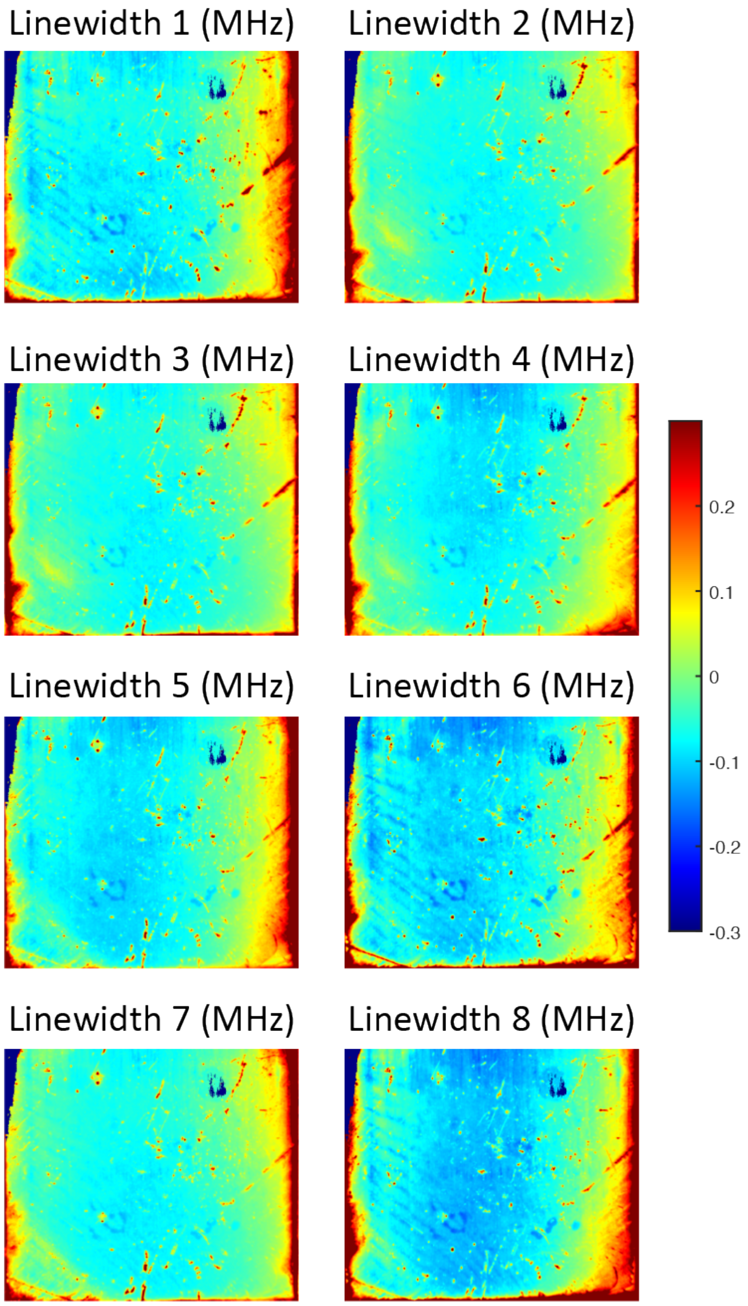

Figure A.6: Depicts the inhomogenous line broadening of the NV resonance linewidths across the entire 4×4 mm surface of Han Solo. The colorbar represents this broadening in units of MHz.

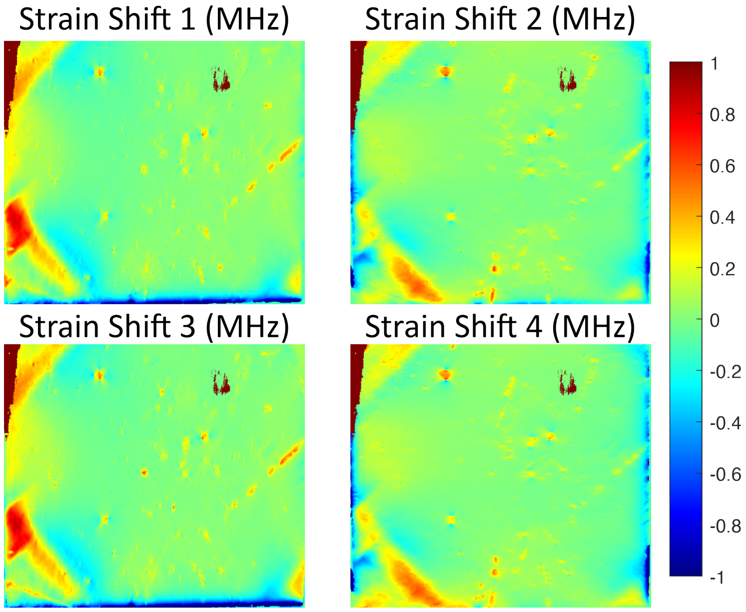

Figure A.7: Depicts the shift (in MHz) of the NV resonance frequency due to diamond strain across the entire 4×4 mm surface of Han Solo. The colorbar represents MHz shifts in the resonance frequency

A.4.4 Arya Stark-D

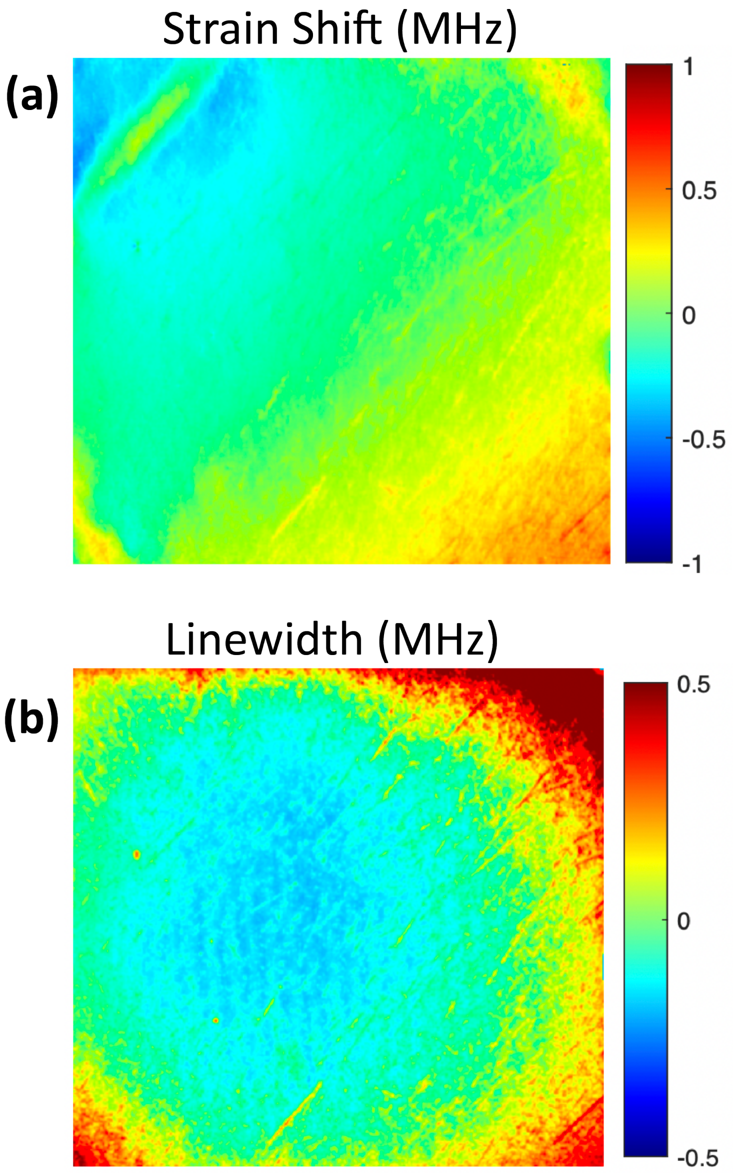

Figure A.8: N(**a**) Depicts the inhomogenous line broadening of the NV resonance linewidths across the entire 2×2 mm surface of Arya Stark-D. The colorbar represents this broadening in units of MHz. (**b**) Depicts the shift (in MHz) of the NV resonance frequency due to diamond strain across the diamond surface. The colorbars represent MHz shifts in the resonance linewidth and resonance frequency, respectively.

Bibliography

[1] M. Ashok, M. J. Turner, R. L. Walsworth, E. V. Levine, and A. P. Chandrakasan, "Hardware trojan detection using unsupervised deep learning on quantum diamond microscope magnetic field images," *J. Emerg. Technol. Comput. Syst.*, vol. 18, Oct 2022.

[2] S. M. Oliver, D. J. Martynowych, M. J. Turner, D. A. Hopper, R. L. Walsworth, and E. V. Levine, "Vector magnetic current imaging of an 8 nm process node chip and 3d current distributions using the quantum diamond microscope," *arXiv:2202.08135*, Feb 2022.

[3] M. J. Turner, N. Langellier, R. Bainbridge, D. Walters, S. Meesala, T. M. Babinec, P. Kehayias, A. Yacoby, E. Hu, M. Lončar, R. L. Walsworth, and E. V. Levine, "Magnetic Field Fingerprinting of Integrated-Circuit Activity with a Quantum Diamond Microscope," *Physical Review Applied*, vol. 14, p. 014097, July 2020.

[4] H. C. Davis, P. Ramesh, A. Bhatnagar, A. Lee-Gosselin, J. F. Barry, D. R. Glenn, R. L. Walsworth, and M. G. Shapiro, "Mapping the microscale origins of magnetic resonance image contrast with subcellular diamond magnetometry," *Nature Communications*, vol. 9, p. 131, Jan. 2018.

[5] J. F. Barry, M. J. Turner, J. M. Schloss, D. R. Glenn, Y. Song, M. D. Lukin, H. Park, and R. L. Walsworth, "Optical magnetic detection of single-neuron action potentials using quantum defects in diamond," *Proceedings of the National Academy of Sciences*, vol. 113, pp. 14133–14138, Dec. 2016.

[6] D. R. Glenn, K. Lee, H. Park, R. Weissleder, A. Yacoby, M. D. Lukin, H. Lee, R. L. Walsworth, and C. B. Connolly, "Single-cell magnetic imaging using a quantum diamond microscope," *Nature Methods*, vol. 12, pp. 736–738, Aug. 2015.

[7] D. Le Sage, K. Arai, D. R. Glenn, S. J. DeVience, L. M. Pham, L. Rahn-Lee, M. D. Lukin, A. Yacoby, A. Komeili, and R. L. Walsworth, "Optical magnetic imaging of living cells," *Nature*, vol. 496, pp. 486–489, Apr. 2013.

[8] N. Arunkumar, K. S. Olsson, J. T. Oon, C. Hart, D. B. Bucher, D. Glenn, M. D. Lukin, H. Park, D. Ham, and R. L. Walsworth, "Quantum logic enhanced sensing in solid-state spin ensembles," *arXiv:2203.12501*, Mar 2022.

[9] N. Arunkumar, D. B. Bucher, M. J. Turner, P. TomHon, D. Glenn, S. Lehmkuhl, M. D. Lukin, H. Park, M. S. Rosen, T. Theis, and R. L. Walsworth, "Micron-scale nv-nmr

spectroscopy with signal amplification by reversible exchange," *PRX Quantum*, vol. 2, p. 010305, Jan 2021.

[10] D. B. Bucher, D. R. Glenn, H. Park, M. D. Lukin, and R. L. Walsworth, "Hyperpolarization-Enhanced NMR Spectroscopy with Femtomole Sensitivity Using Quantum Defects in Diamond," *Physical Review X*, vol. 10, p. 021053, June 2020.

[11] D. B. Bucher, D. P. L. Aude Craik, M. P. Backlund, M. J. Turner, O. Ben Dor, D. R. Glenn, and R. L. Walsworth, "Quantum diamond spectrometer for nanoscale NMR and ESR spectroscopy," *Nature Protocols*, vol. 14, pp. 2707–2747, Sept. 2019.

[12] D. R. Glenn, D. B. Bucher, J. Lee, M. D. Lukin, H. Park, and R. L. Walsworth, "High-resolution magnetic resonance spectroscopy using a solid-state spin sensor," *Nature*, vol. 555, pp. 351–354, Mar. 2018.

[13] I. Lovchinsky, A. O. Sushkov, E. Urbach, N. P. d. Leon, S. Choi, K. D. Greve, R. Evans, R. Gertner, E. Bersin, C. Müller, L. McGuinness, F. Jelezko, R. L. Walsworth, H. Park, and M. D. Lukin, "Nuclear magnetic resonance detection and spectroscopy of single proteins using quantum logic," *Science*, vol. 351, pp. 836–841, Feb. 2016.

[14] I. Schwartz, J. Rosskopf, S. Schmitt, B. Tratzmiller, Q. Chen, L. P. McGuinness, F. Jelezko, and M. B. Plenio, "Blueprint for nanoscale NMR," *Scientific Reports*, vol. 9, p. 6938, May 2019. Number: 1 Publisher: Nature Publishing Group.

[15] D. Cohen, R. Nigmatullin, M. Eldar, and A. Retzker, "Confined Nano-NMR Spectroscopy Using NV Centers," *Advanced Quantum Technologies*, vol. 3, no. 11, p. 2000019, 2020. _eprint: https://onlinelibrary.wiley.com/doi/pdf/10.1002/qute.202000019.

[16] C. Munuera-Javaloy, A. Tobalina, and J. Casanova, "High-Resolution NMR Spectroscopy at Large Fields with Nitrogen Vacancy Centers," *Physical Review Letters*, vol. 130, p. 133603, Mar. 2023. Publisher: American Physical Society.

[17] N. Aslam, M. Pfender, P. Neumann, R. Reuter, A. Zappe, F. Fávaro de Oliveira, A. Denisenko, H. Sumiya, S. Onoda, J. Isoya, and J. Wrachtrup, "Nanoscale nuclear magnetic resonance with chemical resolution," *Science*, vol. 357, pp. 67–71, July 2017. Publisher: American Association for the Advancement of Science.

[18] D. Rugar, H. J. Mamin, M. H. Sherwood, M. Kim, C. T. Rettner, K. Ohno, and D. D. Awschalom, "Proton magnetic resonance imaging using a nitrogen–vacancy spin sensor," *Nature Nanotechnology*, vol. 10, pp. 120–124, Feb. 2015. Number: 2 Publisher: Nature Publishing Group.

[19] S. Schmitt, T. Gefen, F. M. Stürner, T. Unden, G. Wolff, C. Müller, J. Scheuer, B. Naydenov, M. Markham, S. Pezzagna, J. Meijer, I. Schwarz, M. Plenio, A. Retzker, L. P. McGuinness, and F. Jelezko, "Submillihertz magnetic spectroscopy performed with a nanoscale quantum sensor," *Science*, vol. 356, pp. 832–837, May 2017. Publisher: American Association for the Advancement of Science.

[20] B. Fortman, J. Pena, K. Holczer, and S. Takahashi, "Demonstration of NV-detected ESR spectroscopy at 115 GHz and 4.2 T," *Applied Physics Letters*, vol. 116, p. 174004, Apr. 2020. Publisher: American Institute of Physics.

[21] B. P. Weiss, R. R. Fu, J. F. Einsle, D. R. Glenn, P. Kehayias, E. A. Bell, J. Gelb, J. F. D. F. Araujo, E. A. Lima, C. S. Borlina, P. Boehnke, D. N. Johnstone, T. M. Harrison, R. J. Harrison, and R. L. Walsworth, "Secondary magnetic inclusions in detrital zircons from the Jack Hills, Western Australia, and implications for the origin of the geodynamo," *Geology*, vol. 46, pp. 427–430, May 2018.

[22] D. R. Glenn, R. R. Fu, P. Kehayias, D. L. Sage, E. A. Lima, B. P. Weiss, and R. L. Walsworth, "Micrometer-scale magnetic imaging of geological samples using a quantum diamond microscope," *Geochemistry, Geophysics, Geosystems*, vol. 18, no. 8, pp. 3254–3267, 2017.

[23] R. R. Fu, B. P. Weiss, E. A. Lima, P. Kehayias, J. F. D. F. Araujo, D. R. Glenn, J. Gelb, J. F. Einsle, A. M. Bauer, R. J. Harrison, G. A. H. Ali, and R. L. Walsworth, "Evaluating the paleomagnetic potential of single zircon crystals using the Bishop Tuff," *Earth and Planetary Science Letters*, vol. 458, pp. 1–13, Jan. 2017.

[24] F. Bruckmaier, R. D. Allert, N. R. Neuling, P. Amrein, S. Littin, K. D. Briegel, P. Schätzle, P. Knittel, M. Zaitsev, and D. B. Bucher, "Imaging local diffusion in microstructures using NV-based pulsed field gradient NMR," Mar. 2023. arXiv:2303.03516 [physics].

[25] P. Kehayias, M. J. Turner, R. Trubko, J. M. Schloss, C. A. Hart, M. Wesson, D. R. Glenn, and R. L. Walsworth, "Imaging crystal stress in diamond using ensembles of nitrogen-vacancy centers," *Physical Review B*, vol. 100, p. 174103, Nov. 2019.

[26] E. V. Levine, M. J. Turner, P. Kehayias, C. A. Hart, N. Langellier, R. Trubko, D. R. Glenn, R. R. Fu, and R. L. Walsworth, "Principles and techniques of the quantum diamond microscope," *Nanophotonics*, vol. 8, pp. 1945–1973, Sept. 2019.

[27] R. Ebadi, M. C. Marshall, D. F. Phillips, J. Cremer, T. Zhou, M. Titze, P. Kehayias, M. Saleh Ziabari, N. Delegan, S. Rajendran, A. O. Sushkov, F. J. Heremans, E. S. Bielejec, M. V. Holt, and R. L. Walsworth, "Directional detection of dark matter using solid-state quantum sensing," *AVS Quantum Science*, vol. 4, p. 044701, Nov 2022.

[28] S. Rajendran, N. Zobrist, A. O. Sushkov, R. Walsworth, and M. Lukin, "A method for directional detection of dark matter using spectroscopy of crystal defects," *Physical Review D*, vol. 96, p. 035009, Aug. 2017.

[29] N. Aslam, G. Waldherr, P. Neumann, F. Jelezko, and J. Wrachtrup, "Photo-induced ionization dynamics of the nitrogen vacancy defect in diamond investigated by single-shot charge state detection," *New Journal of Physics*, vol. 15, p. 013064, Jan. 2013. Publisher: IOP Publishing.

[30] C. A. Hart, *Experimental Realization of Improved Magnetic Sensing and Imaging in Ensembles of Nitrogen Vacancy Centers in Diamond*. PhD thesis, Harvard University, 2020.

[31] S. D. Subedi, V. V. Fedorov, J. Peppers, D. V. Martyshkin, S. B. Mirov, L. Shao, and M. Loncar, "Laser spectroscopic characterization of negatively charged nitrogen-vacancy (NV^{+}) centers in diamond," *Optical Materials Express*, vol. 9, pp. 2076–2087, May 2019. Publisher: Optica Publishing Group.

[32] J. F. Barry, J. M. Schloss, E. Bauch, M. J. Turner, C. A. Hart, L. M. Pham, and R. L. Walsworth, "Sensitivity optimization for NV-diamond magnetometry," *Reviews of Modern Physics*, vol. 92, p. 015004, Mar. 2020. Publisher: American Physical Society.

[33] S. J. DeVience, *Nuclear Magnetic Resonance with Spin Singlet States and Nitrogen Vacancy Centers in Diamond*. PhD thesis, Harvard University, 2014.

[34] M. J. Turner, *Quantum Diamond Microscopes for Biological Systems and Integrated Circuits*. PhD thesis, Harvard University, 2020.

[35] L. M. Pham, *Magnetic Field Sensing with Nitrogen-Vacancy Color Centers in Diamond*. PhD thesis, Harvard University, 2013.

[36] C. S. Shin, C. E. Avalos, M. C. Butler, D. R. Trease, S. J. Seltzer, J. Peter Mustonen, D. J. Kennedy, V. M. Acosta, D. Budker, A. Pines, and V. S. Bajaj, "Room-temperature operation of a radiofrequency diamond magnetometer near the shot-noise limit," *Journal of Applied Physics*, vol. 112, p. 124519, Dec. 2012.

[37] A. Horsley, P. Appel, J. Wolters, J. Achard, A. Tallaire, P. Maletinsky, and P. Treutlein, "Microwave device characterization using a widefield diamond microscope," *Phys. Rev. Appl.*, vol. 10, p. 044039, Oct 2018.

[38] V. V. Dobrovitski, A. E. Feiguin, D. D. Awschalom, and R. Hanson, "Decoherence dynamics of a single spin versus spin ensemble," *Physical Review B*, vol. 77, p. 245212, June 2008. Publisher: American Physical Society.

[39] M. V. Vaidya, C. M. Collins, D. K. Sodickson, R. Brown, G. C. Wiggins, and R. Lattanzi, "Dependence of B1+ and B1+ Field Patterns of Surface Coils on the Electrical Properties of the Sample and the MR Operating Frequency," *Concepts in magnetic resonance. Part B, Magnetic resonance engineering*, vol. 46, pp. 25–40, Feb. 2016.

[40] N. F. Ramsey, "A Molecular Beam Resonance Method with Separated Oscillating Fields," *Physical Review*, vol. 78, pp. 695–699, June 1950.

[41] J. M. Taylor, P. Cappellaro, L. Childress, L. Jiang, D. Budker, P. R. Hemmer, A. Yacoby, R. Walsworth, and M. D. Lukin, "High-sensitivity diamond magnetometer with nanoscale resolution," *Nature Physics*, vol. 4, pp. 810–816, Oct. 2008. Number: 10 Publisher: Nature Publishing Group.

[42] J. T. Oon, J. Tang, C. A. Hart, K. S. Olsson, M. J. Turner, J. M. Schloss, and R. L. Walsworth, "Ramsey envelope modulation in nv diamond magnetometry," *Phys. Rev. B*, vol. 106, p. 054110, Aug 2022.

[43] M. C. Marshall, R. Ebadi, C. Hart, M. J. Turner, M. J. Ku, D. F. Phillips, and R. L. Walsworth, “High-precision mapping of diamond crystal strain using quantum interferometry,” *Phys. Rev. Applied*, vol. 17, p. 024041, Feb 2022.

[44] J. M. Schloss, J. F. Barry, M. J. Turner, and R. L. Walsworth, “Simultaneous Broadband Vector Magnetometry Using Solid-State Spins,” *Physical Review Applied*, vol. 10, p. 034044, Sept. 2018.

[45] G. Balasubramanian, P. Neumann, D. Twitchen, M. Markham, R. Kolesov, N. Mizuochi, J. Isoya, J. Achard, J. Beck, J. Tissler, V. Jacques, P. R. Hemmer, F. Jelezko, and J. Wrachtrup, “Ultralong spin coherence time in isotopically engineered diamond,” *Nature Materials*, vol. 8, pp. 383–387, May 2009. Number: 5 Publisher: Nature Publishing Group.

[46] A. M. Edmonds, C. A. Hart, M. J. Turner, P.-O. Colard, J. M. Schloss, K. Olsson, R. Trubko, M. L. Markham, A. Rathmill, B. Horne-Smith, W. Lew, A. Manickam, S. Bruce, P. G. Kaup, J. C. Russo, M. J. DiMario, J. T. South, J. T. Hansen, D. J. Twitchen, and R. Walsworth, “Characterisation of CVD diamond with high concentrations of nitrogen for magnetic-field sensing applications,” *Materials for Quantum Technology*, vol. 1, p. 025001, Jan. 2021.

[47] E. Bauch, S. Singh, J. Lee, C. A. Hart, J. M. Schloss, M. J. Turner, J. F. Barry, L. Pham, N. Bar-Gill, S. F. Yelin, and R. L. Walsworth, “Decoherence of dipolar spin ensembles in diamond,” *arXiv:1904.08763 [physics, physics:quant-ph]*, Apr. 2019.

[48] E. Bauch, C. A. Hart, J. M. Schloss, M. J. Turner, J. F. Barry, P. Kehayias, S. Singh, and R. L. Walsworth, “Ultralong Dephasing Times in Solid-State Spin Ensembles via Quantum Control,” *Physical Review X*, vol. 8, p. 031025, July 2018.

[49] G. de Lange, Z. H. Wang, D. Ristè, V. V. Dobrovitski, and R. Hanson, “Universal Dynamical Decoupling of a Single Solid-State Spin from a Spin Bath,” *Science*, vol. 330, pp. 60–63, Oct. 2010. Publisher: American Association for the Advancement of Science.

[50] L. Cywinski, R. M. Lutchyn, C. P. Nave, and S. Das Sarma, “How to enhance dephasing time in superconducting qubits,” *Physical Review B*, vol. 77, p. 174509, May 2008. Publisher: American Physical Society.

[51] T. Gullion, D. B. Baker, and M. S. Conradi, “New, compensated Carr-Purcell sequences,” *Journal of Magnetic Resonance (1969)*, vol. 89, pp. 479–484, Oct. 1990.

[52] M. A. Ali Ahmed, G. A. Álvarez, and D. Suter, “Robustness of dynamical decoupling sequences,” *Physical Review A*, vol. 87, p. 042309, Apr. 2013. Publisher: American Physical Society.

[53] F. Bloch, W. W. Hansen, and M. Packard, “Nuclear Induction,” *Physical Review*, vol. 69, pp. 127–127, Feb. 1946. Publisher: American Physical Society.

[54] E. M. Purcell, H. C. Torrey, and R. V. Pound, “Resonance Absorption by Nuclear Magnetic Moments in a Solid,” *Physical Review*, vol. 69, pp. 37–38, Jan. 1946. Publisher: American Physical Society.

[55] E. D. Becker, “A BRIEF HISTORY OF NUCLEAR MAGNETIC RESONANCE,” *Analytical Chemistry*, vol. 65, pp. 295A–302A, Mar. 1993. Publisher: American Chemical Society.

[56] D. E. Wemmer, “Homonuclear correlated spectroscopy (COSY): The basics of two-dimensional NMR,” *Concepts in Magnetic Resonance*, vol. 1, no. 2, pp. 59–72, 1989. _eprint: https://onlinelibrary.wiley.com/doi/pdf/10.1002/cmr.1820010204.

[57] F. A. L. Anet and A. J. R. Bourn, “Nuclear Magnetic Resonance Spectral Assignments from Nuclear Overhauser Effects1,” *Journal of the American Chemical Society*, vol. 87, pp. 5250–5251, Nov. 1965. Publisher: American Chemical Society.

[58] D. Marion, “An Introduction to Biological NMR Spectroscopy *,” *Molecular & Cellular Proteomics*, vol. 12, pp. 3006–3025, Nov. 2013. Publisher: Elsevier.

[59] P. J. Hore, “Solvent suppression in fourier transform nuclear magnetic resonance,” *Journal of Magnetic Resonance (1969)*, vol. 55, pp. 283–300, Nov. 1983.

[60] W. S. Price, “Water Signal Suppression in NMR Spectroscopy,” in *Annual Reports on NMR Spectroscopy* (G. A. Webb, ed.), vol. 38, pp. 289–354, Academic Press, Jan. 1999.

[61] G. Giovannetti, V. Hartwig, V. Positano, and N. Vanello, “Radiofrequency Coils for Magnetic Resonance Applications: Theory, Design, and Evaluation,” *Critical Reviews in Biomedical Engineering*, vol. 42, no. 2, 2014. Publisher: Begel House Inc.

[62] T. L. Peck, R. L. Magin, and P. C. Lauterbur, “Design and Analysis of Microcoils for NMR Microscopy,” *Journal of Magnetic Resonance, Series B*, vol. 108, pp. 114–124, Aug. 1995.

[63] A.-H. M. Emwas, “The strengths and weaknesses of nmr spectroscopy and mass spectrometry with particular focus on metabolomics research,” in *Metabonomics* (J. Bjerrum, ed.), no. 1277 in Methods in Molecular Biology, ch. 13, pp. 161–194, Humana Press, 2015.

[64] M. H. Levitt, *Spin Dynamics Basics of Nuclear Magnetic Resonance*. John Wiley and Sons, second ed., 2008.

[65] B. E. Herzog, D. Cadeddu, F. Xue, P. Peddibhotla, and M. Poggio, “Boundary between the thermal and statistical polarization regimes in a nuclear spin ensemble,” *Applied Physics Letters*, vol. 105, p. 043112, Aug. 2014.

[66] R. Harris, *Modern Physics*. Pearson Addison-Wesley, second ed., 2008.

[67] D. Freude, *Spectroscopy*, ch. Chapter 4: Nuclear Magnetic Resonance. Universität Leipzig, 2006.

[68] M. P. M. Letertre, P. Giraudeau, and P. de Tullio, "Nuclear Magnetic Resonance Spectroscopy in Clinical Metabolomics and Personalized Medicine: Current Challenges and Perspectives," *Frontiers in Molecular Biosciences*, vol. 8, 2021.

[69] A.-H. Emwas, R. Roy, R. T. McKay, L. Tenori, E. Saccenti, G. A. N. Gowda, D. Raftery, F. Alahmari, L. Jaremko, M. Jaremko, and D. S. Wishart, "NMR Spectroscopy for Metabolomics Research," *Metabolites*, vol. 9, p. 123, July 2019. Number: 7 Publisher: Multidisciplinary Digital Publishing Institute.

[70] J. Giberson, J. Scicluna, N. Legge, and J. Longstaffe, "Developments in benchtop NMR spectroscopy 2015–2020," in *Annual Reports on NMR Spectroscopy*, vol. 102, pp. 153–246, Elsevier, 2021.

[71] P. Nikolaou, B. M. Goodson, and E. Y. Chekmenev, "NMR Hyperpolarization Techniques for Biomedicine," *Chemistry – A European Journal*, vol. 21, pp. 3156–3166, Feb. 2015.

[72] K. S. Liu, A. Henning, M. W. Heindl, R. D. Allert, J. D. Bartl, I. D. Sharp, R. Rizzato, and D. B. Bucher, "Surface NMR using quantum sensors in diamond," *Proceedings of the National Academy of Sciences*, vol. 119, p. e2111607119, Feb. 2022. Publisher: Proceedings of the National Academy of Sciences.

[73] B. Patra, M. Sharma, W. Hale, and M. Utz, "Time-resolved non-invasive metabolomic monitoring of a single cancer spheroid by microfluidic NMR," *Scientific Reports*, vol. 11, p. 53, Jan. 2021. Number: 1 Publisher: Nature Publishing Group.

[74] J. Holzgrafe, Q. Gu, J. Beitner, D. M. Kara, H. S. Knowles, and M. Atatüre, "Nanoscale NMR Spectroscopy Using Nanodiamond Quantum Sensors," *Physical Review Applied*, vol. 13, p. 044004, Apr. 2020. Publisher: American Physical Society.

[75] H. Mamin, M. Sherwood, M. Kim, C. Rettner, K. Ohno, D. Awschalom, and D. Rugar, "Multipulse Double-Quantum Magnetometry with Near-Surface Nitrogen-Vacancy Centers," *Physical Review Letters*, vol. 113, p. 030803, July 2014. Publisher: American Physical Society.

[76] R. Rizzato, F. Bruckmaier, K. S. Liu, S. J. Glaser, and D. B. Bucher, "Polarization transfer from optically-pumped NV center ensembles to multinuclear spin baths," *arXiv:2111.11804 [cond-mat, physics:physics]*, Nov. 2021. arXiv: 2111.11804.

[77] A. Healey, L. Hall, G. White, T. Teraji, M.-A. Sani, F. Separovic, J.-P. Tetienne, and L. Hollenberg, "Polarization Transfer to External Nuclear Spins Using Ensembles of Nitrogen-Vacancy Centers," *Physical Review Applied*, vol. 15, p. 054052, May 2021. Publisher: American Physical Society.

[78] J. Tetienne, L. T. Hall, A. J. Healey, G. A. L. White, M. Sani, F. Separovic, and L. C. L. Hollenberg, "Prospects for nuclear spin hyperpolarization of molecular samples using nitrogen-vacancy centers in diamond," *Physical Review B*, vol. 103, p. 014434, Jan. 2021. Publisher: American Physical Society.

[79] H. Espinós, C. Munuera-Javaloy, I. Panadero, P. Acedo, R. Puebla, J. Casanova, and E. Torrontegui, “Enhancing polarization transfer from nitrogen-vacancy centers in diamond to external nuclear spins via dangling bond mediators,” *arXiv*, May 2023. arXiv:2304.14282 [quant-ph].

[80] D. E. J. Waddington, M. Sarracanie, H. Zhang, N. Salameh, D. R. Glenn, E. Rej, T. Gaebel, T. Boele, R. L. Walsworth, D. J. Reilly, and M. S. Rosen, “Nanodiamond-enhanced MRI via in situ hyperpolarization,” *Nature Communications*, vol. 8, p. 15118, Apr. 2017.

[81] O. Sahin, E. de Leon Sanchez, S. Conti, A. Akkiraju, P. Reshetikhin, E. Druga, A. Aggarwal, B. Gilbert, S. Bhave, and A. Ajoy, “High field magnetometry with hyperpolarized nuclear spins,” *Nature Communications*, vol. 13, p. 5486, Sept. 2022. Number: 1 Publisher: Nature Publishing Group.

[82] J. Scheuer, I. Schwartz, S. Müller, Q. Chen, I. Dhand, M. B. Plenio, B. Naydenov, and F. Jelezko, “Robust techniques for polarization and detection of nuclear spin ensembles,” *Physical Review B*, vol. 96, p. 174436, Nov. 2017. Publisher: American Physical Society.

[83] J. P. King, K. Jeong, C. C. Vassiliou, C. S. Shin, R. H. Page, C. E. Avalos, H.-J. Wang, and A. Pines, “Room-temperature in situ nuclear spin hyperpolarization from optically pumped nitrogen vacancy centres in diamond,” *Nature Communications*, vol. 6, p. 8965, Dec. 2015. Number: 1 Publisher: Nature Publishing Group.

[84] J. P. King, P. J. Coles, and J. A. Reimer, “Optical polarization of `$^{13}\text{C}$` nuclei in diamond through nitrogen vacancy centers,” *Physical Review B*, vol. 81, p. 073201, Feb. 2010. Publisher: American Physical Society.

[85] Y.-X. Shang, F. Hong, J.-H. Dai, Y.-N. Lu, H. Yu, Y.-H. Yu, X.-H. Yu, X.-Y. Pan, and G.-Q. Liu, “High-Pressure NMR Enabled by Diamond Nitrogen-Vacancy Centers,” Mar. 2022. arXiv:2203.10511 [quant-ph].

[86] M. S. Grinolds, P. Maletinsky, S. Hong, M. D. Lukin, R. L. Walsworth, and A. Yacoby, “Quantum control of proximal spins using nanoscale magnetic resonance imaging,” *Nature Physics*, vol. 7, pp. 687–692, Sept. 2011.

[87] M. S. Grinolds, M. Warner, K. De Greve, Y. Dovzhenko, L. Thiel, R. L. Walsworth, S. Hong, P. Maletinsky, and A. Yacoby, “Subnanometre resolution in three-dimensional magnetic resonance imaging of individual dark spins,” *Nature Nanotechnology*, vol. 9, pp. 279–284, Apr. 2014.

[88] A. O. Sushkov, N. Chisholm, I. Lovchinsky, M. Kubo, P. K. Lo, S. D. Bennett, D. Hunger, A. Akimov, R. L. Walsworth, H. Park, and M. D. Lukin, “All-Optical Sensing of a Single-Molecule Electron Spin,” *Nano Letters*, vol. 14, pp. 6443–6448, Nov. 2014.

[89] A. Sushkov, I. Lovchinsky, N. Chisholm, R. Walsworth, H. Park, and M. Lukin, “Magnetic Resonance Detection of Individual Proton Spins Using Quantum Reporters,” *Physical Review Letters*, vol. 113, p. 197601, Nov. 2014.

[90] A. Ajoy, U. Bissbort, M. Lukin, R. Walsworth, and P. Cappellaro, "Atomic-Scale Nuclear Spin Imaging Using Quantum-Assisted Sensors in Diamond," *Physical Review X*, vol. 5, p. 011001, Jan. 2015.

[91] L. M. Pham, S. J. DeVience, F. Casola, I. Lovchinsky, A. O. Sushkov, E. Bersin, J. Lee, E. Urbach, P. Cappellaro, H. Park, A. Yacoby, M. Lukin, and R. L. Walsworth, "NMR technique for determining the depth of shallow nitrogen-vacancy centers in diamond," *Physical Review B*, vol. 93, p. 045425, Jan. 2016.

[92] H. Zhang, K. Arai, C. Belthangady, J. Jaskula, and R. L. Walsworth, "Selective addressing of solid-state spins at the nanoscale via magnetic resonance frequency encoding," *npj Quantum Information*, vol. 3, pp. 1–8, Aug. 2017.

[93] D. Daly, S. J. DeVience, E. Huckestein, J. Cremer, J. W. Blanchard, and R. L. Walsworth, "Nutation-based longitudinal sensing protocols for high-field nmr with nitrogen vacancy centers in diamond," 2023.

[94] J. Choi, H. Zhou, H. S. Knowles, R. Landig, S. Choi, and M. D. Lukin, "Robust Dynamic Hamiltonian Engineering of Many-Body Spin Systems," *Physical Review X*, vol. 10, p. 031002, July 2020. Publisher: American Physical Society.

[95] S. J. DeVience, L. M. Pham, I. Lovchinsky, A. O. Sushkov, N. Bar-Gill, C. Belthangady, F. Casola, M. Corbett, H. Zhang, M. Lukin, H. Park, A. Yacoby, and R. L. Walsworth, "Nanoscale NMR spectroscopy and imaging of multiple nuclear species," *Nature Nanotechnology*, vol. 10, pp. 129–134, Feb. 2015.

[96] T. Staudacher, F. Shi, S. Pezzagna, J. Meijer, J. Du, C. A. Meriles, F. Reinhard, and J. Wrachtrup, "Nuclear Magnetic Resonance Spectroscopy on a (5-Nanometer)3 Sample Volume," *Science*, vol. 339, pp. 561–563, Feb. 2013. Publisher: American Association for the Advancement of Science.

[97] H. J. Mamin, M. Kim, M. H. Sherwood, C. T. Rettner, K. Ohno, D. D. Awschalom, and D. Rugar, "Nanoscale Nuclear Magnetic Resonance with a Nitrogen-Vacancy Spin Sensor," *Science*, vol. 339, pp. 557–560, Feb. 2013. Publisher: American Association for the Advancement of Science.

[98] S. Z. Kiss, A. M. Rostas, L. Heidinger, N. Spengler, M. V. Meissner, N. MacKinnon, E. Schleicher, S. Weber, and J. G. Korvink, "A microwave resonator integrated on a polymer microfluidic chip," *Journal of Magnetic Resonance*, vol. 270, pp. 169–175, Sept. 2016.

[99] R. Tschaggelar, F. D. Breitgoff, O. Oberhänsli, M. Qi, A. Godt, and G. Jeschke, "High-Bandwidth Q-Band EPR Resonators," *Applied Magnetic Resonance*, vol. 48, pp. 1273–1300, Dec. 2017.

[100] J. W. Sidabras, T. Sarna, R. R. Mett, and J. S. Hyde, "Uniform field loop-gap resonator and rectangular TEU02 for aqueous sample EPR at 94GHz," *Journal of Magnetic Resonance*, vol. 282, pp. 129–135, Sept. 2017.

[101] A. Savitsky, J. Zhang, and D. Suter, “Variable bandwidth, high efficiency microwave resonator for control of spin-qubits in nitrogen-vacancy centers,” *Review of Scientific Instruments*, vol. 94, p. 023101, Feb. 2023. arXiv:2301.03911 [quant-ph].

[102] B. Fortman, L. Mugica-Sanchez, N. Tischler, C. Selco, Y. Hang, K. Holczer, and S. Takahashi, “Electron–electron double resonance detected NMR spectroscopy using ensemble NV centers at 230 GHz and 8.3 T,” *Journal of Applied Physics*, vol. 130, p. 083901, Aug. 2021.

[103] E. R. Eisenach, J. F. Barry, L. M. Pham, R. G. Rojas, D. R. Englund, and D. A. Braje, “Broadband loop gap resonator for nitrogen vacancy centers in diamond,” *Review of Scientific Instruments*, vol. 89, p. 094705, Sept. 2018.

[104] K. Sasaki, Y. Monnai, S. Saijo, R. Fujita, H. Watanabe, J. Ishi-Hayase, K. M. Itoh, and E. Abe, “Broadband, large-area microwave antenna for optically detected magnetic resonance of nitrogen-vacancy centers in diamond,” *Review of Scientific Instruments*, vol. 87, p. 053904, May 2016.

[105] N. Aslam, M. Pfender, R. Stöhr, P. Neumann, M. Scheffler, H. Sumiya, H. Abe, S. Onoda, T. Ohshima, J. Isoya, and J. Wrachtrup, “Single spin optically detected magnetic resonance with 60–90 GHz (E-band) microwave resonators,” *Review of Scientific Instruments*, vol. 86, p. 064704, June 2015.

[106] S. Milikisiyants, A. A. Nevzorov, and A. I. Smirnov, “Photonic band-gap resonators for high-field/high-frequency EPR of microliter-volume liquid aqueous samples,” *Journal of Magnetic Resonance*, vol. 296, pp. 152–164, Nov. 2018.

[107] Y. Twig, A. Sorkin, D. Cristea, A. Feintuch, and A. Blank, “Surface loop-gap resonators for electron spin resonance at W-band,” *Review of Scientific Instruments*, vol. 88, p. 123901, Dec. 2017.

[108] G. W. Morley, L.-C. Brunel, and J. van Tol, “A multifrequency high-field pulsed electron paramagnetic resonance/electron-nuclear double resonance spectrometer,” *Review of Scientific Instruments*, vol. 79, p. 064703, June 2008.

[109] I. Alshamleh, N. Krause, C. Richter, N. Kurrle, H. Serve, U. L. Günther, and H. Schwalbe, “Real-Time NMR Spectroscopy for Studying Metabolism,” *Angewandte Chemie International Edition*, vol. 59, no. 6, pp. 2304–2308, 2020. _eprint: https://onlinelibrary.wiley.com/doi/pdf/10.1002/anie.201912919.

[110] D. G. Gadian and G. K. Radda, “NMR studies of tissue metabolism,” *Annual Review of Biochemistry*, vol. 50, pp. 69–83, 1981.

[111] J. O. Park, S. A. Rubin, Y.-F. Xu, D. Amador-Noguez, J. Fan, T. Shlomi, and J. D. Rabinowitz, “Metabolite concentrations, fluxes and free energies imply efficient enzyme usage,” *Nature Chemical Biology*, vol. 12, pp. 482–489, July 2016.

[112] D. G. Gadian, “Whole Organ Metabolism Studied by NMR,” *Annual Review of Biophysics and Bioengineering*, vol. 12, pp. 69–89, June 1983.

[113] N. R. Neuling, R. D. Allert, and D. B. Bucher, “Prospects of Single-Cell NMR Spectroscopy with Quantum Sensors,” June 2023. arXiv:2306.07593 [physics].

[114] A. Palma, S. Grande, A. M. Luciani, V. Mlynárik, L. Guidoni, V. Viti, and A. Rosi, “Metabolic Study of Breast MCF-7 Tumor Spheroids after Gamma Irradiation by 1H NMR Spectroscopy and Microimaging,” *Frontiers in Oncology*, vol. 6, 2016.

[115] A. Kalfe, A. Telfah, J. Lambert, and R. Hergenröder, “Looking into Living Cell Systems: Planar Waveguide Microfluidic NMR Detector for in Vitro Metabolomics of Tumor Spheroids,” *Analytical Chemistry*, vol. 87, pp. 7402–7410, July 2015. Publisher: American Chemical Society.

[116] M. T. Santini, G. Rainaldi, R. Romano, A. Ferrante, S. Clemente, A. Motta, and P. L. Indovina, “MG-63 human osteosarcoma cells grown in monolayer and as three-dimensional tumor spheroids present a different metabolic profile: a 1H NMR study,” *FEBS Letters*, vol. 557, no. 1-3, pp. 148–154, 2004. _eprint: https://onlinelibrary.wiley.com/doi/pdf/10.1016/S0014-5793%2803%2901466-2.

[117] M. Rusz, E. Rampler, B. K. Keppler, M. A. Jakupec, and G. Koellensperger, “Single Spheroid Metabolomics: Optimizing Sample Preparation of Three-Dimensional Multicellular Tumor Spheroids,” *Metabolites*, vol. 9, p. 304, Dec. 2019. Number: 12 Publisher: Multidisciplinary Digital Publishing Institute.

[118] G. Rogers, S. Barker, M. Sharma, S. Khakoo, and M. Utz, “Operando NMR metabolomics of a microfluidic cell culture,” *Journal of Magnetic Resonance*, vol. 349, p. 107405, Apr. 2023.

[119] Q. Yang, G. Bae, G. Nadiradze, A. Castagna, G. Berezhnoy, L. Zizmare, A. Kulkarni, Y. Singh, F. J. Weinreich, S. Kommoss, M. A. Reymond, and C. Trautwein, “Acidic ascites inhibits ovarian cancer cell proliferation and correlates with the metabolomic, lipidomic and inflammatory phenotype of human patients,” *Journal of Translational Medicine*, vol. 20, p. 581, Dec. 2022.

[120] U. Pilatus, E. Aboagye, D. Artemov, N. Mori, E. Ackerstaff, and Z. M. Bhujwalla, “Real-time measurements of cellular oxygen consumption, pH, and energy metabolism using nuclear magnetic resonance spectroscopy,” *Magnetic Resonance in Medicine*, vol. 45, pp. 749–755, May 2001.

[121] H. Wen, Y. J. An, W. J. Xu, K. W. Kang, and S. Park, “Real-time monitoring of cancer cell metabolism and effects of an anticancer agent using 2D in-cell NMR spectroscopy,” *Angewandte Chemie (International Ed. in English)*, vol. 54, pp. 5374–5377, Apr. 2015.

[122] R. Knitsch, M. AlWahsh, H. Raschke, J. Lambert, and R. Hergenröder, “In Vitro Spatio-Temporal NMR Metabolomics of Living 3D Cell Models,” *Analytical Chemistry*, vol. 93, pp. 13485–13494, Oct. 2021. Publisher: American Chemical Society.